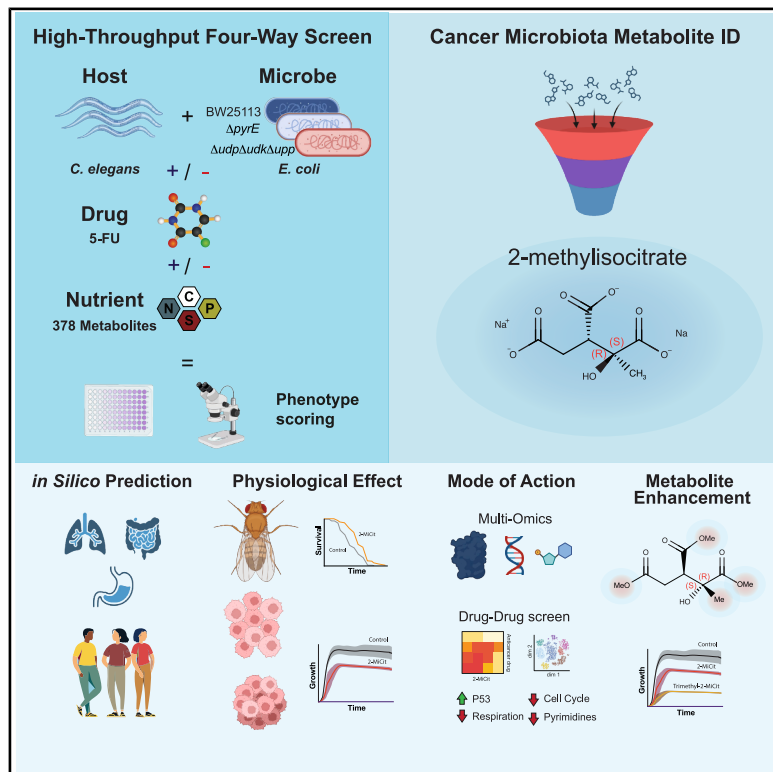


Chemotherapy modulation by a cancer-associated microbiota metabolite

Graphical abstract



Highlights

- Host-microbe-drug-nutrient 4-way screen identifies 2-methylisocitrate regulating 5-FU
- 2-methylisocitrate inhibits mitochondrial IDH and causes nucleotide imbalance and DNA damage
- Cancer-microbiome metabolites have double-edged sword effects in chemotherapy
- Natural microbial metabolites can be modified into enhanced therapeutic agents

Authors

Daniel Martinez-Martinez,
Tanara V. Peres, Kristin Gehling, ...,
Christian Frezza, Helena M. Cochemé,
Filipe Cabreiro

Correspondence

f.cabreiro@uni-koeln.de

In brief

Martinez-Martinez et al. combine a host-microbe-drug-nutrient screen with multi-omics to reveal how the cancer-associated microbiota modulates chemotherapy. They identify 2-methylisocitrate, a microbial metabolite that inhibits cancer growth and synergizes with 5-fluorouracil by impairing mitochondrial metabolism. Using chemical modifications, they enhance 2-methylisocitrate potency, offering a promising co-adjuvant strategy for cancer treatment.



Article

Chemotherapy modulation by a cancer-associated microbiota metabolite

Daniel Martinez-Martinez,^{1,2,10} Tanara V. Peres,^{1,2,10} Kristin Gehling,^{3,10} Leonor Quintaneiro,² Cecilia Cabrera,^{1,2} Maksym Cherevatenko,⁸ Stephen J. Cutty,^{1,2} Lena Best,⁴ Georgios Marinos,⁴ Johannes Zimmerman,⁴ Ayesha Safoor,³ Despoina Chrysostomou,⁵ Joao B. Mokochinski,^{1,2} Alex Montoya,^{1,2} Susanne Brodesser,³ Michalina Zatorska,² Timothy Scott,² Ivan Andrew,¹ Holger Kramer,^{1,2} Masuma Begum,⁶ Bian Zhang,⁶ Bernard T. Golding,^{6,7} Julian R. Marchesi,⁵ Susumu Hirabayashi,^{1,2} Christoph Kaleta,⁴ Alexis R. Barr,^{1,2} Christian Frezza,⁸ Helena M. Cochemé,^{1,2} and Filipe Cabreiro^{1,2,3,9,11,*}

¹MRC Laboratory of Medical Sciences (LMS), Du Cane Road, London W12 0HS, UK

²Institute of Clinical Sciences, Imperial College London, Hammersmith Hospital Campus, Du Cane Road, London W12 0HS, UK

³University of Cologne, Faculty of Mathematics and Natural Sciences, Institute of Genetics, Cluster of Excellence Cellular Stress Responses in Aging-associated Diseases (CECAD), Cologne, Germany

⁴Institute for Experimental Medicine, Kiel University, Kiel 24105, Germany

⁵Division of Digestive Diseases, Faculty of Medicine, Imperial College London, London W12 0NN, UK

⁶BiBerChem Research Ltd., The Biosphere, Draymans Way, Newcastle Helix, Newcastle upon Tyne NE4 5BX, UK

⁷School of Natural & Environmental Sciences, Bedson Building, Newcastle University, Newcastle upon Tyne NE1 7RU, UK

⁸University of Cologne, Faculty of Medicine and University Hospital Cologne, Institute for Metabolomics in Ageing, Cluster of Excellence Cellular Stress Responses in Aging-associated Diseases (CECAD), Cologne, Germany

⁹Center for Molecular Medicine Cologne (CMMC)-University of Cologne, Robert-Koch Str. 21, 50931 Cologne, Germany

¹⁰These authors contributed equally

¹¹Lead contact

*Correspondence: f.cabreiro@uni-koeln.de

<https://doi.org/10.1016/j.cels.2025.101397>

SUMMARY

Understanding how the microbiota produces regulatory metabolites is of significance for cancer and cancer therapy. Using a host-microbe-drug-nutrient 4-way screening approach, we evaluated the role of nutrition at the molecular level in the context of 5-fluorouracil toxicity. Notably, our screens identified the metabolite 2-methylisocitrate, which was found to be produced and enriched in human tumor-associated microbiota. 2-methylisocitrate exhibits anti-proliferative properties across genetically and tissue-diverse cancer cell lines, three-dimensional (3D) spheroids, and an *in vivo* *Drosophila* gut tumor model, where it reduced tumor dissemination and increased survival. Chemical landscape interaction screens identified drug-metabolite signatures and highlighted the synergy between 5-fluorouracil and 2-methylisocitrate. Multi-omic analyses revealed that 2-methylisocitrate acts via multiple cellular pathways linking metabolism and DNA damage to regulate chemotherapy. Finally, we converted 2-methylisocitrate into its trimethyl ester, thereby enhancing its potency. This work highlights the great impact of microbiome-derived metabolites on tumor proliferation and their potential as promising co-adjuvants for cancer treatment.

INTRODUCTION

Cancer development results from the complex interplay between intrinsic and extrinsic factors, including host genetics, environmental cues, and the recently recognized influence of the microbiota.¹ Numerous studies have explored the influence of nutrition on determining both risk and cancer progression,² as well as on the microbiome.³ Microbial molecules exhibit remarkable chemical diversity and have been described as causal agents of cancer in humans. Well-known examples include virulence factors like CagA from *Helicobacter pylori*⁴ and colibactin from genotoxic *Escherichia coli* pks+ strains.⁵ Conversely, other microbial compounds have anti-cancer

properties, such as inhibiting cancer cell growth, inducing apoptosis, or suppressing angiogenesis. Examples of microbial metabolites with anti-cancer properties include antibiotics such as actinomycin D⁶ and mitomycin C,⁷ produced by bacteria, as well as compounds like paclitaxel, produced by the fungus *Taxomyces andeanae*.⁸ Therefore, microbiota-derived metabolites can be a double-edged sword: on the one hand, they can enhance inflammatory responses in the tumor microenvironment (TME), accelerating tumor progression and contributing to cancer development⁹ exemplified by secondary bile acids, trimethylamine-oxide, and tryptophan-derived metabolites,¹⁰ while on the other hand, they can activate immune cells, enhancing anti-tumor immunity, for which short-chain fatty



acids and indole derivatives have been shown to have a protective role against tumorigenesis.¹¹

Shifts in microbial communities can also occur due to chemotherapy.¹² While some bacteria-mediated mechanisms bolster the efficacy of drugs,^{13–16} others can undermine therapeutic efforts.^{17,18} Bacteria can also bioaccumulate drugs, thus reducing the therapeutic quantity available to host cells.¹⁹ Furthermore, bacteria can act as mediators between xenobiotics and the host by integrating drug and nutrient signals, rewiring their metabolism accordingly, and secreting molecules that modulate host physiology.²⁰ Much less explored is the role played by microbial metabolites in regulating drug action and their impact on drug pharmacokinetics through regulation or inhibition of host enzymes. One of the most prominent examples is the microbiome-produced metabolite *p*-cresol, which interferes with acetaminophen clearance through competitive inhibition of O-sulfonation in the liver.²¹ In a cancer context, microbial metabolites can be used in combination with anti-cancer therapies, such as chemotherapy, radiation therapy, or immunotherapy, to enhance treatment efficacy. Recently, bacterial 3-indole acetic acid from the gut microbiota was shown to enhance the efficacy of 5-fluorouracil [5-FU] + irinotecan + oxaliplatin (FIRINOX) chemotherapy in pancreatic cancer through a myeloperoxidase ROS-dependent mechanism.¹⁵ Moreover, the ability of microbes to produce and administer molecules of interest within target tissues has gained traction over the last years.^{22,23} For instance, the *E. coli* strain Nissle 1917 has been engineered in several ways to fight cancer, for example, by modulating immunotherapy,^{24,25} by delivering cytotoxic proteins to the TME,²⁶ or by transforming dietary glucosinolate into sulforaphane to control cancer progression.²⁷ Yet, to our knowledge, no studies exist on the role of cancer-associated microbiota metabolites in modulating cancer and chemotherapy.

Despite the promising potential of microbial metabolites in anti-cancer therapy, there are challenges, such as identifying novel compounds and optimizing their pharmacokinetic properties. Approaches targeting the holobiont, defined at the host together with its microbiota, are thus required to systematically unravel these mechanisms at the cellular and molecular levels. Model organisms, such as nematodes, flies, and fish, have substantially contributed to our understanding of host-microbe interactions.²⁸ Specifically, *C. elegans* has proven to be a key holobiont model organism in unraveling host-microbe interactions due to its unique, well-suited features, which include the amenability to perform high-throughput screens, a transparent body amenable to imaging, a highly organized intestinal epithelium, and the easy generation of genetically modified organisms. In addition, nutritional, pharmacological, and microbiological inputs can be relatively simply manipulated and thus allow testing a multitude of parameters on host physiology at a depth unattainable with any other model organism.²⁹

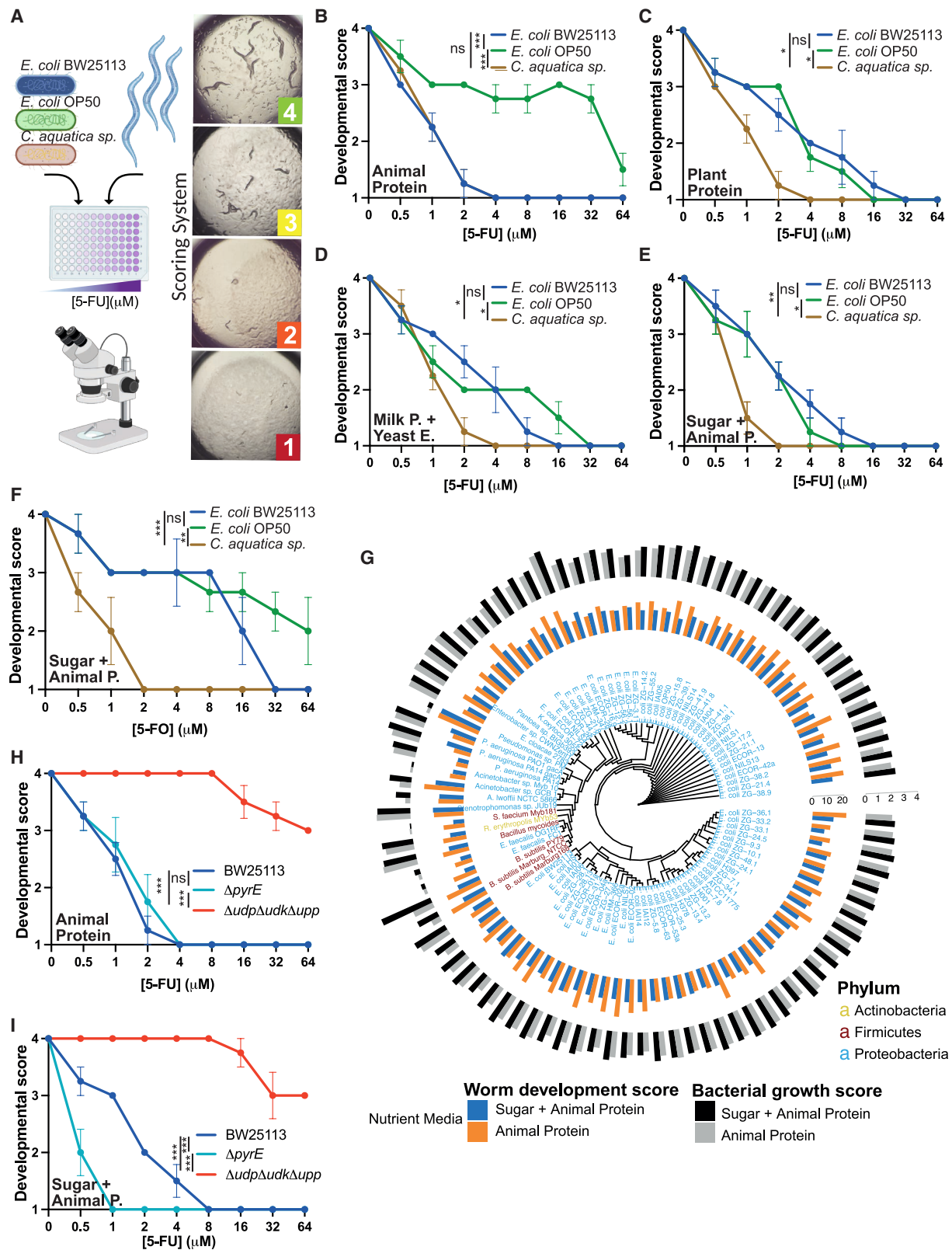
We and others have shown that fluoropyrimidines can be biotransformed by gut microbes to activate 5-FU and other fluoropyrimidines to 5-FUMP, 5-FUTP, and 5-FdUMP using the enzymes uracil phosphoribosyltransferase (Upp), uridine kinase (Udk), and uridine phosphorylase (Udp)^{13,14,30} or alternatively deactivated by dihydropyrimidine dehydrogenase (PreTA) to dihydrofluorouracil.¹⁷ Since nutrients are a major factor regulating bacterial metabolism, we hypothesized that environmental fac-

tors such as diet could influence the role played by microbes in the efficacy of 5-FU. Here, using a high-throughput host-microbe-drug-nutrient 4-way screen²⁰ and a combination of molecular and genetic approaches, we investigated the impact of dietary metabolites on the efficacy of 5-FU in *C. elegans*. We discovered that microbes produce distinct metabolites regulating fluoronucleotide chemotherapeutic efficacy in a diet-dependent manner. In particular, we found that the metabolite 2-methylisocitrate (2-MiCit) that regulates 5-FU efficacy in *C. elegans* is also produced by the cancer-associated microbiota, distinctively enriched in diverse tissues, and significantly enriched in adenocarcinoma patients versus healthy controls. We show that 2-MiCit has anti-cancer cell growth properties in genetically diverse cancer cell lines, three-dimensional (3D) spheroid cancer models, as well as in a *Drosophila* gut tumor model. Our findings suggest that 2-MiCit exerts its anti-proliferative effects via multiple cellular mechanisms, including suppression of mitochondrial respiration through inhibition of isocitrate dehydrogenase (IDH), leading to nucleotide imbalance and activation of p53-associated pathways. Furthermore, through a drug-metabolite screen in HCT116 cancer cells, we mapped the anti-cancer chemotherapeutic signatures that are synergistic or antagonistic with 2-MiCit action and revealed the mechanism of synergy between 2-MiCit and 5-FU. Lastly, through tailored organic chemistry routes, we rationally modified 2-MiCit to increase its anti-proliferative properties, indicating that this modified compound may serve as a promising candidate for future research and potential cancer treatment.

RESULTS

Nutrients regulate 5-FU efficacy in a bacteria-dependent manner

First, we developed a semi-quantitative assay to establish the role of dietary cues on drug action in *C. elegans* (Figure 1A). Briefly, we incubated *C. elegans* at the first larval stage, L1, with 2 *E. coli* bacterial strains, OP50 and BW25113 (BW), and another commonly used bacterial strain for *C. elegans* 5-FU studies—*Comamonas aquatica*.^{13,14} Multi-well plates on which both bacteria and worms are incubated were prepared using media with diverse nutritional composition and/or with increasing concentrations of 5-FU. After 48 h, worm development was scored as shown in Figure 1A and attributed a numerical value per drug dose (details can be found in the STAR Methods section). We observed that the effects of drugs on *C. elegans* growth were dependent on both the species and strain of bacteria (Figure 1B), as well as on the nutritional content of the media used for both bacterial and worm growth (Figures 1C–E and S1A–S1C), and the type of fluoronucleotide challenge (Figures 1E, 1F, and S1A–S1C). Based on these results, we tested 91 strains (9 lab isolates and 82 wild isolates) belonging to 3 phyla—Actinobacteria, Firmicutes, and Proteobacteria, which are abundantly present in cancer-associated microbiota.^{31,32} We found that bacterial species and strain-level resolution dictate 5-FU effects on worm growth in a nutrient-dependent manner (Figures 1G and S1D; Table S1). In parallel, we also measured the impact of 5-FU on bacterial growth and measured the respective IC50 values for each bacterial genotype and nutritional media. Albeit a larger variability is observed



(legend on next page)

between different species compared with within species, no correlation was found between drug inhibitory effects on bacterial growth and worm growth inhibition in a nutrient-dependent manner (Figures S1E–S1M). Next, we tested whether these drug- and diet-dependent effects on *C. elegans* growth were mediated by the two key pathways previously reported to regulate drug effects: (1) *de novo* ribonucleotide synthesis and (2) the salvage ribonucleotide pathway.^{13,14} We show that the triple deletion of *upp*, *udk*, and *udp*, which fully abrogates the salvage pathway, impaired drug action irrespective of the external nutrient supply. However, ablation of the *de novo* pathway, through deletion of *pyrE*, revealed that sugar effects on drug action, but not protein effects, were fully dependent on the *de novo* pathway (Figure 1H). Thus, screening of *C. elegans* reveals additional mechanisms of drug action in a diet-dependent manner independent of direct microbial growth impairment by fluoropyrimidines.

To unravel the complexities of these interactions, we applied our previously published host-microbe-drug-nutrient high-throughput 4-way screening method²⁰ (Figure 2A). We systematically profiled the impact of 5-FU action on both bacterial and worm growth in three bacterial genotypes: wild-type (WT) control, the Δ *pyrE* mutant ablating the *de novo* pathway, and the Δ *upp* Δ *udk* Δ *udp* triple mutant, which abrogates the salvage pathway, in the presence of 378 metabolites present in Biolog covering all major nutrient classes and substrates for both host and microbial cells (Figures 2B–2D and S2A; see Table S2 for a list of individual compounds tested). Higher concentrations of 5-FU were applied for the Δ *upp* Δ *udk* Δ *udp* triple mutant due to its inherent resistance to the drug.¹⁴ Overall, we found that pyrimidine nucleotides and nucleosides rescued both bacterial (Figures S2B–S2I) and worm growth against the anti-proliferative effects of 5-FU in a salvage ribonucleotide-dependent manner (Figures 2B–2D). Many carbohydrates, sugars, and polyols rescued worm development (developmental score of ≥ 3) but not bacterial growth (normalized bacterial growth below 1) by 5-FU when worms were colonized by feeding the WT strain (Figures 2B–2D and S2B–S2K). Notably, the intermediate worm development rescue of these nutrients was lost if worms were co-cultured with the *de novo* *pyrE* mutant (Figures 2B, 2C, and 2E), but was enhanced to full developmental stage (score = 4) when co-cultured with the salvage pathway triple mutant (Figures 2B, 2D, and 2E). The importance of these metabolites per bacterial genotype on host phenotype is captured using a ternary plot. Nucleotides have a more potent effect on BW and the *pyrE* mutant, while sugars exert their activity mainly in the salvage pathway triple mutant (Figure 2F). At the functional level, using Kyoto Encyclopedia of Genes and Genomes (KEGG)

pathway enrichment, our analysis confirmed that nutrients that feed into bacterial pyrimidine and galactose metabolism or are modulated by the sugar phosphotransferase system (PTS) regulate *C. elegans* phenotypes with 5-FU (Figure 2G). Overall, we conclude that key nutrient classes of sugars and nucleotides regulate 5-FU effects on the host through bacterial metabolites.

Bacterial metabolites regulate 5-FU efficacy

Our 4-way screen identified the PTS, a key active transport system in bacteria responsible for coordinating the uptake of various carbohydrate molecules. The cyclic AMP (cAMP) receptor protein (CRP) is a master regulator of this signaling pathway, controlling the transcription of numerous genes in response to changes in the nutritional environment.³³ To further validate our screen findings, we tested whether the deletion of *cpr* mediated 5-FU effects on the host in a nutrient-dependent manner. Our data show that the addition of glucose significantly decreased 5-FU efficacy when worms were co-cultured with WT *E. coli*. As predicted, disruption of *cpr* function strongly reduced drug efficacy in animal protein-based media but enhanced drug efficacy in the presence of glucose (Figure 3A) in a mechanism independent from the regulation of CRP by 5-FU in a nutrient-dependent manner (Figure S3A). To understand the link between nutrients and drug effects, we performed a 3-way host-microbe-drug screen¹⁴ in regular animal protein-based media (nematode growth media [NGM]) \pm glucose. This analysis included a selection of 248 *E. coli* genes with a role in 5-FU action in worms previously identified from other studies^{13,14} and genes that are under direct regulation of the transcription factor *cpr*²⁰ (Figures S3B and S3C; Table S1) and performed functional enrichment analysis (Figure 3B). We found two major metabolic pathways regulating 5-FU, enriched in a \pm glucose-dependent manner: the central carbon/energy and nucleotide metabolism. For example, we observe that several bacterial genes involved in the TCA cycle rescued worm developmental arrest caused by 5-FU (x axis, normalized score of ≥ 0.5), whereas in the presence of glucose, the absence of these bacterial genes made worms more sensitive to 5-FU (color gradient, normalized score of <0 , red).

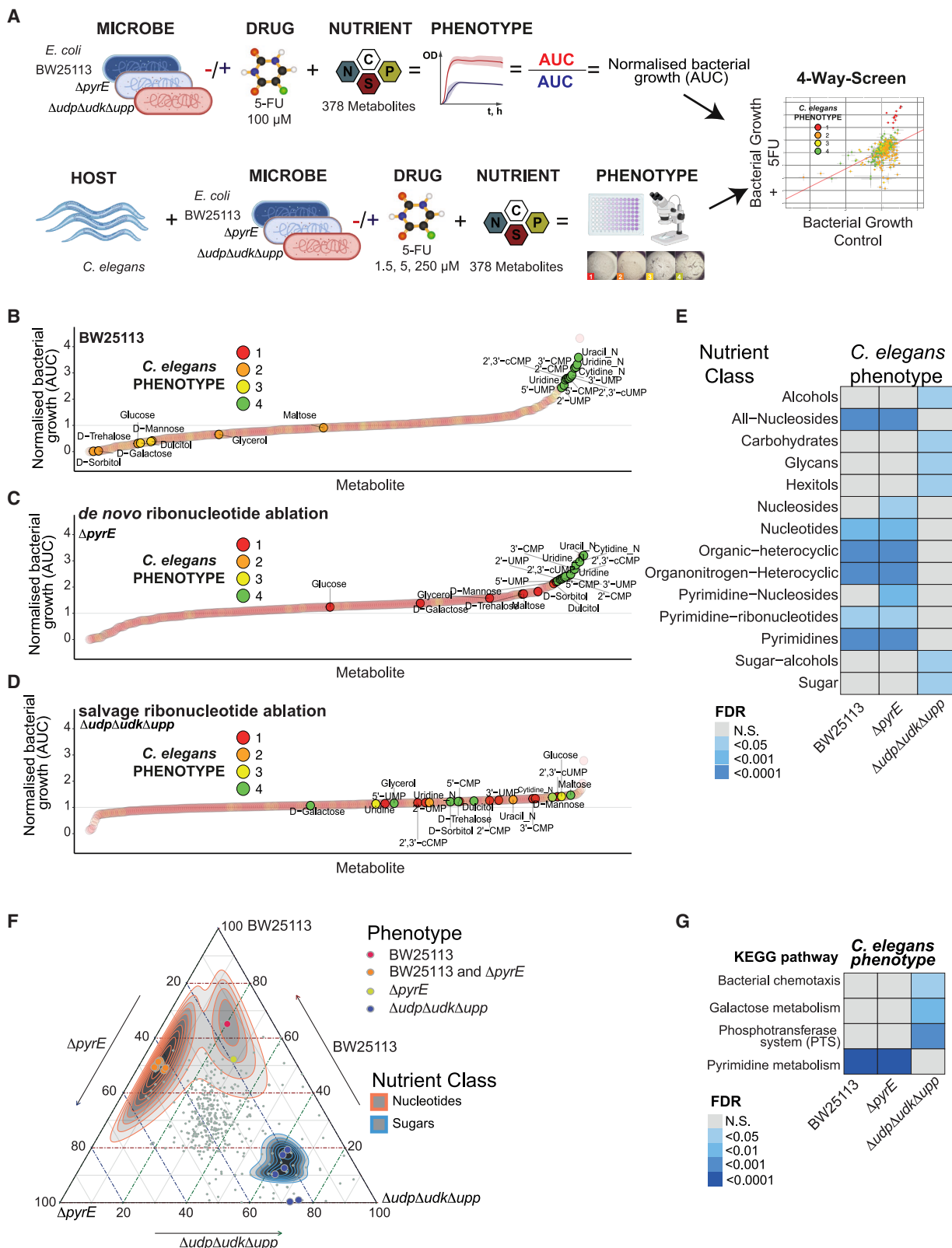
First, we focused on the role of nucleotide metabolism. As expected, genes belonging to purine metabolism (IMP, guanosine, and adenosine pathways, for example, *guaA*) impaired drug effects regardless of nutrient conditions (Figures 3B and 3C). By contrast, we found that deletion of all genes involved in UMP biosynthesis and the superpathway of ribo- and deoxyribonucleotides (e.g., *pyrE*) had little to no effect in mediating 5-FU effects

Figure 1. Fluoropyrimidine efficacy in *C. elegans* depends on bacterial metabolism, drug structure, and media nutrient source

(A–E) Diagram of developmental assay procedure and visual scoring system used to assess drug efficacy on the host (A). Wild-type (WT) *C. elegans* at the L1 stage was fed 3 different bacterial strains, *E. coli* BW25113, *E. coli* OP50, or *C. aquatica*, and exposed to 0–64 μ M 5-FU. After 72 h, worms were scored 1 to 4, with the lowest meaning arrested development and the highest for worms that achieved adulthood and laid eggs. Developmental scores were obtained for worms grown on 4 different nutrient compositions of nematode growth media (NGM): bacto peptone containing animal-based protein (B), soy peptone using plant protein sources (C), Luria broth (LB) comprising milk protein casein and yeast extract (D), or brain heart infusion broth (BHI) using animal protein and sugars (E). (F) Developmental scores of *C. elegans* in BHI treated with 5-FU.

(G) Worm and bacterial cumulative scores show strain- and species-specific effects of 5-FU on worm and bacterial growth. Larger bars denote lower drug toxicity (see details in Figure S1D for its respective calculation).

(H and I) 5-FU efficacy on *C. elegans* fed WT BW25113 *E. coli*, Δ *pyrE*, or Δ *udp* Δ *udk* Δ *upp* mutants on NGM with animal-based protein without (H) or with (I) sugars. Data are means \pm SD. Not significant (NS) $p \geq 0.05$, * $p < 0.05$, ** $p < 0.01$, *** $p < 0.001$ from ANOVA tests with multiple comparisons adjusted by Tukey's HSD.



(legend on next page)

on animal protein-based media but antagonized the rescuing drug effects observed in the presence of added glucose in BW (Figure 3B). To show that nutrients regulate drug effects on the host through bacterial metabolites, we tested glycerol supplementation whose metabolism, unlike glucose, relies on a single gene, glycerol kinase (*glpK*). While glycerol supplementation significantly reduced drug efficacy on worm growth when co-cultured with WT *E. coli*, this effect was abolished when worms were co-cultured with a *glpK* mutant (Figure S3D). Likewise, we observed that deletion of genes belonging to the *de novo* synthesis of UMP (Figures 3C–3E) abolished sugar effects, but not deletion of genes belonging to the *de novo* deoxyribonucleotides (Figures S3E and S3F). Glucose supplementation did not alter the expression of host ribonucleotide genes (*ndk-1*, *umps-1*, *pyr-1*, *upp-1*, and *dpyd-1*), and worm *pyr-1* and *umps-1* genetic mutants, involved in host *de novo* production of the pyrimidine UMP, did not alter the worm response to 5-FU with or without glucose supplementation (Figures S3G and S3H). We also tested whether sugar supplementation altered the ability of bacterial cells to further convert the 5-FU prodrug into its active metabolites in both bacteria and *C. elegans*. We found that sugar supplementation increased, rather than decreased, the conversion of 5-FU to 5-FUMP or 5-FUrd in a bacterial salvage-dependent manner (e.g., *udp*, *udk*, *upp*) but independent of the *de novo* pathway (e.g., *pyrE*) (Figures 3F and 3G). Finally, we tested whether glucose supplementation altered nucleotide metabolism in bacteria. We found that glucose supplementation altered the nucleotide profile in bacteria. In particular, we observed a significant increase in the abundance of orotate and UTP. Since only UTP increased in a *pyrE*-dependent manner, we concluded that sugar-derived bacterial UTP counteracted the efficacy of 5-FU in the host (Figure 3H). Previously, we observed that supplementation with pyrimidine nucleosides and nucleoside phosphates impaired 5-FU efficacy in a *pyrE*-independent manner (Figures 2B and 2C). Together, these data allow us to conclude that bacteria metabolize diverse sugars to produce pyrimidine nucleotide metabolites that regulate drug efficacy in the host and are consistent with the described roles of the nucleotide pathways in the regulation of 5-FU in *C. elegans*.^{13,14,30}

Next, we focused our attention on central carbon metabolism. We found that genes belonging to central carbon metabolism and under direct transcriptional control by *cpr* (e.g., the

TCA cycle citrate synthase *gltA*) regulated nutrient effects on 5-FU action (Figures 3B, 3C, S4A, and S4B). We observed that deletion of genes upstream of the metabolite pyruvate did not regulate 5-FU efficacy, whereas genes downstream, belonging to both the glycolytic and TCA pathways, reduced 5-FU effects in worms on protein-based media and improved drug efficacy in the presence of added sugar (Figures 3B, S3B, 4A, and S4C). This suggested that pyruvate was a central node for the observed effects. We hypothesized that the metabolic rewiring of pyruvate toward other pathways was essential for the regulation of 5-FU. To test this, we created double mutants of *gltA* with all 23 other non-essential genes involved in either pyruvate production or catabolism. Only a single gene, *prpB*, belonging to the methylcitrate cycle, improved 5-FU efficacy back to WT levels when combined with *gltA* deletion (Figure S4D). The methylcitrate cycle is a prokaryotic metabolic pathway closely related to both the TCA and the glyoxylate cycle, sharing metabolic enzymes, substrates, and products, with the overall function to detoxify toxic levels of propionate.³⁴ Only deletion of *prpB*, but no other genes from the methylcitrate cycle, rescued the bacterial effects of *gltA* on 5-FU efficacy (Figures 4B and S4E). These data suggested that deletion of *gltA* is either involved in the regulation of activated fluoronucleotides or in the rewiring of 2-MiCit production. To test this hypothesis, we measured levels of fluoronucleotides, nucleotides, central carbon metabolites, and 2-MiCit. We did not find that deletion of *gltA* altered 5-FU activation to 5-FUMP or 5-FUrd compared with WT both in worms or bacteria (Figures 4C and S4F) nor the levels of nucleotides and central carbon metabolites in worms (Figure S4G). Furthermore, no interactions between *gltA* and *pyrE* were observed in the mediation of 5-FU effects on the host (Figure S4H). However, deletion of *gltA* significantly decreased 2-MiCit abundance, and its levels were rescued by a *prpB* mutation, confirming the metabolic rewiring of the 2-MiCit cycle by *gltA* (Figure 4D). Consistent with this observation, supplementation with oxaloacetate and propionate, either separately or in combination, rescued both the efficacy of 5-FU in worms co-cultured with a *gltA* bacterial mutant (Figures 4E and S4I) and returned the levels of 2-MiCit in the *gltA* bacterial mutant back to WT levels (Figure S4J). Altogether, these data lead us to conclude that central carbon metabolism genes identified in our screen regulate 2-MiCit production, impacting 5-FU efficacy.

Figure 2. 4-way screening reveals the importance of individual nutrients in 5-FU efficacy

(A) Microbe-drug-nutrient screen to assess the effects of 378 metabolites from Biolog plates on bacterial growth under 5-FU exposure. Metabolite composition can be found in Figure S2A and Table S2. The resulting data were represented as the OD₇₅₀ area under the curve (AUC) integral for each metabolite. Host-microbe-drug-nutrient effects were assessed in N2 worms fed BW25113 *E. coli* ± 5-FU and with supplementation of 378 metabolites individually. The resulting phenotype scores are color-coded in the graphs.

(B–D) Host-microbe-drug-nutrient interaction landscape. Plots depict combined microbe and host effects of each metabolite supplemented (x axis) and bacterial relative growth changes on treatment versus control conditions (y axis), calculated as the adjusted growth of the growth integrals (AUC) of at least 4 biological replicates. Dashed line represents control condition. Relative growth of changes of BW25113 exposed to 100 μM 5-FU versus control (y axis) caused by nutrient (x axis). *C. elegans* development phenotype was scored on BW25113 bacteria in the presence of 5 μM 5-FU (B). Δ*pyrE* bacterial mutants depleted of *de novo* ribonucleotide synthesis were exposed to 100 μM 5-FU, and worms fed this mutant were scored in the presence of 5 μM 5-FU (C), or Δ*udp*Δ*udk*Δ*upp* bacterial mutants were exposed to 100 μM 5-FU, and worms were scored in the presence of 250 μM 5-FU (D).

(E) Functional enrichment of nutrient classes on the host phenotype per bacterial genotype.

(F) Ternary plot of nutrient effects on host phenotype per bacterial genotype. The 0–100 axis represents the strength of individual nucleotides and sugars on host phenotype rescue.

(G) Functional enrichment of KEGG pathways regulating 5-FU effects in 3 bacterial genetic backgrounds.

Enrichment analysis in (E) and (G) was done with hypergeometric tests, and Benjamini-Hochberg correction was applied for multiple testing.

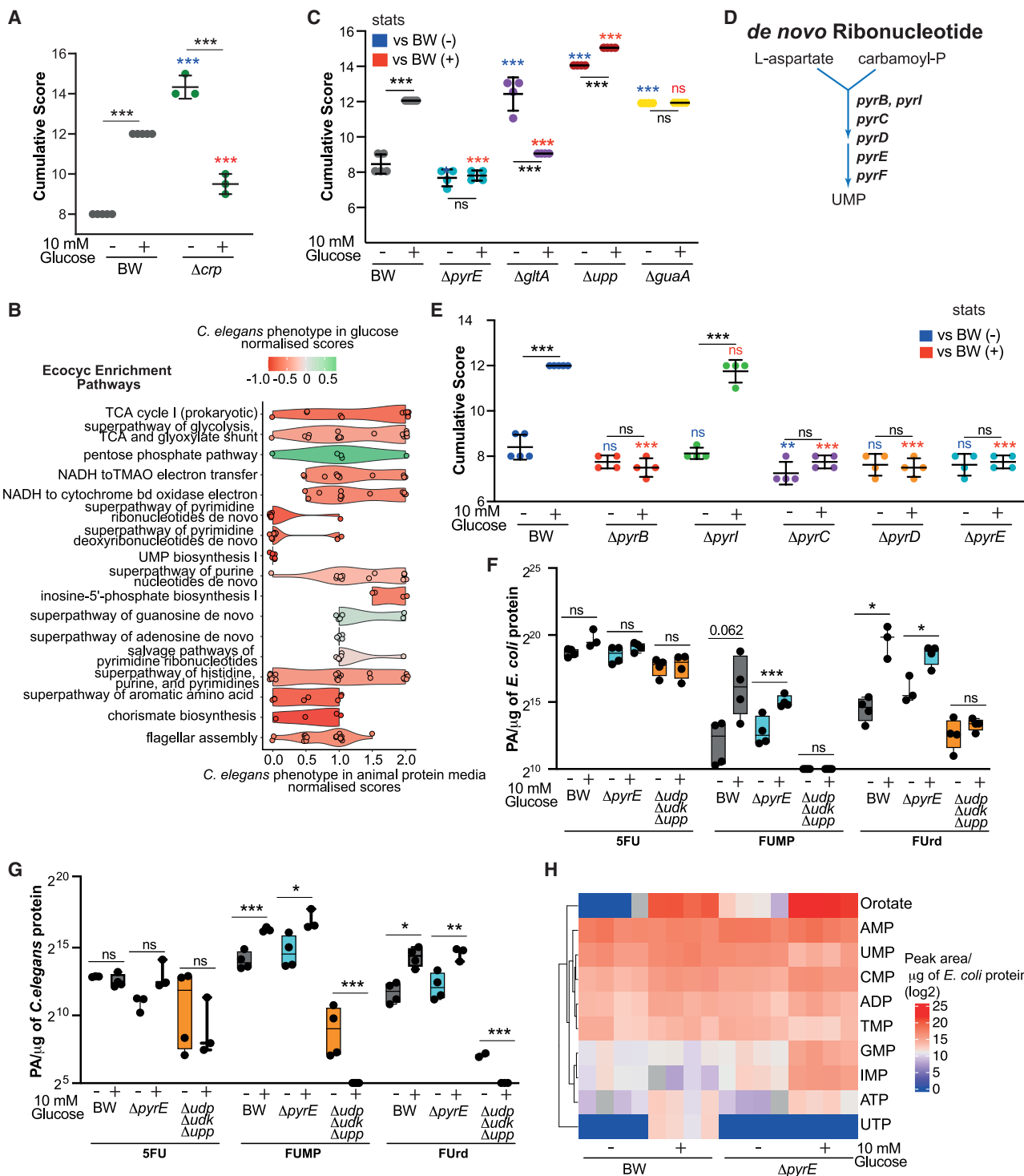


Figure 3. De novo synthesis of pyrimidine nucleotides from sugars regulates 5-FU efficacy in the host

(A) *C. elegans* WT fed *E. coli* BW25113 (BW) or catabolite repressor protein mutant CRP on NGM \pm 10 mM glucose. Cumulative developmental assay scores (CS) were obtained by summing the qualitative assessment of worm development at 0, 1, 2.5, and 5 μ M 5-FU. Higher CS values indicate lower drug efficacy.

(B) EcoCyc pathway enrichment for gene deletions and their effects on *C. elegans*. Violin plots of CS values in both NGM (x axis) and with glucose supplementation (color). Color ranges from red (sensitive to treatment) to green (resistant to treatment) as a normalized phenotype score, linear scale. Each dot represents a mutant belonging to a specific pathway and its effect on regulating drug effects in NGM.

(C) CS of *C. elegans* WT fed bacterial mutants of the *de novo* pyrimidine biosynthesis pathway Δ pyrE, TCA cycle Δ gltA, salvage ribonucleotide pathway Δ upp, and the guanine ribonucleotide *de novo* pathway Δ guaA in NGM \pm 10 mM glucose.

(legend continued on next page)

2-MiCit is produced by the cancer-associated microbiome and exerts anti-proliferative effects on cancer cells

Since *E. coli* is a common member of the gut microbiota associated with many human solid tumors,³² we explored the potential connection between bacterial 2-MiCit production and tumors in humans by performing microbial community modeling. In this modeling approach, sequencing data were aligned with a database of metabolic models representing bacteria found in the cancer-associated microbiome (Figure S5A; clinical demographics are available in Table S4). These individual metabolic models were integrated into a comprehensive metabolic microbial community model, considering the abundance of each bacterial species and nutrient availability in plasma. Through linear optimization applied to these models, we were able to predict the 2-MiCit production capacity of these bacterial species (see STAR Methods for further details). Since 5-FU is mostly used in the clinic to treat breast, colon, rectum, stomach, pancreas, and skin cancers, we first inquired which tissues are most strongly associated with the production of 2-MiCit based on the identification of bacteria within these tissues. We found that both colon and breast are among the tissues where cancer-associated microbiota had the highest predicted capacity to produce 2-MiCit, although employing bacteria from phylogenetically diverse phyla/genera (Figures 5A and S5B). Likewise, characterization of 2-MiCit production from microbiome genomes at the species level in over 4,000 metastatic tumor biopsies³¹ also reveals the gastrointestinal (GI) tract, skin, and pancreas as the sites with the highest producers and employing microbes predominantly from Proteobacteria (Figures S5C–S5E). Next, we compared the gut microbiome from healthy controls and patients with adenomas or adenocarcinomas from five independent cohorts with distinct geographical locations^{35–38} as well as the main contributor species to 2-MiCit production. We found that the microbiome associated with colorectal carcinomas had a significantly higher 2-MiCit production capacity compared with healthy controls and post-operative healthy patients independently of geographical location (Figure 5B). Using this approach, we also identified several bacterial species that contributed to the predicted production of 2-MiCit (e.g., *E. coli*) and others that did not (Figure S5F; Table S4). To validate these findings, we grew cancer-associated bacteria from diverse phyla *in vitro*, separated them into groups of high producers and low/non-producers according to our metabolic models (Table S4), and measured 2-MiCit levels in both the endogenous and exogenous/secreted fractions. We found that cancer-associated microbes produced 2-MiCit in the mM range (Table S5), and this effect was significantly higher in the secreted fraction of microbes classified as producers by our metabolic modeling (Figure 5C), but no major differences were observed between different phyla (Figures S5G and S5H). Given the key role diet plays in regulating

bacterial metabolite production, we performed metabolic modeling for 2,018 nutrients in their capacity to yield 2-MiCit. We found that *E. coli* can utilize 120 nutrients as substrates, with sugars, saccharides, and carboxylic acids as the main substrate nutrient classes (Figure S5I) and capturing 80% of metabolites showing an effect in rescuing worm phenotypes upon 5-FU challenge (Figure 2; Table S4). Next, we performed computational predictions and quantitative measurements of 2-MiCit production under physiological concentrations of propionate,³⁹ in the absence and presence of oxygen. We found that propionate increases the production of 2-MiCit, doubling it in an oxygen-dependent manner (Figures S5J and S5K).

To our knowledge, no prior literature exists on the biological activity of 2-MiCit in eukaryotic cells. Thus, we tested the anti-cancer properties of this metabolite in three independent models. First, we tested the anti-proliferative properties of 2-MiCit in 20 cell lines from blood, bone, breast, cecum, and colon (Table S5). Except for one cell line from the cecum, where 2-MiCit increased proliferation significantly, in the other 16 cell lines, 2-MiCit exhibited a striking anti-proliferative effect, with 9 showing statistically significant growth inhibition (Figures 5D and S5L). From these data, we can conclude that some members of the cancer-associated microbiota produce and secrete 2-MiCit that in general possesses anti-cancer properties, but the extent of the anti-proliferative effects is cell-type-specific (Figure 5D). Since microbes are often associated with solid cancers,³² we also tested whether 2-MiCit possessed anti-proliferative properties in spheroids obtained from HCT116 colorectal cancer (CRC) cells and observed a significant inhibition of growth over time (Figure 5E). Next, we investigated whether 2-MiCit also inhibited cancer cell dissemination and improved survival *in vivo*. For this purpose, we used a *Drosophila ras*^{G12V} *apc*^{RNAi} model, where transgene expression specifically in the hindgut, equivalent to the mammalian colon, causes tumors to display a migratory behavior, invading the intestinal muscle layer and disseminating into the abdominal cavity.⁴⁰ We observed that 2-MiCit significantly decreased the number of disseminated tumor foci and increased survival of *ras*^{G12V} *apc*^{RNAi} animals (Figures 5F, 5G, and S5M–S5O). Overall, these data support a cellular anti-proliferative role for 2-MiCit.

2-MiCit impairs mitochondrial metabolism and induces DNA damage

Since 2-MiCit is a carboxylic acid, we first explored its role in altering metabolism. 2-MiCit has been described as a potential inhibitor of all isozymes of NADP-dependent IDH in *Aspergillus nidulans*.⁴¹ We confirmed that 2-MiCit also inhibited the activity of the mitochondrial human IDH *in vitro* (Figure 6A) and impaired mitochondrial respiration *in vivo* in a dose-dependent manner (Figures 6B, S6A, and S6B). To confirm that 2-MiCit altered cellular metabolism, we performed targeted metabolomics of

(D) Schematic diagram of the *de novo* pyrimidine ribonucleotide pathway.

(E) CS of *C. elegans* WT fed all bacterial mutants of the *de novo* pyrimidine biosynthesis pathway.

(F and G) Quantification of activated fluoronucleotides in *E. coli* (F) and *C. elegans* fed WT, *ΔpyrE*, or *ΔudpΔudkΔupp* mutants (G) ± sugar represented as boxplots.

(H) Quantification of nucleotides in *E. coli* WT and *ΔpyrE* ± sugar. Color represents normalized metabolite quantification by µg of *E. coli* protein, log scale.

Data are means ± SD. NS, $p \geq 0.05$; * $p < 0.05$; ** $p < 0.01$; *** $p < 0.001$ from one-way ANOVA tests with multiple comparisons adjusted by Tukey's HSD. Blue or red asterisks represent statistical comparisons to worms fed BW ± sugar in supplemented media.

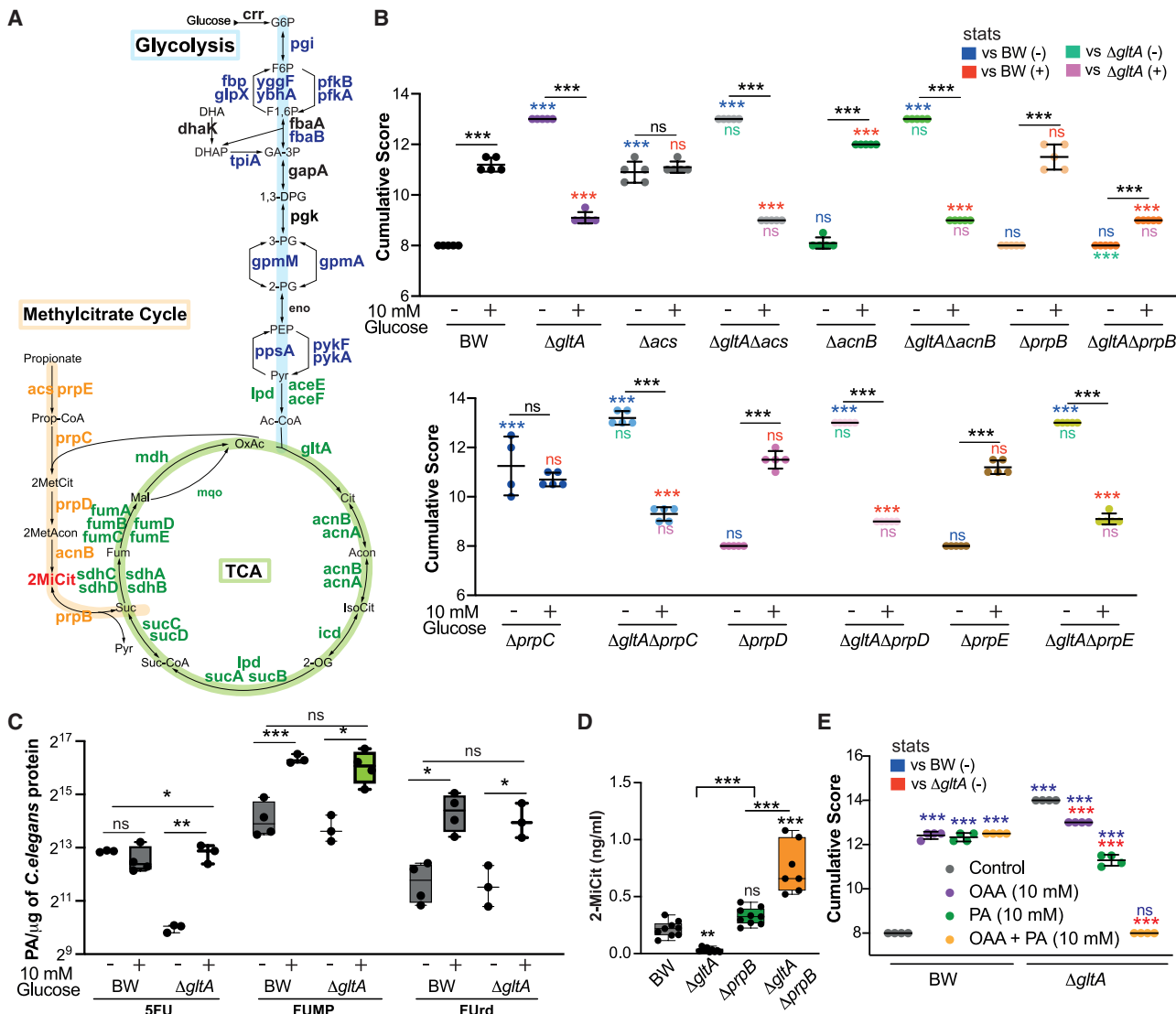


Figure 4. The TCA and methylcitrate cycles regulate 5-FU efficacy in a nutrient-dependent manner

(A) Metabolic interplay of the methylcitrate pathway (orange), glycolysis (blue), and the TCA cycle (green) in *E. coli*.

(B) CS of *C. elegans* fed bacterial single and double mutants of the methylcitrate pathway ± sugar.

(C) Quantification of activated fluoronucleotides in *C. elegans* fed control or $\Delta gltA$ mutants ± sugar.

(D) Quantification of the metabolite 2-methylisocitrate (2-MiCit) in bacteria.

(E) Supplementation of methylcitrate cycle substrates propionic acid (PA) and/or oxaloacetate (OAA) rescue CS phenotype of worms fed $\Delta gltA$ mutant bacteria. Data are means \pm SD. NS p \geq 0.05, *p < 0.05, **p < 0.01, ***p < 0.001 from one-way ANOVA tests with multiple comparisons adjusted by Tukey's HSD. Asterisks colors represent statistical comparisons as indicated.

HCT116 cells treated with and without 2-MiCit. As expected, we observed abundant 2-MiCit in treated cells, and from its role as an IDH inhibitor, we found an increased abundance of metabolites upstream of IDH, namely aconitate and citrate, with a concomitant decrease of 2-oxoglutarate and succinate, which are downstream of IDH in the TCA cycle (Figure 6C). Next, we investigated the mechanisms by which 2-MiCit impacts cells. To address this question, we performed RNA sequencing (RNA-seq) analysis on seven CRC cell lines (SW1417, SKCO1, LoVo, HT29, SW948, DLD-1, and HCT116) with distinct oncogenic alterations, microsatellite instability (Table S5), and with different responses to 2-MiCit treatment (Figure 5D). As ex-

pected, the transcriptomic profiles of each cell line were distinct from each other, and the transcriptional changes induced by 2-MiCit were cell-line-specific (Figures S6C and S6D; Table S6). However, 2-MiCit treatment induced transcriptional changes in a subset of KEGG functions that are functionally linked and were conserved among at least half of the responsive cell types, namely pathways involved in cell cycle, DNA damage repair and replication, pyrimidine metabolism, and the p53 signaling pathway (Figure 6D). Consistent with the transcriptomic data, we observed an enrichment in the metabolomics data with nucleotide metabolism being downregulated (Figures 6E and 6F). Since nucleotide imbalance can cause

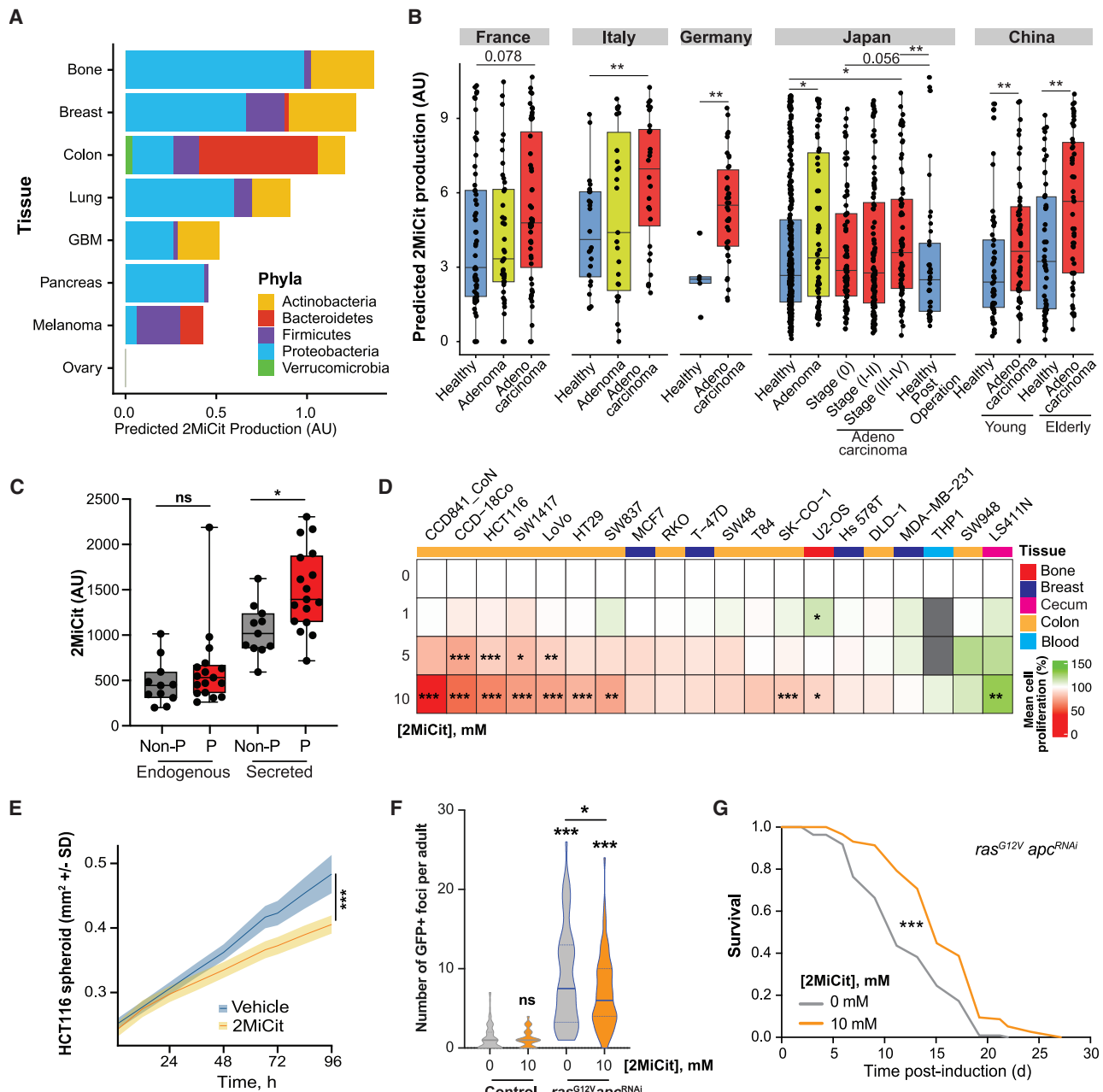


Figure 5. 2-MiCit is secreted by cancer-associated microbes and affects cancer cell proliferation

(A) Computational prediction of 2-MiCit production by microbiome strains across different tumor tissues using microbiome metabolic modeling.

(B) 2-MiCit production is predicted to be increased in gut microbes of adenocarcinoma patients (red) compared with healthy controls from geographically different human cohorts.

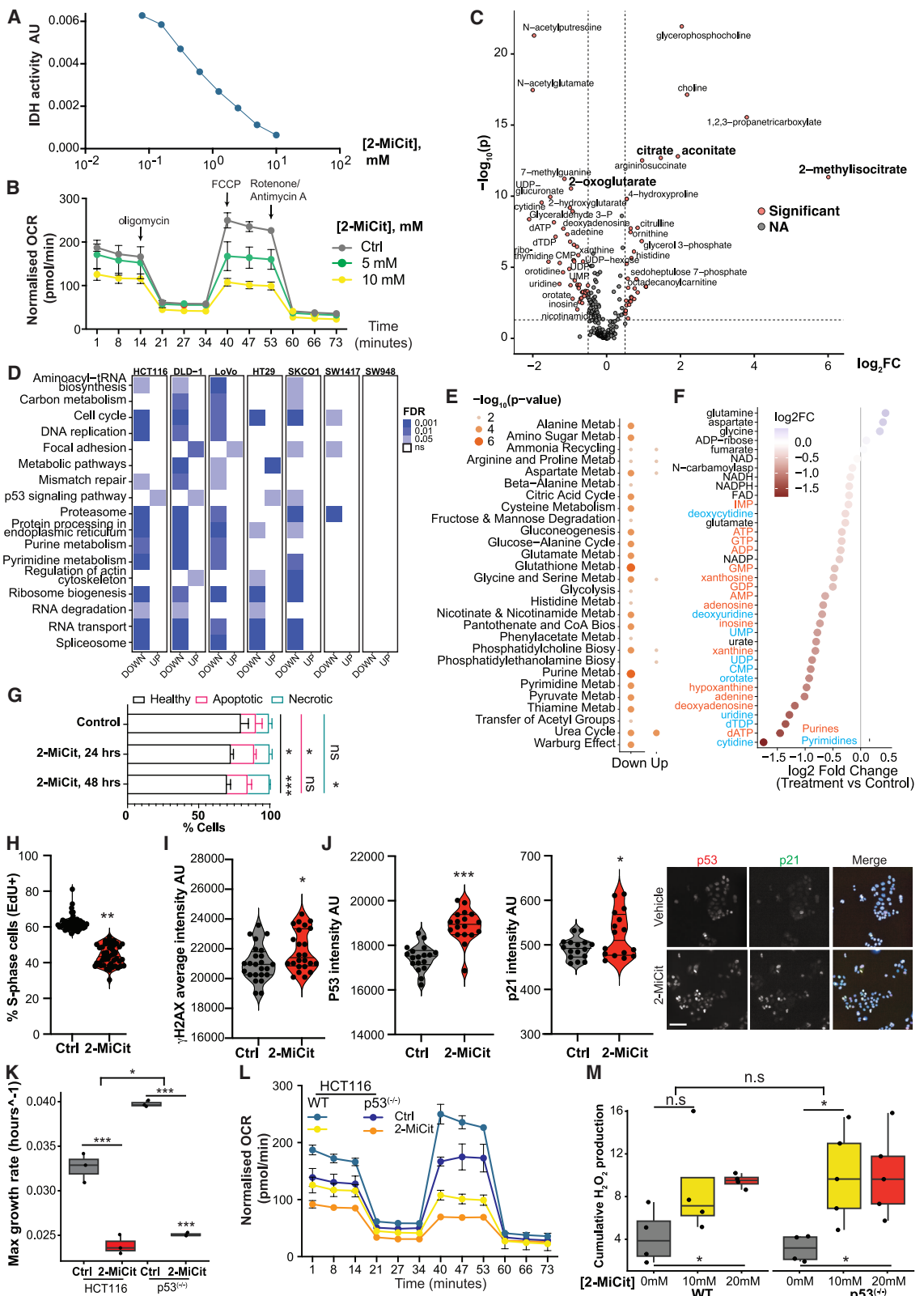
(C) Quantification of 2-MiCit in cancer-associated microbes in the endogenous and secreted fractions. Non-P, predicted non-producers; P, predicted producers.

(D) Dose-dependent effect of 2-MiCit on cell proliferation across multiple cancer cell lines from blood, bone, breast, cecum, and colon. Color represents mean cell proliferation (red < 100%, green > 100%), linear scale.

(E) Growth of HCT116 tumor spheroids is decreased upon 10 mM 2-MiCit treatment.

(F and G) 10 mM 2-MiCit supplementation *in vivo* reduces tumor dissemination (F) and extends survival (G) in a *Drosophila* hindgut tumor model.

NS $p \geq 0.05$, * $p < 0.05$, ** $p < 0.01$, *** $p < 0.001$. Data in (B) were compared using Wilcoxon test; data in (C)–(E) were compared using a two-way ANOVA with multiple comparisons adjusted by Tukey's HSD; data in (F) were compared with a t test; data in (G) were compared with the log-rank test.



(legend on next page)

p53-dependent replication stress,⁴² and both KEGG terms were enriched in our RNA-seq datasets (Figure 6D), we investigated markers of cell death, cell cycle arrest, DNA damage, and p53 activity. We observed that 2-MiCit increased the number of apoptotic and necrotic cells over time (Figure 6G), reduced the percentage of cells in S-phase (Figures 6H and S6E) and the expression of cell cycle regulators E2F4 and c-Myc (Figure S6F), increased the intensity of the γH2AX DNA damage marker (Figure 6I), increased the number of γH2AX (Figures S6G and S6H) and 53BP1 (Figure S6I) nuclear bodies per cell, the expression of the damage-specific DNA binding protein 2 (DDB2) (Figure S6J), and markers of DNA damage indicative of replication stress, as well as both the intensity of p21 and p53 (Figure 6J) and the transcriptional activity of p53, c-Myc, and E2F4 (Figure S6K). Finally, to investigate the role of p53 in the context of 2-MiCit, we tested the impact of 2-MiCit treatment in WT HCT116 cells and p53-deficient HCT116 p53^(−/−) cells.⁴³ We found that the effect of 2-MiCit treatment on proliferation capacity was greater in p53-deficient cells (Figures 6K and S6L). Finally, we observed a reduced impact of 2-MiCit on mitochondrial respiration in p53^(−/−) cells compared with WT (Figures 6L and S6I), despite no differences observed in mitochondrial H₂O₂ accumulation induced by 2-MiCit (Figures 6M and S6N) between cell lines. Possibly, the reduced impact of 2-MiCit on proliferation of WT cells versus p53^(−/−) may be related to a p53-dependent higher metabolic buffering capacity and direct glycolysis regulation,⁴⁴ as shown by metabolomics of central carbon- and energy-related metabolites (Figure S6O), in particular the glycolytic intermediate glyceraldehyde 3-phosphate. Overall, these data suggest a protective role for p53 against the anti-proliferative effects of 2-MiCit.

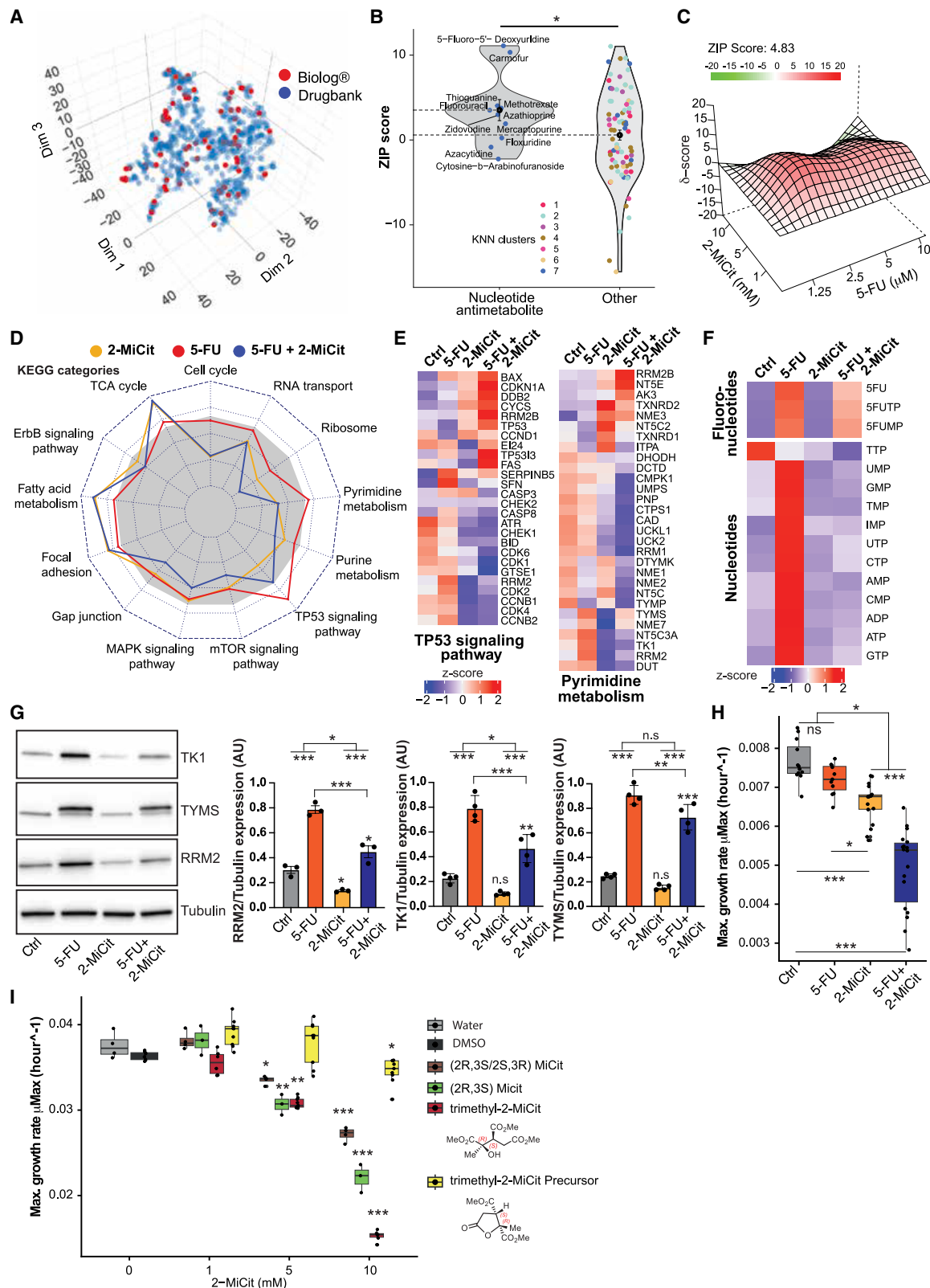
2-MiCit regulates chemotherapy by throttling nucleotide metabolism

To understand the role of 2-MiCit in modulating cancer chemotherapy, we performed a high-throughput screen in HCT116 cells measuring proliferation with four concentrations of 2-MiCit versus four concentrations of 92 anti-cancer therapeutics covering the chemical space represented by the FDA-approved drugs and a diverse set of anti-cancer mechanisms

and targets (Figures 7A, S7A, and S7B) (see STAR Methods and Table S7). We found that 2-MiCit significantly synergized with anti-metabolite drugs from the nucleoside and nucleotide class of compounds, to which 5-FU belongs (zero interaction potency [ZIP] score = 2.79). Other chemically distant functional clusters (KNN clusters) showed either neutral or antagonistic effects (Figures 7B, S7B, and S7C). These findings were further validated using a 4 × 4 matrix of 2-MiCit and 5-FU concentrations, showing that 2-MiCit synergized with 5-FU to inhibit cell growth (ZIP score = 4.83; Figure 7C). To understand how 2-MiCit regulates 5-FU action, we performed proteomics of HCT116 cells treated with either 5-FU and/or 2-MiCit (Figures 7D and 7E; Table S7). Consistent with the role of 2-MiCit inhibiting IDH, we found the TCA cycle to be a significantly enriched KEGG term. Focusing on the interaction between the two compounds, we observed that 2-MiCit abrogated proteomic changes in pyrimidine metabolism and TP53 signaling, two of the most significantly upregulated categories by 5-FU action alone (Figure 6D). We observed that 2-MiCit alone upregulated both p21(CDKN1A) and p53(TP53) and significantly synergized with 5-FU to upregulate these proteins. However, at the pathway level, we observed that 2-MiCit overall antagonized the upregulation of this pathway by 5-FU (Figures 7D and 7E). We also observed that 2-MiCit downregulated most enzymes of pyrimidine ribonucleotide and deoxyribonucleotide metabolism involved in the production of pyrimidine nucleotides and deoxy-nucleotides, as well as those involved in the prodrug metabolism of 5-FU, and antagonized the effect of 5-FU in the upregulation of these proteins (Figure 7E). At the metabolite level, we observed that 5-FU increases the abundance of most nucleotides except for thymidine triphosphate (TTP), a key metabolite for DNA synthesis. By contrast, 2-MiCit decreased nucleotide abundance, consistent with previous data (Figures 6D and 6F), and antagonized the increased levels of nucleotides induced by 5-FU. We also measured activated fluoronucleotides (e.g., 5-FUTP and 5-FUMP) and observed that 2-MiCit decreased activation of the prodrug 5-FU, which is consistent with a downregulation of the enzymes involved in fluoropyrimidine metabolism or uptake (Figures 7E and 7F). Next, we validated our findings using HCT116 spheroids. We observed that similar to the effects in

Figure 6. 2-MiCit impairs mitochondrial respiration and nucleotide metabolism and activates a DNA damage response

- (A) *In vitro* measurements of IDH activity with 2-MiCit.
 - (B) Normalized mitochondrial oxygen consumption rate (OCR) for HCT116 cells treated with 2-MiCit.
 - (C) Targeted metabolomics analysis of HCT116 cells exposed to 10 mM 2-MiCit.
 - (D) RNA-seq functional enrichment of KEGG pathways shared by at least 3 cell lines regulating 2-MiCit effects in CRC cell lines. Color represents statistical significance, with darker tones of blue for smaller *p* values.
 - (E) Metabolite functional enrichment.
 - (F) Abundance of selected metabolite classes. Dot color indicates the fold change of metabolite abundance, with red representing higher abundance in control and blue representing higher abundance in treatment, log2 scale.
 - (G) 2-MiCit treatment induces apoptosis and necrosis in HCT116 cells.
 - (H) 2-MiCit treatment decreases the fraction of HCT116 cells in S-phase.
 - (I) Increased intensity of γH2AX DNA damage marker by 2-MiCit.
 - (J) Increased levels of p53 and p21 in HCT116 cells exposed to 2-MiCit. Representative images of 1,000 HCT116 cells/well. P53 is red, p21 is green, and Hoechst is blue in merged images. Scale bar, 100 μm.
 - (K) Max growth rate of WT and p53-mutated HCT116 cells ± 2-MiCit.
 - (L) Normalized OCR of p53-deficient cells is hampered compared with WT HCT116. Impact of 2-MiCit on mitochondrial respiration is decreased in p53^(−/−) HCT116 cells (see Figure S6I).
 - (M) ROS accumulation in HCT116 and p53^(−/−) cells exposed to 10 and 20 mM 2-MiCit measured by intracellular H₂O₂-sensing HyPer7 probe.
- Data in (H)–(J) are represented as violin or boxplots. NS *p* ≥ 0.05, **p* < 0.05, ***p* < 0.01, ****p* < 0.001 from using a t test; data in (G) and (K)–(M) were compared using two-way ANOVA with multiple comparisons adjusted by Tukey's HSD.



(legend on next page)

2D cell cultures, 2-MiCit antagonized 5-FU upregulation of key enzymes in the pyrimidine pathway (Figure 7G) and synergized with 5-FU in 3D spheroid proliferation (Figures 7H, S7D, and S7E). Altogether, we can conclude that 2-MiCit synergizes with 5-FU through a downregulation of pyrimidine metabolic enzymes and reducing nucleotide metabolism at key metabolic nodes essential for the production of dUMP, the substrate of thymidylate synthase (TYMS), and the target of 5-FU.

Rational chemical design enhances 2-MiCit potency

Finally, we explored the chemical landscape of 2-MiCit to improve its potency. Using synthetic chemistry approaches, we chemically synthesized the pure (2R,3S) enantiomer of 2-MiCit (see STAR Methods for details; Scheme 1), (2R,3S)-2-MiCit, which is the metabolite produced by bacteria, and showed that it is more potent than the commercially available racemic mixture [(2R,3S/2S,3R)-2-MiCit] at inhibiting IDH *in vitro* (Figures S7F and S7G) and in mediating the anti-proliferative effects in cells (Figures 7I and S7H). Next, through tailored organic chemistry routes, we rationally modified the chemical structure of 2-MiCit. The creation of a trimethyl ester of 2-MiCit had a significant anti-proliferative effect in two-dimensional (2D) and 3D cells (Figures 7I and S7I), without an increase of *in vitro* IDH activity (Figure S7G), suggesting that the increased permeability and stereochemical configuration of the methyl group at position 2 of isocitrate are key for its anti-proliferative properties. Overall, this modified trimethyl-2-MiCit compound with enhanced potency may serve as a promising candidate for future research and potential cancer treatment.

DISCUSSION

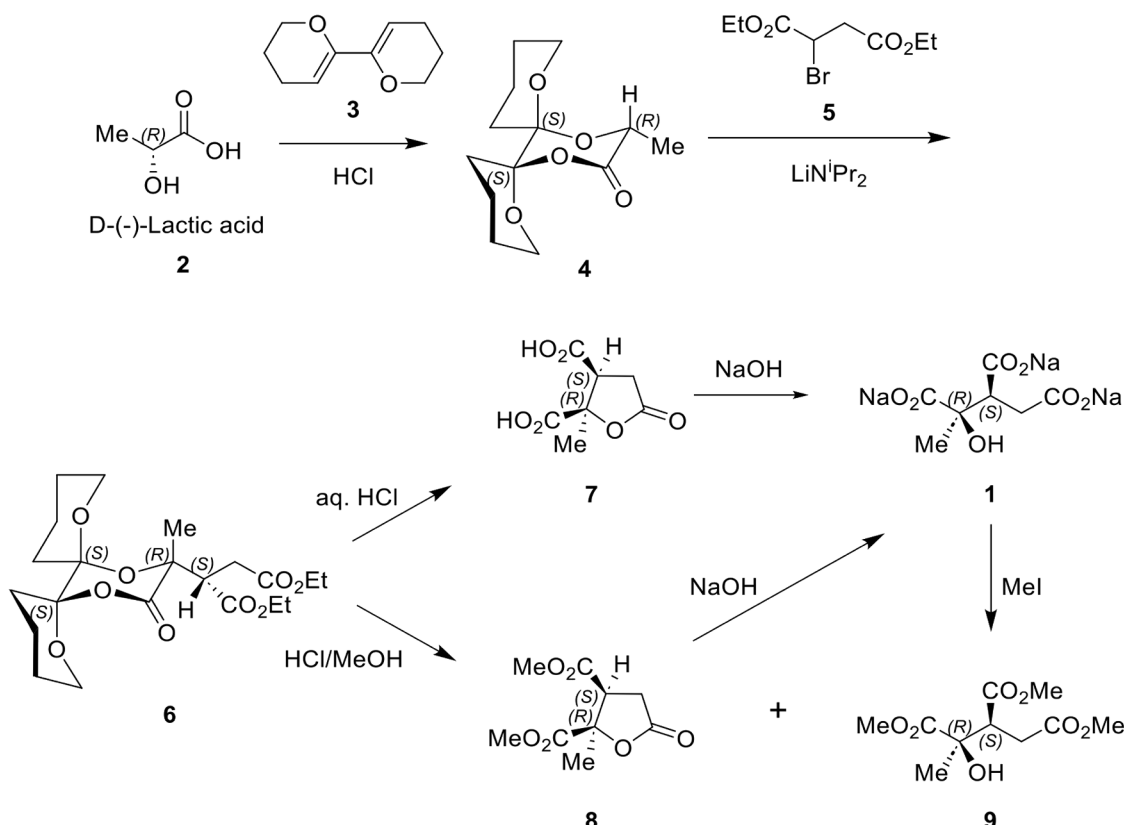
Establishing how diet and microbial metabolites influence host physiology and drug action represents a crucial objective in both fundamental and applied research. This endeavor holds important implications for personalized medicine, offering the potential to revolutionize how we approach healthcare and treatment options in the future. Although numerous studies have explored the potential impact of various dietary components on cancer risk and treatment outcomes,² no scientifically based dietary recommendations exist. Understanding the intricate relationship between diet and cancer requires comprehensive research efforts to

elucidate how dietary factors influence cancer development, the cancer microenvironment including its microbiota, and response to therapy. To address this knowledge gap, we combined a recently published high-throughput host-microbe-drug-nutrient 4-way screen²⁰ with *in silico* human microbiota metabolic modeling and metabolomics to identify bacterial metabolites regulating 5-FU fluoropyrimidine chemotherapy, a mainstay treatment for many cancers, including colorectal and breast cancers. We found that the production of bacterial metabolites regulating 5-FU efficacy was modulated by nutrients that are widely available in our diets, such as pyrimidines, which can be obtained from meats, or glucose and fructose that are widely abundant in western diets. For example, mice fed high-protein diets were shown to be protected against 5-FU toxicity due to an increase in *de novo* pyrimidine synthesis⁴⁵ in diverse organs. Analogously, we find that supplementation with sugars reduces 5-FU toxicity in *C. elegans* through a mechanism that involves the *de novo* synthesis of pyrimidines in microbes but not the host. Conversely, dietary serine alters bacterial one-carbon metabolism, reducing the provision of nucleotides to the host and exacerbating DNA toxicity, leading to host death by 5-FU.³⁰ Consistent with these observations, supplementation with nucleotides rescues 5-FU toxicity in both *C. elegans* (this study, Garcia-Gonzalez et al.,¹³ Scott et al.,¹⁴ and Ke et al.³⁰) and in mice, rats, and humans.^{46–48} Given the important contribution of microbiota nucleotide metabolism on host physiology throughout aging,⁴⁹ it is reasonable to assume a similarly important mechanism in the regulation of 5-FU chemotherapy. Thus, our study dissects the evolutionarily conserved links between microbe-derived metabolites and the host and their modulation by environmental cues, such as drugs and nutrition.

Another key metabolite identified in this study that regulates 5-FU efficacy is a metabolite derived from the methylcitrate cycle. 2-MiCit is produced by microorganisms, including bacteria and fungi, as a strategy to detoxify elevated concentrations of propionic acid, a short-chain fatty acid produced in the proximal colon by the gut microbiota in concentrations ranging from 14 to 28 mM.⁵⁰ In the past, a study of propionate toxicity identified 2-MiCit as a potent inhibitor of *Salmonella enterica*.⁵¹ This finding may implicate the methylcitrate cycle as a defense mechanism by commensal microbes and its respective metabolites as part of the arsenal of toxic molecules produced by commensals to protect themselves against invading

Figure 7. Drug efficacy of 2-MiCit is increased in the presence of 5-FU or by chemical modifications

- (A) Drugs of Biolog assay plates (red) span a vast chemical space indicated by DrugBank drugs in blue. t-SNE representation of compounds' chemical fingerprints from the DrugBank database and Biolog plates.
 - (B) Zero interaction potency (ZIP) score of Biolog drugs tested with 2-MiCit. A positive ZIP score indicates a synergistic interaction between the two compounds.
 - (C) ZIP score 3D landscape of a 4 × 4 drug interaction matrix of HCT116 cells treated with 5-FU and 2-MiCit. Color represents ZIP synergy score, and red indicates a positive synergy and green a negative synergy, linear scale with arbitrary units.
 - (D) Radar plot of the average log₂FC effect (versus control) of the genes enriched in the KEGG pathway categories from HCT116 cells treated with 1.25 μM 5-FU and/or 10 mM 2-MiCit. Gray area marks the threshold of log₂FC = 0.
 - (E) Heatmap of proteomics data for two key KEGG pathways from (D). Color represents the Z score of protein intensity, ranging from red (positive Z score) to blue (negative Z score), linear scale.
 - (F) (Fluoro-) nucleotide profiling of HCT116 cells treated with 1.25 μM 5-FU and 10 mM 2-MiCit. Color represents the Z score of protein intensity, ranging from red (positive Z score) to blue (negative Z score), linear scale.
 - (G) Protein blotting and quantification of thymidine kinase 1 (TK1), thymidylate synthase (TYMS), and ribonucleotide reductase regulatory subunit M2 (RRM2) in HCT116 tumor spheroids after treatment with 1.25 μM 5-FU and 10 mM 2-MiCit.
 - (H) Max growth rate represented as boxplots of HCT116 spheroids upon treatment with 1.25 μM 5-FU and/or 10 mM 2-MiCit.
 - (I) Max growth rate represented as boxplots of HCT116 cells upon treatment with 0, 1, 5, and 10 mM of each of the modified chemical versions.
- Data are means ± SD. NS $p \geq 0.05$, * $p < 0.05$, ** $p < 0.01$, *** $p < 0.001$ using two-way ANOVA. Data in (B) were tested by comparing the “nucleotide anti-metabolite” class against the null model of the full distribution.



Scheme 1. Synthesis of dimethyl (2R,3S)-2-methyl-5-oxotetrahydrofuran-2,3-dicarboxylate 8 and trimethyl (2S,3R)-3-hydroxybutane-1,2,3-tricarboxylate 9

pathogens. Interestingly, little is known about the role of 2-MiCit in the regulation of the biological activity of host cells. Our detailed mechanistic investigation in this study points to 2-MiCit as a cancer-enriched, bacterially produced metabolite modulating the effects of cell proliferation and anti-cancer chemotherapy. A recent report shows that closely related bacteria can have distinct effects on CRC cell growth, with most inactivated bacterial cells impairing growth, while 50% of secretomes promote growth and the other 50% impairing growth.⁵² Also, effects on growth observed per bacterial strain were cancer cell-type specific. Likewise, we observed a proliferative effect of 2-MiCit in two cell lines, while an anti-proliferative effect was observed in 16 cell types with variable impact. Our combined results paint a complex scenario where microbial-derived metabolites can impact cell proliferation in different ways depending on the cell type on which they exert action. Further, we found 2-MiCit acts synergistically with fluoropyrimidine drugs while acting antagonistically to alkylating drugs (Figures 7 and S7). Our work allows us to conclude that the identification of specific microbial species and/or their metabolites that modulate cancer cell proliferation and drug responses could in the future inform personalized treatment approaches tailored to individual patients based on their microbiome and cancer-associated microbiome profiles.

An emerging concept in biology is the relationship between metabolism and DNA repair and replication mechanisms.⁵³

Recent research highlights the vital role of p53 in coordinating processes such as cell division, DNA damage response, and cell death with cellular energy production and metabolism. The gut microbiome was shown to switch mutant p53 from tumor-suppressive to oncogenic.⁵⁴ However, no studies to date have looked at the relationship between metabolites from the cancer-associated microbiota and the roles of p53. Here, we show that 2-MiCit arrests cell cycle progression, induces DNA damage, upregulates p53, and impairs cell proliferation. We observed that 2-MiCit had a stronger effect in slowing cellular division of $\text{p53}^{(-/-)}$ -deficient cells. Since 2-MiCit impacts cellular metabolism and respiration through the inhibition of the TCA cycle enzyme IDH, a likely explanation for these effects results from the reduced mitochondrial metabolic capacity observed in $\text{p53}^{(-/-)}$ -deficient cells. This is consistent with a protective cellular role of p53 in mediating a connection between metabolism and cell proliferation,⁵³ rather than a direct role for p53 in arresting cellular division induced by 2-MiCit, which may be driven by c-Myc and E2F4, two key cell cycle regulators found downregulated by 2-MiCit treatment. In response to DNA damage or oxidative stress, p53 has previously been shown to redirect glucose toward the pentose phosphate pathway (PPP) through glycolysis suppression. Consistent with this, we observe a strong decrease in glyceraldehyde 3-phosphate in p53-deficient cells compared with WT cells treated with 2-MiCit. This metabolic plasticity enables cells to obtain nucleotide precursors essential for repairing DNA.⁵³ Likewise, we show that

5-FU rewires metabolism for increased nucleotide abundance. However, we observe that this phenomenon occurs in a p53-independent manner (Figures 7F and S7I). Further, 2-MiCit synergizes 5-FU effects by upregulating pro-apoptotic proteins while downregulating cell cycle proteins and throttling the expression of key proteins necessary to produce pyrimidine metabolites. These combined effects likely explain the anti-proliferation synergistic effects observed between 2-MiCit and 5-FU. Our data imply that unexplored host-microbe context-dependent roles for p53 may exist at the nexus of DNA damage and metabolism in a cancer cell-dependent manner and suggest an important role for other regulators of 2-MiCit effects in cellular metabolism and proliferation, which remains unexplored.

Modification of chemotherapeutic drugs to increase their efficacy is a key area of research with the aim of improving clinical outcomes for cancer patients. In the past, combination therapies were commonly used approaches in the clinic to enhance the efficacy of cancer drugs. This includes the combination of drugs or supplements with complementary mechanisms of action targeting multiple signaling pathways to impede cancer progression. One example is the use of FOLFOX, a combination of the supplement folic acid with the drugs 5-FU and oxaliplatin, the first-line chemotherapy treatment for metastatic colorectal cancer.⁵⁵ Akin to these studies, here we show that the microbial metabolite 2-MiCit is an effective combinatorial agent with a distinct metabolic signature that antagonizes the cellular survival strategy activated upon 5-FU challenge, ultimately increasing its potency. Another strategy is the structural modification of drugs, whereby altering the chemical structure of a compound may improve its potency, specificity, and stability. Here, we show that the conversion of 2-MiCit into its trimethyl ester (trimethyl (2R,3S)-2-MiCit) strongly increased potency. Therefore, refining existing therapies for cancer requires a multidisciplinary systems approach that integrates insights from basic science, pharmacology, and chemistry.

Limitations of the study

The limitations of this study should be considered in the context of its clinical relevance and its translation to humans. While the findings regarding the production of 2-MiCit by bacteria provide valuable and unique biological insights into its function and regulation of chemotherapy, the generalizability to patient populations may be limited due to the study's specific use of published microbiome datasets based on samples that have not been originally collected for the direct purposes of this study. Furthermore, the study's design with the utilization of invertebrate models and *in vitro* cell work may not fully capture the dynamics, the outcomes, or the effects of treatment in real-world clinical settings. These limitations highlight the need for further experimental research, including the use of mammalian systems and additional methodologies to confirm the applicability of these findings in routine clinical practice.

RESOURCE AVAILABILITY

Lead contact

Further information and requests for resources and reagents should be directed to and will be fulfilled by the lead contact, Filipe Cabreiro (f.cabreiro@uni-koeln.de).

Materials availability

All *E. coli* strains generated in this study will be made available upon request to the [lead contact](#).

Data and code availability

Metabolomics, proteomics, and RNA-seq data have been deposited at GEO, PRIDE, and MetaboLights and are publicly available as of the date of publication. Accession numbers are listed in the [key resources table](#). This paper analyzes existing, publicly available data. These accession numbers for the datasets are listed in the [key resources table](#). Any additional information required to reanalyze the data reported in this paper is available from the [lead contact](#) upon request. Original code has been deposited at GitHub (https://github.com/Cabreiro-Lab/micit_cancer_code/) and is publicly available as of the date of publication. Any additional information required to reanalyze the data reported in this paper is available from the [lead contact](#) upon request. DOIs are listed in the [key resources table](#).

ACKNOWLEDGMENTS

F.C. was supported by the Wellcome Trust/Royal Society (grant numbers 102532/Z/12/Z and 102531/Z/13/A), the DFG German Research Foundation (grant number EXC 2030-390661388), and the Center for Molecular Medicine Cologne (grant number IPFP-B02). D.M.-M. was supported by the Leverhulme Trust (grant number RPG-2022-299). H.M.C. is funded by the Medical Research Council (grant number MC-A654-5QB90). J.R.M. and the Division of Digestive Diseases at Imperial College London receive financial and infrastructure support from the NIHR Imperial Biomedical Research Centre based at Imperial College Healthcare NHS Trust and Imperial College London. Some strains were provided by the Caenorhabditis Genetics Center (CGC), which is funded by the NIH Office of Research Infrastructure Programs (grant number P40 OD010440). We thank Professor Bert Vogelstein (Johns Hopkins University School of Medicine, Baltimore, MD) for generously gifting the HCT116 p53^(−/−) cell line. We thank Dr. Nikos Oikonomou at the CECAD FACS facility for the support in flow cytometry experiments. Some graphics in the graphical abstract were created with [BioRender.com](#). This work was supported by the DFG Research Infrastructure West German Genome Center (project 407493903) as part of the Next Generation Sequencing Competence Network (project 423957469). NGS analyses were carried out at the production site in Cologne (Cologne Center for Genomics [CCG]).

AUTHOR CONTRIBUTIONS

Conceptualization, D.M.-M., T.V.P., and F.C.; methodology, B.T.G.; software, D.M.-M., K.G., L.B., M.C., J.Z., G.M., A.M., S.B., J.B.M., and C.K.; formal analysis, D.M.-M., T.V.P., K.G., L.Q., M.C., L.B., J.Z., G.M., A.M., S.B., B.Z., H.M.C., and F.C.; investigation, D.M.-M., T.V.P., K.G., L.Q., C.C., S.J.C., L.B., J.Z., G.M., D.C., M.Z., T.S., I.A., A.S., M.B., and H.M.C.; supervision, J.R.M., S.H., H.K., C.K., A.R.B., B.T.G., C.F., H.M.C., and F.C.; writing, D.M.-M., T.V.P., K.G., and F.C.; funding acquisition, F.C.; project administration, F.C.

DECLARATION OF INTERESTS

J.R.M. has previously received consultancy fees from Cultech Ltd. and Enterobiotix Ltd.

STAR METHODS

Detailed methods are provided in the online version of this paper and include the following:

- [KEY RESOURCES TABLE](#)
- [EXPERIMENTAL MODEL AND STUDY PARTICIPANT DETAILS](#)
 - Culturing of bacterial and *C. elegans* strains
 - Human cell lines and spheroids
 - *Drosophila* husbandry and genetics
 - Human cohorts
 - French and German cohort
 - Italian cohort

- Japanese cohort
- Chinese cohort
- Netherlands cohort
- **METHOD DETAILS**
 - Bacterial IC₅₀ assays
 - LC-MS/MS method for nucleotide and fluoronucleotide quantification
 - Metabolic models
 - Cancer cell lines
 - Drug-drug interaction
 - Chemical space representation of the drug space
 - RNA sequencing and analysis
 - Metabolomic analysis
 - Bacterial sample preparation for fully quantitative and comparative metabolomics
 - Comprehensive targeted metabolomic analysis/LC-MS in cells
 - Proteomics analysis in HCT116 cells
 - Sample processing
 - Liquid chromatography-tandem mass spectrometry (LC-MS/MS) analysis
 - Data processing
 - Western blot
 - DNA damage dynamics
 - Annexin V/PI staining
 - Cell cycle profiling
 - HyPer7 measurement
 - Seahorse
 - *In vitro* IDH activity assay
 - Replication stress analysis
 - Synthetic chemistry
- **QUANTIFICATION AND STATISTICAL ANALYSIS**
 - General

SUPPLEMENTAL INFORMATION

Supplemental information can be found online at <https://doi.org/10.1016/j.cels.2025.101397>.

Received: April 24, 2024

Revised: June 6, 2025

Accepted: August 18, 2025

Published: September 10, 2025

REFERENCES

1. Hanahan, D. (2022). Hallmarks of Cancer: New Dimensions. *Cancer Discov.* 12, 31–46. <https://doi.org/10.1158/2159-8290.CD-21-1059>.
2. Gonzalez, P.S., O’Prey, J., Cardaci, S., Barthet, V.J.A., Sakamaki, J.I., Beaumatin, F., Roseweir, A., Gay, D.M., Mackay, G., Malviya, G., et al. (2018). Mannose impairs tumour growth and enhances chemotherapy. *Nature* 563, 719–723. <https://doi.org/10.1038/s41586-018-0729-3>.
3. Wu, G.D., Chen, J., Hoffmann, C., Bittinger, K., Chen, Y.Y., Keilbaugh, S.A., Bewtra, M., Knights, D., Walters, W.A., Knight, R., et al. (2011). Linking long-term dietary patterns with gut microbial enterotypes. *Science* 334, 105–108. <https://doi.org/10.1126/science.1208344>.
4. Javaheri, A., Kruse, T., Moonens, K., Mejías-Luque, R., Debraekeleer, A., Asche, C.I., Tegtmeier, N., Kalali, B., Bach, N.C., Sieber, S.A., et al. (2016). *Helicobacter pylori* adhesin HopQ engages in a virulence-enhancing interaction with human CEACAMs. *Nat. Microbiol.* 2, 16189. <https://doi.org/10.1038/nmicrobiol.2016.189>.
5. Wilson, M.R., Jiang, Y., Villalta, P.W., Stornetta, A., Boudreau, P.D., Carrá, A., Brennan, C.A., Chun, E., Ngo, L., Samson, L.D., et al. (2019). The human gut bacterial genotoxin colibactin alkylates DNA. *Science* 363, eaar7785. <https://doi.org/10.1126/science.aar7785>.
6. Liu, X.F., Xiang, L., Zhou, Q., Carralot, J.P., Prunotto, M., Niederfellner, G., and Pastan, I. (2016). Actinomycin D enhances killing of cancer cells by immunotoxin RG7787 through activation of the extrinsic pathway of apoptosis. *Proc. Natl. Acad. Sci. USA* 113, 10666–10671. <https://doi.org/10.1073/pnas.1611481113>.
7. Luo, M., Wang, F., Zhang, H., To, K.K.W., Wu, S., Chen, Z., Liang, S., and Fu, L. (2020). Mitomycin C enhanced the efficacy of PD-L1 blockade in non-small cell lung cancer. *Signal Transduct. Target. Ther.* 5, 141. <https://doi.org/10.1038/s41392-020-0200-4>.
8. Stierle, A., Strobel, G., and Stierle, D. (1993). Taxol and taxane production by *Taxomyces andreanae*, an endophytic fungus of Pacific yew. *Science* 260, 214–216. <https://doi.org/10.1126/science.8097061>.
9. Liu, Y., Lau, H.C.H., and Yu, J. (2023). Microbial metabolites in colorectal tumorigenesis and cancer therapy. *Gut Microbes* 15, 2203968. <https://doi.org/10.1080/19490976.2023.2203968>.
10. Cui, W., Guo, M., Liu, D., Xiao, P., Yang, C., Huang, H., Liang, C., Yang, Y., Fu, X., Zhang, Y., et al. (2024). Gut microbial metabolite facilitates colorectal cancer development via ferroptosis inhibition. *Nat. Cell Biol.* 26, 124–137. <https://doi.org/10.1038/s41556-023-01314-6>.
11. Yang, Q., Wang, B., Zheng, Q., Li, H., Meng, X., Zhou, F., and Zhang, L. (2023). A Review of Gut Microbiota-Derived Metabolites in Tumor Progression and Cancer Therapy. *Adv. Sci.* 10, e2207366. <https://doi.org/10.1002/advs.202207366>.
12. Maier, L., Pruteanu, M., Kuhn, M., Zeller, G., Telzerow, A., Anderson, E.E., Brochado, A.R., Fernandez, K.C., Dose, H., Mori, H., et al. (2018). Extensive impact of non-antibiotic drugs on human gut bacteria. *Nature* 555, 623–628. <https://doi.org/10.1038/nature25979>.
13. García-González, A.P., Ritter, A.D., Shrestha, S., Andersen, E.C., Yilmaz, L.S., and Walhout, A.J.M. (2017). Bacterial Metabolism Affects the *C. elegans* Response to Cancer Chemotherapeutics. *Cell* 169, 431–441.e8. <https://doi.org/10.1016/j.cell.2017.03.046>.
14. Scott, T.A., Quintaneiro, L.M., Norvaisas, P., Lui, P.P., Wilson, M.P., Leung, K.Y., Herrera-Dominguez, L., Sudiwala, S., Pessia, A., Clayton, P.T., et al. (2017). Host-Microbe Co-metabolism Dictates Cancer Drug Efficacy in *C. elegans*. *Cell* 169, 442–456.e18. <https://doi.org/10.1016/j.cell.2017.03.040>.
15. Tintelnot, J., Xu, Y., Lesker, T.R., Schönlein, M., Konczalla, L., Giannou, A.D., Pelczar, P., Kyries, D., Puelles, V.G., Bielecka, A.A., et al. (2023). Microbiota-derived 3-IAA influences chemotherapy efficacy in pancreatic cancer. *Nature* 615, 168–174. <https://doi.org/10.1038/s41586-023-05728-y>.
16. Zimmermann, M., Zimmermann-Kogadeeva, M., Wegmann, R., and Goodman, A.L. (2019). Separating host and microbiome contributions to drug pharmacokinetics and toxicity. *Science* 363, eaat9931. <https://doi.org/10.1126/science.aat9931>.
17. Spanogiannopoulos, P., Kyaw, T.S., Guthrie, B.G.H., Bradley, P.H., Lee, J.V., Melamed, J., Malig, Y.N.A., Lam, K.N., Gempis, D., Sandy, M., et al. (2022). Host and gut bacteria share metabolic pathways for anti-cancer drug metabolism. *Nat. Microbiol.* 7, 1605–1620. <https://doi.org/10.1038/s41564-022-01226-5>.
18. Wallace, B.D., Wang, H., Lane, K.T., Scott, J.E., Orans, J., Koo, J.S., Venkatesh, M., Jobin, C., Yeh, L.A., Mani, S., and Redlinbo, M.R. (2010). Alleviating cancer drug toxicity by inhibiting a bacterial enzyme. *Science* 330, 831–835. <https://doi.org/10.1126/science.1191175>.
19. Klünemann, M., Andrejev, S., Blasche, S., Mateus, A., Phapale, P., Devendran, S., Vappiani, J., Simon, B., Scott, T.A., Kafkia, E., et al. (2021). Bioaccumulation of therapeutic drugs by human gut bacteria. *Nature* 597, 533–538. <https://doi.org/10.1038/s41586-021-03891-8>.
20. Pryor, R., Norvaisas, P., Marinos, G., Best, L., Thingholm, L.B., Quintaneiro, L.M., De Haes, W., Esser, D., Waschina, S., Lujan, C., et al. (2019). Host-Microbe-Drug-Nutrient Screen Identifies Bacterial Effectors of Metformin Therapy. *Cell* 178, 1299–1312.e29. <https://doi.org/10.1016/j.cell.2019.08.003>.
21. Clayton, T.A., Baker, D., Lindon, J.C., Everett, J.R., and Nicholson, J.K. (2009). Pharmacometabolic identification of a significant host-microbiome metabolic interaction affecting human drug metabolism. *Proc. Natl. Acad. Sci. USA* 106, 14728–14733. <https://doi.org/10.1073/pnas.0904489106>.

22. Sieow, B.F.L., Wun, K.S., Yong, W.P., Hwang, I.Y., and Chang, M.W. (2021). Tweak to Treat: Reprogramming Bacteria for Cancer Treatment. *Trends Cancer* 7, 447–464. <https://doi.org/10.1016/j.trecan.2020.11.004>.
23. Hahn, J., Ding, S., Im, J., Harimoto, T., Leong, K.W., and Danino, T. (2024). Bacterial therapies at the interface of synthetic biology and nanomedicine. *Nat. Rev. Bioeng.* 2, 120–135. <https://doi.org/10.1038/s44222-023-00119-4>.
24. Gurbatri, C.R., Lia, I., Vincent, R., Coker, C., Castro, S., Treuting, P.M., Hinchliffe, T.E., Arpaia, N., and Danino, T. (2020). Engineered probiotics for local tumor delivery of checkpoint blockade nanobodies. *Sci. Transl. Med.* 12, eaax0876. <https://doi.org/10.1126/scitranslmed.aax0876>.
25. Leventhal, D.S., Sokolovska, A., Li, N., Plescia, C., Kolodziej, S.A., Gallant, C.W., Christmas, R., Gao, J.R., James, M.J., Abin-Fuentes, A., et al. (2020). Immunotherapy with engineered bacteria by targeting the STING pathway for anti-tumor immunity. *Nat. Commun.* 11, 2739. <https://doi.org/10.1038/s41467-020-16602-0>.
26. Chiang, C.J., and Huang, P.H. (2021). Metabolic engineering of probiotic *Escherichia coli* for cytolytic therapy of tumors. *Sci. Rep.* 11, 5853. <https://doi.org/10.1038/s41598-021-85372-6>.
27. Ho, C.L., Tan, H.Q., Chua, K.J., Kang, A., Lim, K.H., Ling, K.L., Yew, W.S., Lee, Y.S., Thiery, J.P., and Chang, M.W. (2018). Engineered commensal microbes for diet-mediated colorectal-cancer chemoprevention. *Nat. Biomed. Eng.* 2, 27–37. <https://doi.org/10.1038/s41551-017-0181-y>.
28. Leulier, F., MacNeil, L.T., Lee, W.J., Rawls, J.F., Cani, P.D., Schwarzer, M., Zhao, L., and Simpson, S.J. (2017). Integrative Physiology: At the Crossroads of Nutrition, Microbiota, Animal Physiology, and Human Health. *Cell Metab.* 25, 522–534. <https://doi.org/10.1016/j.cmet.2017.02.001>.
29. Backes, C., Martinez-Martinez, D., and Cabreiro, F. (2021). *C. elegans*: A biosensor for host-microbe interactions. *Lab Anim.* 50, 127–135. <https://doi.org/10.1038/s41684-021-00724-z>.
30. Ke, W., Saba, J.A., Yao, C.H., Hilzendeger, M.A., Drangowska-Way, A., Joshi, C., Mony, V.K., Benjamin, S.B., Zhang, S., Locasale, J., et al. (2020). Dietary serine-microbiota interaction enhances chemotherapeutic toxicity without altering drug conversion. *Nat. Commun.* 11, 2587. <https://doi.org/10.1038/s41467-020-16220-w>.
31. Battaglia, T.W., Mimpel, I.L., Traets, J.J.H., van Hoeck, A., Zeverijn, L.J., Geurts, B.S., de Wit, G.F., Noë, M., Hofland, I., Vos, J.L., et al. (2024). A pan-cancer analysis of the microbiome in metastatic cancer. *Cell* 187, 2324–2335.e19. <https://doi.org/10.1016/j.cell.2024.03.021>.
32. Nejman, D., Livyatan, I., Fuks, G., Gavert, N., Zwang, Y., Geller, L.T., Rotter-Maskowitz, A., Weiser, R., Mallel, G., Gigi, E., et al. (2020). The human tumor microbiome is composed of tumor type-specific intracellular bacteria. *Science* 368, 973–980. <https://doi.org/10.1126/science.aya9189>.
33. Chubukov, V., Gerosa, L., Kochanowski, K., and Sauer, U. (2014). Coordination of microbial metabolism. *Nat. Rev. Microbiol.* 12, 327–340. <https://doi.org/10.1038/nrmicro3238>.
34. Huang, Z., Wang, Q., Khan, I.A., Li, Y., Wang, J., Wang, J., Liu, X., Lin, F., and Lu, J. (2023). The Methylcitrate Cycle and Its Crosstalk with the Glyoxylate Cycle and Tricarboxylic Acid Cycle in Pathogenic Fungi. *Molecules* 28, 6667. <https://doi.org/10.3390/molecules28186667>.
35. Thomas, A.M., Manghi, P., Asnicar, F., Pasolli, E., Armanini, F., Zolfo, M., Beghini, F., Manara, S., Karcher, N., Pozzi, C., et al. (2019). Metagenomic analysis of colorectal cancer datasets identifies cross-cohort microbial diagnostic signatures and a link with choline degradation. *Nat. Med.* 25, 667–678. <https://doi.org/10.1038/s41591-019-0405-7>.
36. Yachida, S., Mizutani, S., Shiroma, H., Shiba, S., Nakajima, T., Sakamoto, T., Watanabe, H., Masuda, K., Nishimoto, Y., Kubo, M., et al. (2019). Metagenomic and metabolomic analyses reveal distinct stage-specific phenotypes of the gut microbiota in colorectal cancer. *Nat. Med.* 25, 968–976. <https://doi.org/10.1038/s41591-019-0458-7>.
37. Yang, Y., Du, L., Shi, D., Kong, C., Liu, J., Liu, G., Li, X., and Ma, Y. (2021). Dysbiosis of human gut microbiome in young-onset colorectal cancer. *Nat. Commun.* 12, 6757. <https://doi.org/10.1038/s41467-021-27112-y>.
38. Zeller, G., Tap, J., Voigt, A.Y., Sunagawa, S., Kultima, J.R., Costea, P.I., Amiot, A., Böhm, J., Brunetti, F., Habermann, N., et al. (2014). Potential of fecal microbiota for early-stage detection of colorectal cancer. *Mol. Syst. Biol.* 10, 766. <https://doi.org/10.1525/msb.20145645>.
39. Louis, P., and Flint, H.J. (2017). Formation of propionate and butyrate by the human colonic microbiota. *Environ. Microbiol.* 19, 29–41. <https://doi.org/10.1111/1462-2920.13589>.
40. Bangi, E., Murgia, C., Teague, A.G.S., Sansom, O.J., and Cagan, R.L. (2016). Functional exploration of colorectal cancer genomes using *Drosophila*. *Nat. Commun.* 7, 13615. <https://doi.org/10.1038/ncomms13615>.
41. Brock, M. (2005). Generation and phenotypic characterization of *Aspergillus nidulans* methylisocitrate lyase deletion mutants: methylisocitrate inhibits growth and conidiation. *Appl. Environ. Microbiol.* 71, 5465–5475. <https://doi.org/10.1128/AEM.71.9.5465-5475.2005>.
42. Linke, S.P., Clarkin, K.C., Di Leonardo, A., Tsou, A., and Wahl, G.M. (1996). A reversible, p53-dependent G0/G1 cell cycle arrest induced by ribonucleotide depletion in the absence of detectable DNA damage. *Genes Dev.* 10, 934–947. <https://doi.org/10.1101/gad.10.8.934>.
43. Davis, R.J., Gönen, M., Margineantu, D.H., Handeli, S., Swanger, J., Hoellerbauer, P., Paddison, P.J., Gu, H., Raftery, D., Grim, J.E., et al. (2018). Pan-cancer transcriptional signatures predictive of oncogenic mutations reveal that *Fbw7* regulates cancer cell oxidative metabolism. *Proc. Natl. Acad. Sci. USA* 115, 5462–5467. <https://doi.org/10.1073/pnas.1718338115>.
44. Bensaad, K., Tsuruta, A., Selak, M.A., Vidal, M.N.C., Nakano, K., Bartrons, R., Gottlieb, E., and Vousden, K.H. (2006). TIGAR, a p53-inducible regulator of glycolysis and apoptosis. *Cell* 126, 107–120. <https://doi.org/10.1016/j.cell.2006.05.036>.
45. Zaharevitz, D.W., Grubb, M.F., Hyman, R., Chisena, C., and Cysyk, R.L. (1993). Effect of high-protein diet on pyrimidine synthesis and response to PALA in mouse tissues. *J. Natl. Cancer Inst.* 85, 662–666. <https://doi.org/10.1093/jnci/85.8.662>.
46. Bagrij, T., Kralovanszky, J., Gyergyay, F., Kiss, E., and Peters, G.J. (1993). Influence of uridine treatment in mice on the protection of gastrointestinal toxicity caused by 5-fluorouracil. *Anticancer Res.* 13, 789–793.
47. Kralovanszky, J., Prajda, N., Kerpel-Fronius, S., Bagrij, T., Kiss, E., and Peters, G.J. (1993). Biochemical consequences of 5-fluorouracil gastrointestinal toxicity in rats; effect of high-dose uridine. *Cancer Chemother. Pharmacol.* 32, 243–248. <https://doi.org/10.1007/BF00685843>.
48. van Groeningen, C.J., Peters, G.J., and Pinedo, H.M. (1993). Reversal of 5-fluorouracil-induced toxicity by oral administration of uridine. *Ann. Oncol.* 4, 317–320. <https://doi.org/10.1093/oxfordjournals.annonc.a058490>.
49. Best, L., Dost, T., Esser, D., Flor, S., Gamarra, A.M., Haase, M., Kadibalban, A.S., Marinoss, G., Walker, A., Zimmermann, J., et al. (2025). Metabolic modelling reveals the aging-associated decline of host-microbiome metabolic interactions in mice. *Nat. Microbiol.* 10, 973–991. <https://doi.org/10.1038/s41564-025-01959-z>.
50. Cong, J., Zhou, P., and Zhang, R. (2022). Intestinal Microbiota-Derived Short Chain Fatty Acids in Host Health and Disease. *Nutrients* 14, 1977. <https://doi.org/10.3390/nu14091977>.
51. Horswill, A.R., Dudding, A.R., and Escalante-Semerena, J.C. (2001). Studies of propionate toxicity in *Salmonella enterica* identify 2-methylcitrate as a potent inhibitor of cell growth. *J. Biol. Chem.* 276, 19094–19101. <https://doi.org/10.1074/jbc.M100244200>.
52. Taddese, R., Garza, D.R., Ruiter, L.N., de Jonge, M.I., Belzer, C., Aalvink, S., Nagtegaal, I.D., Dutilh, B.E., and Boleij, A. (2020). Growth rate alterations of human colorectal cancer cells by 157 gut bacteria. *Gut Microbes* 12, 1–20. <https://doi.org/10.1080/19490976.2020.1799733>.
53. Cucchi, D., Gibson, A., and Martin, S.A. (2021). The emerging relationship between metabolism and DNA repair. *Cell Cycle* 20, 943–959. <https://doi.org/10.1080/15384101.2021.1912889>.

54. Kadosh, E., Snir-Alkalay, I., Venkatachalam, A., May, S., Lasy, A., Elyada, E., Zinger, A., Shaham, M., Vaalani, G., Mernberger, M., et al. (2020). The gut microbiome switches mutant p53 from tumour-suppressive to oncogenic. *Nature* 586, 133–138. <https://doi.org/10.1038/s41586-020-2541-0>.
55. Chua, W., Goldstein, D., Lee, C.K., Dhillon, H., Michael, M., Mitchell, P., Clarke, S.J., and Iacopetta, B. (2009). Molecular markers of response and toxicity to FOLFOX chemotherapy in metastatic colorectal cancer. *Br. J. Cancer* 101, 998–1004. <https://doi.org/10.1038/sj.bjc.6605239>.
56. Darley, D.J., Selmer, T., Clegg, W., Harrington, R.W., Buckel, W., and Golding, B.T. (2003). Stereocontrolled Synthesis of (2R,3S)-2-Methylisocitrate, a Central Intermediate in the Methylcitrate Cycle. *Helv. Chim. Acta* 86, 3991–3999. <https://doi.org/10.1002/hlca.200390332>.
57. Martin, M. (2011). Cutadapt removes adapter sequences from high-throughput sequencing reads. *EMBnet J.* 17, 10–12. <https://doi.org/10.14806/ej.17.1.200>.
58. Schmieder, R., and Edwards, R. (2011). Quality control and preprocessing of metagenomic datasets. *Bioinformatics* 27, 863–864. <https://doi.org/10.1093/bioinformatics/btr026>.
59. Langmead, B., and Salzberg, S.L. (2012). Fast gapped-read alignment with Bowtie 2. *Nat. Methods* 9, 357–359. <https://doi.org/10.1038/nmeth.1923>.
60. Zimmermann, J., Kaleta, C., and Waschyna, S. (2021). gapseq: informed prediction of bacterial metabolic pathways and reconstruction of accurate metabolic models. *Genome Biol.* 22, 81. <https://doi.org/10.1186/s13059-021-02295-1>.
61. Gelius-Dietrich, G., Desouki, A.A., Fritzemeier, C.J., and Lercher, M.J. (2013). Sybil-efficient constraint-based modelling in R. *BMC Syst. Biol.* 7, 125. <https://doi.org/10.1186/1752-0509-7-125>.
62. Hall, B.G., Acar, H., Nandipati, A., and Barlow, M. (2014). Growth rates made easy. *Mol. Biol. Evol.* 31, 232–238. <https://doi.org/10.1093/molbev/mst187>.
63. Ianevski, A., Giri, A.K., and Aittokallio, T. (2020). SynergyFinder 2.0: visual analytics of multi-drug combination synergies. *Nucleic Acids Res.* 48, W488–W493. <https://doi.org/10.1093/nar/gkaa216>.
64. Bolger, A.M., Lohse, M., and Usadel, B. (2014). Trimmomatic: a flexible trimmer for Illumina sequence data. *Bioinformatics* 30, 2114–2120. <https://doi.org/10.1093/bioinformatics/btu170>.
65. Patro, R., Duggal, G., Love, M.I., Irizarry, R.A., and Kingsford, C. (2017). Salmon provides fast and bias-aware quantification of transcript expression. *Nat. Methods* 14, 417–419. <https://doi.org/10.1038/nmeth.4197>.
66. Love, M.I., Huber, W., and Anders, S. (2014). Moderated estimation of fold change and dispersion for RNA-seq data with DESeq2. *Genome Biol.* 15, 550. <https://doi.org/10.1186/s13059-014-0550-8>.
67. Wickham, H., Averick, M., Bryan, J., Chang, W., McGowan, L., François, R., Grolemund, G., Hayes, A., Henry, L., Hester, J., et al. (2019). Welcome to the Tidyverse. *J. Open Source Software* 4, 1686. <https://doi.org/10.21105/joss.01686>.
68. Garcia-Alonso, L., Holland, C.H., Ibrahim, M.M., Turei, D., and Saez-Rodriguez, J. (2019). Benchmark and integration of resources for the estimation of human transcription factor activities. *Genome Res.* 29, 1363–1375. <https://doi.org/10.1101/gr.240663.118>.
69. Pang, Z., Chong, J., Zhou, G., de Lima Morais, D.A., Chang, L., Barrette, M., Gauthier, C., Jacques, P.É., Li, S., and Xia, J. (2021). MetaboAnalyst 5.0: narrowing the gap between raw spectra and functional insights. *Nucleic Acids Res.* 49, W388–W396. <https://doi.org/10.1093/nar/gkaa382>.
70. Gu, Z., Eils, R., and Schlesner, M. (2016). Complex heatmaps reveal patterns and correlations in multidimensional genomic data. *Bioinformatics* 32, 2847–2849. <https://doi.org/10.1093/bioinformatics/btw313>.
71. Tyanova, S., Temu, T., Sinitcyn, P., Carlson, A., Hein, M.Y., Geiger, T., Mann, M., and Cox, J. (2016). The Perseus computational platform for comprehensive analysis of (proteo)omics data. *Nat. Methods* 13, 731–740. <https://doi.org/10.1038/nmeth.3901>.
72. Szklarczyk, D., Kirsch, R., Koutrouli, M., Nastou, K., Mehryary, F., Hachilif, R., Gable, A.L., Fang, T., Doncheva, N.T., Pyysalo, S., et al. (2023). The STRING database in 2023: protein-protein association networks and functional enrichment analyses for any sequenced genome of interest. *Nucleic Acids Res.* 51, D638–D646. <https://doi.org/10.1093/nar/gkac1000>.
73. Katoh, K., and Standley, D.M. (2013). MAFFT multiple sequence alignment software version 7: improvements in performance and usability. *Mol. Biol. Evol.* 30, 772–780. <https://doi.org/10.1093/molbev/mst010>.
74. Minh, B.Q., Schmidt, H.A., Chernomor, O., Schrempf, D., Woodhams, M. D., von Haeseler, A., and Lanfear, R. (2020). Corrigendum to: IQ-TREE 2: New Models and Efficient Methods for Phylogenetic Inference in the Genomic Era. *Mol. Biol. Evol.* 37, 2461. <https://doi.org/10.1093/molbev/msaa131>.
75. Yu, G., Smith, D.K., Zhu, H., Guan, Y., and Lam, T.T.Y. (2017). ggtree: an R package for visualization and annotation of phylogenetic trees with their covariates and other associated data. *Methods Ecol. Evol.* 8, 28–36. <https://doi.org/10.1111/2041-210X.12628>.
76. Irber, L., Pierce-Ward, N.T., Abuelanin, M., Alexander, H., Anant, A., Barve, K., Baumler, C., Botvinnik, O., Brooks, P., Dsouza, D., et al. (2024). sourmash v4: A multitol tool to quickly search, compare, and analyze genomic and metagenomic data sets. *J. Open Source Software* 9, 6830. <https://doi.org/10.21105/joss.06830>.
77. Galardini, M., Koumoutsi, A., Herrera-Dominguez, L., Cordero Varela, J. A., Telzerow, A., Wagih, O., Wartel, M., Clermont, O., Denamur, E., Typas, A., and Beltrao, P. (2017). Phenotype inference in an *Escherichia coli* strain panel. *eLife* 6, e31035. <https://doi.org/10.7554/eLife.31035>.
78. Baba, T., Ara, T., Hasegawa, M., Takai, Y., Okumura, Y., Baba, M., Datsenko, K.A., Tomita, M., Wanner, B.L., and Mori, H. (2006). Construction of *Escherichia coli* K-12 in-frame, single-gene knockout mutants: the Keio collection. *Mol. Syst. Biol.* 2, 2006.0008. <https://doi.org/10.1038/msb4100050>.
79. Kitagawa, M., Ara, T., Arifuzzaman, M., Ioka-Nakamichi, T., Inamoto, E., Toyonaga, H., and Mori, H. (2005). Complete set of ORF clones of *Escherichia coli* ASKA library (a complete set of *E. coli* K-12 ORF archive): unique resources for biological research. *DNA Res.* 12, 291–299. <https://doi.org/10.1093/dnares/dsi012>.
80. Vos, J.L., Elbers, J.B.W., Krijgsman, O., Traets, J.J.H., Qiao, X., van der Leun, A.M., Lubeck, Y., Seignette, I.M., Smit, L.A., Willems, S.M., et al. (2021). Neoadjuvant immunotherapy with nivolumab and ipilimumab induces major pathological responses in patients with head and neck squamous cell carcinoma. *Nat. Commun.* 12, 7348. <https://doi.org/10.1038/s41467-021-26472-9>.
81. Cherepanov, P.P., and Wackernagel, W. (1995). Gene disruption in *Escherichia coli*: TcR and KmR cassettes with the option of Flp-catalyzed excision of the antibiotic-resistance determinant. *Gene* 158, 9–14. [https://doi.org/10.1016/0378-1119\(95\)00193-a](https://doi.org/10.1016/0378-1119(95)00193-a).
82. Thomason, L.C., Costantino, N., and Court, D.L. (2007). *E. coli* genome manipulation by P1 transduction. *Curr. Protoc. Mol. Biol.* 79, 1–17. <https://doi.org/10.1002/0471142727.mb0117s79>.
83. Chung, C.T., Niemela, S.L., and Miller, R.H. (1989). One-step preparation of competent *Escherichia coli*: transformation and storage of bacterial cells in the same solution. *Proc. Natl. Acad. Sci. USA* 86, 2172–2175. <https://doi.org/10.1073/pnas.86.7.2172>.
84. Magnusdottir, S., Heinken, A., Kutt, L., Ravcheev, D.A., Bauer, E., Noronha, A., Greenhalgh, K., Jäger, C., Baginska, J., Wilmes, P., et al. (2017). Generation of genome-scale metabolic reconstructions for 773 members of the human gut microbiota. *Nat. Biotechnol.* 35, 81–89. <https://doi.org/10.1038/nbt.3703>.
85. Aden, K., Rehman, A., Waschyna, S., Pan, W.H., Walker, A., Lucio, M., Nunez, A.M., Bharti, R., Zimmerman, J., Bethge, J., et al. (2019). Metabolic Functions of Gut Microbes Associate With Efficacy of Tumor Necrosis Factor Antagonists in Patients With Inflammatory Bowel

- Diseases. *Gastroenterology* 157, 1279–1292.e11. <https://doi.org/10.1053/j.gastro.2019.07.025>.
86. Altschul, S.F., Gish, W., Miller, W., Myers, E.W., and Lipman, D.J. (1990). Basic local alignment search tool. *J. Mol. Biol.* 215, 403–410. [https://doi.org/10.1016/S0022-2836\(05\)80360-2](https://doi.org/10.1016/S0022-2836(05)80360-2).
 87. Bernardes, J.P., Mishra, N., Tran, F., Bahmer, T., Best, L., Blase, J.I., Bordoni, D., Franzenburg, J., Geisen, U., Josephs-Spaedling, J., et al. (2020). Longitudinal Multi-omics Analyses Identify Responses of Megakaryocytes, Erythroid Cells, and Plasmablasts as Hallmarks of Severe COVID-19. *Immunity* 53, 1296–1314.e9. <https://doi.org/10.1016/j.immuni.2020.11.017>.
 88. McConnell, E.L., Basit, A.W., and Murdan, S. (2008). Measurements of rat and mouse gastrointestinal pH, fluid and lymphoid tissue, and implications for in-vivo experiments. *J. Pharm. Pharmacol.* 60, 63–70. <https://doi.org/10.1211/jpp.60.1.0008>.
 89. Orth, J.D., Thiele, I., and Palsson, B.Ø. (2010). What is flux balance analysis? *Nat. Biotechnol.* 28, 245–248. <https://doi.org/10.1038/nbt.1614>.
 90. Grenier, F., Matteau, D., Baby, V., and Rodrigue, S. (2014). Complete Genome Sequence of Escherichia coli BW25113. *Genome Announc.* 2, e01038-14. <https://doi.org/10.1128/genomeA.01038-14>.
 91. Bornstein, B.J., Keating, S.M., Jouraku, A., and Hucka, M. (2008). LibSBML: an API library for SBML. *Bioinformatics* 24, 880–881. <https://doi.org/10.1093/bioinformatics/btn051>.
 92. Berg, S., Kutra, D., Kroeger, T., Straehle, C.N., Kausler, B.X., Haubold, C., Schiegg, M., Ales, J., Beier, T., Rudy, M., et al. (2019). ilastik: interactive machine learning for (bio)image analysis. *Nat. Methods* 16, 1226–1232. <https://doi.org/10.1038/s41592-019-0582-9>.
 93. Yadav, B., Wennerberg, K., Aittokallio, T., and Tang, J. (2015). Searching for Drug Synergy in Complex Dose-Response Landscapes Using an Interaction Potency Model. *Comput. Struct. Biotechnol. J.* 13, 504–513. <https://doi.org/10.1016/j.csbj.2015.09.001>.
 94. Wishart, D.S., Feunang, Y.D., Guo, A.C., Lo, E.J., Marcu, A., Grant, J.R., Sajed, T., Johnson, D., Li, C., Sayeeda, Z., et al. (2018). DrugBank 5.0: a major update to the DrugBank database for 2018. *Nucleic Acids Res.* 46, D1074–D1082. <https://doi.org/10.1093/nar/gkx1037>.
 95. Kim, S., Chen, J., Cheng, T., Gindulyte, A., He, J., He, S., Li, Q., Shoemaker, B.A., Thiessen, P.A., Yu, B., et al. (2023). PubChem 2023 update. *Nucleic Acids Res.* 51, D1373–D1380. <https://doi.org/10.1093/nar/gkac956>.
 96. Degtyarenko, K., de Matos, P., Ennis, M., Hastings, J., Zbinden, M., McNaught, A., Alcántara, R., Darsow, M., Guedj, M., and Ashburner, M. (2008). ChEBI: a database and ontology for chemical entities of biological interest. *Nucleic Acids Res.* 36, D344–D350. <https://doi.org/10.1093/nar/gkm791>.
 97. Schwaiger, M., Rampler, E., Hermann, G., Miklos, W., Berger, W., and Koellensperger, G. (2017). Anion-Exchange Chromatography Coupled to High-Resolution Mass Spectrometry: A Powerful Tool for Merging Targeted and Non-targeted Metabolomics. *Anal. Chem.* 89, 7667–7674. <https://doi.org/10.1021/acs.analchem.7b01624>.
 98. Nanadikar, M.S., Vergel Leon, A.M., Guo, J., van Belle, G.J., Jatho, A., Philip, E.S., Brandner, A.F., Böckmann, R.A., Shi, R., Zieseniss, A., et al. (2023). IDH3gamma functions as a redox switch regulating mitochondrial energy metabolism and contractility in the heart. *Nat. Commun.* 14, 2123. <https://doi.org/10.1038/s41467-023-37744-x>.
 99. Pak, V.V., Ezeriņa, D., Lyublinskaya, O.G., Pedre, B., Tyurin-Kuzmin, P. A., Mishina, N.M., Thauvin, M., Young, D., Wahni, K., Martínez Gache, S.A., et al. (2020). Ultrasensitive Genetically Encoded Indicator for Hydrogen Peroxide Identifies Roles for the Oxidant in Cell Migration and Mitochondrial Function. *Cell Metab.* 31, 642–653.e6. <https://doi.org/10.1016/j.cmet.2020.02.003>.
 100. Jacobs, L.J.H.C., Hoehne, M.N., and Riemer, J. (2022). Measuring Intracellular H₂O₂ in Intact Human Cells Using the Genetically Encoded Fluorescent Sensor HyPer7. *Bio Protoc.* 12, e4538. <https://doi.org/10.21769/BioProtoc.4538>.
 101. Fricker, M.D. (2016). Quantitative Redox Imaging Software. *Antioxid. Redox Signal.* 24, 752–762. <https://doi.org/10.1089/ars.2015.6390>.
 102. Boons, G.-J., Downham, R., Kim, K.S., Ley, S.V., and Woods, M. (1994). Dispiroketalts in synthesis (part 10): Further reactions of dispiro protected lactate and glycolate enolates. *Tetrahedron* 50, 7157–7176. [https://doi.org/10.1016/S0040-4020\(01\)85241-8](https://doi.org/10.1016/S0040-4020(01)85241-8).

STAR★METHODS

KEY RESOURCES TABLE

REAGENT or RESOURCE	SOURCE	IDENTIFIER
Antibodies		
Thymidylate Synthase (D5B3) XP Rabbit mAb	Cell Signaling Technology	Cat#9045; RRID: AB_2797693
RRM2 (E7Y9J) XP Rabbit mAb	Cell Signaling Technology	Cat#65939; RRID: AB_2895029
Recombinant Anti-Thymidine Kinase 1/TK1 antibody [EPR3194]	Abcam	Cat#ab91651; RRID: AB_2050398
α-Tubulin Antibody	Cell Signaling Technology	Cat#2144S; RRID: AB_2210548
Anti-rabbit IgG, HRP-linked Antibody	Cell Signaling Technology	Cat#7074S; RRID: AB_2099233
Anti-mouse IgG-Peroxidase antibody	Sigma Aldrich	Cat#A0168; RRID: AB_257867
Phospho-Histone H2A.X (Ser139) Antibody	Cell Signaling Technology	Cat#2577; RRID: AB_2118010
53BP1 Antibody	Cell Signaling Technology	Cat#4937; RRID: AB_10694558
Purified Mouse Anti-p21	BD Biosciences	Cat#556430; RRID: AB_396414
p53 (7F5) Rabbit mAb	Cell Signaling Technology	Cat#2527; RRID: AB_10695803
Donkey anti-Mouse IgG (H+L) Highly Cross-Adsorbed Secondary Antibody, Alexa Fluor 488	Thermo Fisher Scientific	Cat#A-21202; RRID: AB_141607
DDB2 Polyclonal antibody	Proteintech	Cat#30173-1-AP; RRID: AB_2935524
c-Myc Monoclonal Antibody (9E10)	Thermo Fisher Scientific	MA1-980, RRID: AB_558470
E2F4 antibody (E3G2G)	Cell Signaling Technology	Cat#40291; RRID: AB_2799174
Thymidylate Synthase (D5B3) XP Rabbit mAb	Cell Signaling Technology	Cat#9045T; RRID: AB_2797693
RRM2 (E7Y9J) XP Rabbit mAb	Cell Signaling Technology	Cat#65939T; RRID: AB_2895029
α-Tubulin Antibody	Cell Signaling Technology	Cat#2144S; RRID: AB_2210548
E.coli RNA Sigma 70 antibody	BioLegend	Cat#663208; RRID: AB_2814499
Recombinant Anti-Thymidine Kinase 1/TK1 antibody	Abcam	Cat#ab91651; RRID: AB_2050398
Anti-CRP mouse mAb	BioLegend	Cat#664304; RRID: AB_2565553
Donkey anti-Rabbit IgG (H+L) Highly Cross-Adsorbed Secondary Antibody, Alexa Fluor 488	Thermo Fisher Scientific	Cat#A-21206; RRID: AB_2535792
Bacterial and virus strains		
<i>E. coli</i> OP50p (uracil prototroph made from OP50 Uracil auxotroph)	CGC	Cat#11077; RRID: WB-STRAIN:OP50
<i>E. coli</i> BW25113: F-, Δ(araD-araB)567, ΔlacZ4787(:rrnB-3), λ- rph-, Δ(rhaD-rhaB) 568, hsdR514	CGSC	CGSC#7636
<i>C. aquatica</i>	CGC	Cat#7905; RRID: WB-STRAIN:DA1877
<i>E. coli</i> HT115: mcrA, mcrB, IN(rrnD, rrnE)1, rnc14::Tn10 λ(DE3)	CGC	Cat#8854; RRID: WB-STRAIN:HT115(DE3)
Additional bacterial mutants used in this study are from the Keio collection and are listed on Table S1	This study	Table S1
Keio collection: Single-gene knockout mutants in <i>E. coli</i> BW25113 background	NBRP	https://shigen.nig.ac.jp/ecoli/strain/resource/keioCollection/list/
ASKA collection: <i>E. coli</i> ORF clones (GFP -)	NBRP	https://shigen.nig.ac.jp/ecoli/strain/resource/askaClone/list/ASKA_CLONE_MINUS
<i>E. coli</i> : BW25113 ΔgltA ΔppsA::Kan	This study	N/A

(Continued on next page)

Continued

REAGENT or RESOURCE	SOURCE	IDENTIFIER
<i>E. coli</i> : BW25113 ΔgltA ΔpoxB::Kan	This study	N/A
<i>E. coli</i> : BW25113 ΔgltA ΔilvC::Kan	This study	N/A
<i>E. coli</i> : BW25113 ΔgltA ΔilvB::Kan	This study	N/A
<i>E. coli</i> : BW25113 ΔgltA ΔilvN::Kan	This study	N/A
<i>E. coli</i> : BW25113 ΔgltA ΔpflB::Kan	This study	N/A
<i>E. coli</i> : BW25113 ΔgltA ΔtdcE::Kan	This study	N/A
<i>E. coli</i> : BW25113 ΔgltA ΔldhA::Kan	This study	N/A
<i>E. coli</i> : BW25113 ΔgltA ΔgarL::Kan	This study	N/A
<i>E. coli</i> : BW25113 ΔgltA ΔprpB::Kan	This study	N/A
<i>E. coli</i> : BW25113 ΔgltA ΔmhpE::Kan	This study	N/A
<i>E. coli</i> : BW25113 ΔgltA ΔpabC::Kan	This study	N/A
<i>E. coli</i> : BW25113 ΔgltA ΔnanA::Kan	This study	N/A
<i>E. coli</i> : BW25113 ΔgltA ΔdgoA::Kan	This study	N/A
<i>E. coli</i> : BW25113 ΔgltA ΔavtA::Kan	This study	N/A
<i>E. coli</i> : BW25113 ΔgltA ΔalaC::Kan	This study	N/A
<i>E. coli</i> : BW25113 ΔgltA ΔalaA::Kan	This study	N/A
<i>E. coli</i> : BW25113 ΔgltA ΔglyA::Kan	This study	N/A
<i>E. coli</i> : BW25113 ΔgltA ΔyagE::Kan	This study	N/A
<i>E. coli</i> : BW25113 ΔgltA Δeda::Kan	This study	N/A
<i>E. coli</i> : BW25113 ΔgltA ΔyjhH::Kan	This study	N/A
<i>E. coli</i> : BW25113 ΔgltA ΔyfaU::Kan	This study	N/A
<i>E. coli</i> : BW25113 ΔgltA ΔydbK::Kan	This study	N/A
<i>E. coli</i> : BW25113 ΔgltA ΔpyrE::Kan	This study	N/A
<i>E. coli</i> : BW25113 ΔgltA Δacs::Kan	This study	N/A
<i>E. coli</i> : BW25113 ΔgltA ΔacnB::Kan	This study	N/A
<i>E. coli</i> : BW25113 ΔgltA ΔprpC::Kan	This study	N/A
<i>E. coli</i> : BW25113 ΔgltA ΔprpD::Kan	This study	N/A
<i>E. coli</i> : BW25113 ΔgltA ΔprpE::Kan	This study	N/A
<i>E. coli</i> : BW25113 ΔpykA ΔpykF::Kan	This study	N/A
<i>E. coli</i> : BW25113 Δudp Δudk Δupp::Kan	Scott et al. ¹⁴	N/A
<i>E. coli</i> : BW25113 pPrpB	This study	N/A
<i>E. coli</i> : BW25113 ΔgltA::Kan pPrpB	This study	N/A
<i>E. coli</i> : BW25113 ΔprpB::Kan pPrpB	This study	N/A
<i>E. coli</i> : BW25113 ΔgltA ΔprpB::Kan pPrpB	This study	N/A
<i>E. coli</i> : BW25113 pAcnB	This study	N/A
<i>E. coli</i> : BW25113 ΔgltA::Kan pAcnB	This study	N/A
<i>E. coli</i> : BW25113 ΔprpB::Kan pAcnB	This study	N/A
Additional bacterial strains from natural isolates and lab strains can be found in Table S1		Table S1

Chemicals, peptides, and recombinant proteins

(2RS,3SR)-2-Methylisocitric acid sodium salt	Sigma-Aldrich	92988-50MG
0.25% Trypsin-EDTA (1X)	Gibco	25200-056
5-Fluorouracil	Sigma-Aldrich	F6627-1G
Ammonium Hydroxide Solution	Sigma-Aldrich	221228-25ML
Biolog Dye mix A	Biolog	Cat#74221
Biolog Phenotype Microarray Panels PM-M11, PM-M12, PM-M13, PM-M14	Biolog	Cat #13111, #13112, #13113, #13114

(Continued on next page)

Continued

REAGENT or RESOURCE	SOURCE	IDENTIFIER
Biolog Phenotype Microarrays PM1, PM2A, PM3B, PM4A	Biolog	Cat#12191
Digitonin	Sigma-Aldrich	D141-100MG
Fetal Bovine Serum	Sigma-Aldrich	F7524 (Lot BCBW1085)
Glycerol 99.5%	Fisher Scientific	BP229-1
HEPES	Sigma-Aldrich	H3375
Isocitric Dehydrogenase (NADP) from porcine heart	Sigma-Aldrich	I2002
LB Broth Miller	Fisher Scientific	Cat#BP1426
Menadione	Cambridge Biosciences	M079
PBS pH 7.4 (1X)	Gibco	10010-015
Penicillin/Streptomycin	Gibco	15140-122
Proteinase K	Sigma-Aldrich	P2308
RPMI	Gibco	A10491-01
Seahorse XF RPMI	Agilent	103576-100
SYBR SAFE gel stain	Thermo Fisher Scientific	S33102
TAE Buffer, Tris-Acetate-EDTA, 50X Solution	Fisher BioReagents	BP1332-4
Urea	Sigma-Aldrich	U5128
XTT Sodium Salt	Sigma-Aldrich	X4626
Propionic acid	Merck	8.00605.0100
Bleach (Sodium hypochlorite, 10-15% active chlorine)	Acros Organics	219255000
Chloramphenicol	Sigma-Aldrich	C0378-5G
Kanamycin Sulfate	Fisher Scientific	BP906-5
D-(+)-Galactose	Sigma-Aldrich	Cat#G0750-10G
D-(+)-Glucose ≥99.5%	Sigma-Aldrich	Cat#G8270
Glycerol ≥99.5%	Thermo Fisher Scientific	Cat#BP229-1
Isopropyl-β-D-thiogalactopyranoside (IPTG) ≥99 %	Thermo Fisher Scientific	Cat#BP1755
Soy peptone	Sigma-Aldrich	Cat#70178
5-Fluorouracil ≥ 99%	Sigma-Aldrich	Cat#F6627
5-Fluoroornotic acid 98%	ThermoFisher Scientific	Cat#R0811
Cytidine-13C9,15N3 5'-triphosphate	Sigma-Aldrich	Cat#645699
Uridine-13C9,15N2 5'-triphosphate	Santa Cruz Biotechnology	Cat#SC-301963A
Chloroform	Honeywell	C2432
Dimethyl Sulfoxide	Sigma-Aldrich	D8418-100ML
Brain heart infusion broth (BHI)	Sigma-Aldrich	53286-500G
13C10-ATP	Sigma-Aldrich	Cat#710695
Citric acid-13C ₆	Sigma-Aldrich	606081-100MG
Trisodium 2-Methylcitrate, racemic mixture of diastereomers (Methyl-D3, 98%) 90% + CP	Cambridge Isotope Laboratories	DLM-10758-PK
TrpLE (Gibco TrypLE Express Enzyme (1x)	Gibco	Cat#11558856
2x Laemmli Sample buffer	BioRad	Cat#1610737
4–20% Criterion TGX Precast Midi Protein	BioRad	Cat#5671093
Precision Plus Protein Dual Color Standards	BioRad	Cat#1610374
Trans-Blot Turbo PVDF Transfer Packs	BioRad	Cat#1704157
Probumin Bovine Serum Albumin Microbiological Grade	Sigma-Aldrich	Cat#810651
Sodium azide	Sigma-Aldrich	S2002-100G
Clarity Western ECL Substrate	BioRad	Cat#1705061

(Continued on next page)

Continued

REAGENT or RESOURCE	SOURCE	IDENTIFIER
Pierce Restore PLUS Western Blot Stripping Buffer	Thermo Fisher Scientific	Cat#46430
Agar for <i>C. elegans</i> culture	Sigma-Aldrich	A7002-5KG
Bacto peptone for <i>C. elegans</i> culture	BD Difco	Cat#211677
NaCl for <i>C. elegans</i> culture	Sigma-Aldrich	S3014-1KG
MgSO ₄ for <i>C. elegans</i> culture	Fisher	M/1050/53
CaCl ₂ for <i>C. elegans</i> culture	Sigma-Aldrich	C3881-1KG
Cholesterol	Sigma-Aldrich	C8667-5G
Agar for <i>Drosophila</i> culture	Fisher Scientific	BP2641-1
Yeast for <i>Drosophila</i> culture	MP Biomedicals	903312
Yeast extract for <i>Drosophila</i> culture	Sigma	70161
Peptone for <i>Drosophila</i> culture	Sigma	82303
Sucrose for <i>Drosophila</i> culture	Fisher Scientific	S/8600/63
Glucose for <i>Drosophila</i> culture	Thermo Scientific	170080025
MgSO ₄ for <i>Drosophila</i> culture	Honeywell Fluka	00627
CaCl ₂ for <i>Drosophila</i> culture	Honeywell Fluka	223506
Propionic acid for <i>Drosophila</i> culture	Sigma	P1386
Nipagin for <i>Drosophila</i> culture (methyl 4-hydroxybenzoate)	Sigma	H5501
Ethanol for <i>Drosophila</i> culture	Fisher Scientific	E/0555DF/17
Columbia Agar	Thermo Scientific	11783513
De Man–Rogosa–Sharpe agar	Millipore	69966
Defibrinated horse blood	Thermo Scientific	SR0050C
Fastidious Anaerobe Agar	Neogen	NCM0199C
Critical commercial assays		
GenElute Mammalian Total RNA Miniprep Kit	Sigma-Aldrich	RTN70
Pierce BCA Protein Assay Kit	Thermo Fisher Scientific	Cat#23227
GenElute Plasmid MiniPrep Kit	Sigma-Aldrich	PLN70
IDH activity assay kit	Abcam	ab102528
MycoAlert testing kit	Lonza	LT07-318
RT-PCR cDNA Supermix	iScript Ready-to-Use cDNA Supermix, ⁵⁶ reaction kit	Cat#1708841
PhosSTOP	Roche	4906845001
eBioscience Annexin V-Apoptosis Detection Kit FITC	Invitrogen	88-8005-72
FxCycle PI/RNAse Staining Solution Kit	Invitrogen	F10797
poly-L-Lysine-coated	Sigma-Aldrich	P4832
Paraformaldehyde	Thermo Fisher Scientific	Cat# 28906
B-Per lysis buffer	Thermo Fisher Scientific	Cat#78243
Mitochondrial Stress Test Kit	Agilent	Cat#103015-100
Click-iT EdU Cell Proliferation Kit for Imaging, Alexa Fluor 647 dye	Thermo Fisher Scientific	C10340
cComplete protease inhibitor cocktail	Sigma-Aldrich	11836170001
Deposited data		
HCT116 cells proteomics	This study	PRIDE: PXD051364
HCT116, LoVo, DLD-1, SW48, HT29, SW1417 and SK-CO-1 cells RNAseq	This study	GEO: GSE263706
HCT116 cells targeted metabolomics	This study	MetaboLights: MTBL9995
HCT116 cells fluoronucleotides measurements	This study	MetaboLights: MTBL9992

(Continued on next page)

Continued

REAGENT or RESOURCE	SOURCE	IDENTIFIER
E. coli and C. elegans fluoronucleotides detection	This study	MetaboLights: MTBLS9991
Producer and non-producer bacteria 2-MiCit detection	This study	MetaboLights: MTBLS9994
Datasets from proteomics, RNA-seq and 4-way screen	This study	https://doi.org/10.5281/zenodo.10973338
French and German cohort	Zeller et al. ³⁸	European Nucleotide Archive project-ID PRJEB6070.
Italian cohort	Thomas et al. ³⁵	European Nucleotide Archive project-ID PRJNA447983
Japanese cohort	Yachida et al. ³⁶	SRA: DRA006684 and DRA008156
Chinese cohort	Yang et al. ³⁷	SRA: PRJNA763023
GitHub original code	This study	https://doi.org/10.5281/zenodo.15655665
Experimental models: Cell lines		
HCT116	ATCC	(ATCC Cat#CCL-247; RRID: CVCL_0291)
DLD-1	ATCC	(ATCC Cat#CCL-221; RRID: CVCL_0248)
HEPG2	ATCC	(ATCC Cat#HB-8065; RRID: CVCL_0027)
HT29	ATCC	(ATCC Cat#HTB-38; RRID: CVCL_0320)
LoVo	ATCC	(ATCC Cat#CCL-229; RRID: CVCL_0399)
SW48	ATCC	(ATCC Cat#CCL-231; RRID: CVCL_0218)
RKO	ATCC	(ATCC Cat#CRL-2577; RRID: CVCL_0504)
SW837	ATCC	(ATCC Cat#CCL-235; RRID: CVCL_1729)
SW948	ATCC	(ATCC Cat#CCL-237; RRID: CVCL_0632)
SW1417	ATCC	(ATCC Cat#CCL-238; RRID: CVCL_1717)
MCF7	ATCC	(ATCC Cat#HTB-22; RRID: CVCL_0031)
Hs 578T	ATCC	(ATCC Cat#HTB-126; RRID: CVCL_0332)
THP1	ATCC	(ATCC Cat#TIB-202 RRID: CVCL_0006)
LS411N	ATCC	(ATCC Cat#CRL-2159; RRID: CVCL_1385)
SK-CO-1	ATCC	(ATCC Cat#HTB-39; RRID: CVCL_0626)
T84	ATCC	(ATCC Cat#CCL-248; RRID: CVCL_0555)
LS123	ATCC	(ATCC Cat#CCL-255; RRID: CVCL_1383)
SW1116	ATCC	(ATCC Cat#CCL-233; RRID: CVCL_0544)
CCD18Co	ATCC	(ATCC Cat#CRL-1459; RRID: CVCL_2379)
CCD33Co	ATCC	(ATCC Cat#CRL-1539; RRID: CVCL_2389)
CCD-112CoN	ATCC	(ATCC Cat#CRL-1541; RRID: CVCL_6382)
CCD841 CoN	ATCC	(ATCC Cat#CRL-1790; RRID: CVCL_2871)
HCT116 p53/-	Johns Hopkins University	MTA: JHU MTA\#A38994
Experimental models: Organisms/strains		
C. elegans: N2 Bristol	CGC	CGC: 10570; RRID: WB-STRAIN: WBStrain00000001
C. elegans: GH636 <i>umps-1(zu456)III</i>	CGC	CGC: 19419; RRID: WB-STRAIN: WBStrain00007858
C. elegans: OK286: <i>pyr-1(cu8)II</i>	CGC	RRID: WB-STRAIN:WBStrain00029948
D. melanogaster: UAS-LacZ	Bloomington	RRID: BDSC_8529
D. melanogaster: UAS-dcr2;byn-GAL4, UAS-GFP,tub-gal80 ^{ts} /TM6B	Bangi et al. ⁴⁰	N/A
D. melanogaster: UAS-rasG12V;UAS-apcRNAi	Bangi et al. ⁴⁰	N/A
Oligonucleotides		
Primer: KanamycinR K1: CAGTCATAGCCGAATAGCCT	Sigma-Aldrich	N/A

(Continued on next page)

Continued

REAGENT or RESOURCE	SOURCE	IDENTIFIER
Primer: KanamycinR K2: CGGTGCCCTGAATGAAGTC	Sigma-Aldrich	N/A
Primer: <i>acnB</i> Forward: CCATCCTAACGATTCAAGCCAC	Sigma-Aldrich	N/A
Primer: <i>acnB</i> Reverse: CCATCCTAACGATTCAAGCCAC	Sigma-Aldrich	N/A
Primer: <i>acs</i> Forward: GCATAACTGCATGTTCTCAAAG	Sigma-Aldrich	N/A
Primer: <i>acs</i> Reverse: CGAATGTAGGCCGGATAAGG	Sigma-Aldrich	N/A
Primer: <i>alaA</i> Forward: CCCCTCTGGCAAATCTTATTCT	Sigma-Aldrich	N/A
Primer: <i>alaA</i> Reverse: GGTTAATGAGTTCAAGCGGG	Sigma-Aldrich	N/A
Primer: <i>alaC</i> Forward: GGTAATTTCTTGTAGCGCAGA	Sigma-Aldrich	N/A
Primer: <i>alaC</i> Reverse: CCGGTGTCAACTCACTGTATCA	Sigma-Aldrich	N/A
Primer: <i>avtA</i> Forward: GTCAGCCCTAACAGCGTTGC	Sigma-Aldrich	N/A
Primer: <i>avtA</i> Reverse: GCTTGTTATGCCAGATGCGG	Sigma-Aldrich	N/A
Primer: <i>dgoA</i> Forward: CCATCAACACGCCATCACCC	Sigma-Aldrich	N/A
Primer: <i>dgoA</i> Reverse: CCAATCAAATAGTCACCCAGCTC	Sigma-Aldrich	N/A
Primer: <i>eda</i> Forward: CGTGTGAATGGACAGACAGG	Sigma-Aldrich	N/A
Primer: <i>eda</i> Reverse: GCAGAGAGTGTGTTGACGC	Sigma-Aldrich	N/A
Primer: <i>garL</i> Forward: GGTGATTGGCTACCTGGTAA	Sigma-Aldrich	N/A
Primer: <i>garL</i> Reverse: CCGTAGACGCTGTTCTGCA	Sigma-Aldrich	N/A
Primer: <i>gltA</i> Forward: GGATCCTTACCTGCAAGCG	Sigma-Aldrich	N/A
Primer: <i>gltA</i> Reverse: GGGGGGTATAGATAGACGTCA	Sigma-Aldrich	N/A
Primer: <i>glyA</i> Forward: GCCTGAAGGTAATCGTTGCG	Sigma-Aldrich	N/A
Primer: <i>glyA</i> Reverse: CAGGCCTACACGGAGATTGC	Sigma-Aldrich	N/A
Primer: <i>ilvB</i> Forward: CCCCAATGACTACTCCATGC	Sigma-Aldrich	N/A
Primer: <i>ilvB</i> Reverse: CCTTCAACGTTAAAGCGCGG	Sigma-Aldrich	N/A
Primer: <i>ilvC</i> Forward: GGACAGCCCTCGATGTTGAC	Sigma-Aldrich	N/A
Primer: <i>ilvC</i> Reverse: CCCAGTTGGATATCACATCATT	Sigma-Aldrich	N/A
Primer: <i>ilvN</i> Forward: GCAGGCCTCATTGCAGGAAATC	Sigma-Aldrich	N/A
Primer: <i>ldhA</i> Forward: GGGTAGTTAATCCTGATTAGC	Sigma-Aldrich	N/A

(Continued on next page)

Continued

REAGENT or RESOURCE	SOURCE	IDENTIFIER
Primer: <i>ldhA</i> Reverse: GGCTACTTCTTCATTGTGGTTC	Sigma-Aldrich	N/A
Primer: <i>mhpE</i> Forward: GGTCTGGCTGGAAGTCGAAG	Sigma-Aldrich	N/A
Primer: <i>nanA</i> Forward: GCATCTAACAGCGTCTCG	Sigma-Aldrich	N/A
Primer: <i>pabC</i> Forward: CCCTTATAAAAGGTCCGTTGC	Sigma-Aldrich	N/A
Primer: <i>pabC</i> Reverse: GCAATTGCTGTCGGCAAGATGG	Sigma-Aldrich	N/A
Primer: <i>pflB</i> Forward: GGTTACCGATCGGCAACATTATC	Sigma-Aldrich	N/A
Primer: <i>pflB</i> Reverse: GGCTACGTCGAGTCTGTTTG	Sigma-Aldrich	N/A
Primer: <i>poxB</i> Forward: CCTTATGCCGATGATATTCCCTT	Sigma-Aldrich	N/A
Primer: <i>poxB</i> Reverse: CCGTAACACGTGCCCCAAC	Sigma-Aldrich	N/A
Primer: <i>ppsA</i> Forward: GGAAATTGTCGAAGAGAGCAGA	Sigma-Aldrich	N/A
Primer: <i>ppsA</i> Reverse: CCCGCAACTACCTCAGGTAAAAT	Sigma-Aldrich	N/A
Primer: <i>prpB</i> Forward: GCAATGAAACGCGGTGAAAC	Sigma-Aldrich	N/A
Primer: <i>prpC</i> Forward: GGTCGGATAAGACGCATAGC	Sigma-Aldrich	N/A
Primer: <i>prpC</i> Reverse: GGTATTGAGAGCTTCAGAC	Sigma-Aldrich	N/A
Primer: <i>prpD</i> Forward: GCGTTGATAAAAGACAAAGCAAGG	Sigma-Aldrich	N/A
Primer: <i>prpE</i> Forward: GCATTCTGGAGGTTCTCTCG	Sigma-Aldrich	N/A
Primer: <i>prpE</i> Reverse: CCGTAGGCATGATAAAACGCG	Sigma-Aldrich	N/A
Primer: <i>pykA</i> Forward: GAAGCGCTGAAGGAATCGC	Sigma-Aldrich	N/A
Primer: <i>pykA</i> Reverse: CGCCTGATGATAAGTICAAGTTGC	Sigma-Aldrich	N/A
Primer: <i>pykF</i> Forward: CGATGTCACCTATCCITAGAGC	Sigma-Aldrich	N/A
Primer: <i>pykF</i> Reverse: GCTTCCATCGGATTATCCTTAG	Sigma-Aldrich	N/A
Primer: <i>pyrE</i> Forward: CATCATTGAAAGTGCAGGGGAC	Sigma-Aldrich	N/A
Primer: <i>pyrE</i> Reverse: GAGAATGCGTGAGGGTGAAG	Sigma-Aldrich	N/A
Primer: <i>tdeC</i> Forward: CGCTCTAACTCCTGTGGTGAG	Sigma-Aldrich	N/A
Primer: <i>udk</i> Forward: GCTATTGCACTGGTATCAGACG	Sigma-Aldrich	N/A
Primer: <i>udk</i> Reverse: CTCGGTACACAGACGCATG	Sigma-Aldrich	N/A
Primer: <i>udp</i> Forward: CAACGCATTGCGTCATGGTG	Sigma-Aldrich	N/A

(Continued on next page)

Continued

REAGENT or RESOURCE	SOURCE	IDENTIFIER
Primer: <i>udp</i> Reverse: GCTGTACAAACGTCCAGTTGG	Sigma-Aldrich	N/A
Primer: <i>upp</i> Forward: GAATTGTGCCAGGGTAAAGG	Sigma-Aldrich	N/A
Primer: <i>upp</i> Reverse: GTCTTCACTCACCCCGATAG	Sigma-Aldrich	N/A
Primer: <i>yagE</i> Forward: CCAGCTTAAATTCCCGCACT	Sigma-Aldrich	N/A
Primer: <i>yagE</i> Reverse: CCAGCTTAAATTCCCGCACT	Sigma-Aldrich	N/A
Primer: <i>ydbK</i> Forward: CCCCGCATTTACTTTTATGG	Sigma-Aldrich	N/A
Primer: <i>ydbK</i> Reverse: GGGTTATATGCCTTATTGTCAC	Sigma-Aldrich	N/A
Primer: <i>yfaU</i> Forward: GGATTACTGACGCTGGCAGC	Sigma-Aldrich	N/A
Primer: <i>yfaU</i> Reverse: CCATTAAAATTGCTTGCACATG	Sigma-Aldrich	N/A
Primer: <i>yihH</i> Forward: GGCGATCCGGTAGTTTATTCAAGG	Sigma-Aldrich	N/A
Primer: <i>yihH</i> Reverse: GGCGGTTGATAAGCATCTCTG	Sigma-Aldrich	N/A
Primer: ASKA plasmid pCA24N: GAGGAGAAATTAACATGAGAGG	Sigma-Aldrich	N/A
Primer: ASKA <i>acnB</i> OE plasmid: CCTATGTCAAAGCAGGCTCCTG	Sigma-Aldrich	N/A
Primer: ASKA <i>prpB</i> OE plasmid: GGCAAACAGGTTGTCGAGC	Sigma-Aldrich	N/A
Primer used for RT-PCR: <i>ndk-1</i> Forward: GTCGGAAAGATCATCGCTC	N/A	N/A
Primer used for RT-PCR: <i>ndk-1</i> Reverse: GTAGTGAACCTCAAGATGGG	N/A	N/A
Primer used for RT-PCR: <i>umps-1</i> Forward: GTTCAAGGCTCTAACCTTCC	N/A	N/A
Primer used for RT-PCR: <i>umps-1</i> Reverse: TTCCACGTACGGTAGACTGG	N/A	N/A
Primer used for RT-PCR: <i>dpyd-1</i> Forward: GCCAAATACTACTAGTCCAACC	N/A	N/A
Primer used for RT-PCR: <i>dpyd-1</i> Reverse: TTCAAGATGAGGAGACTCTCG	N/A	N/A
Primer used for RT-PCR: <i>pyr-1</i> Forward: TTGACCATGAAGGAACCTCAC	N/A	N/A
Primer used for RT-PCR: <i>pyr-1</i> Reverse: GTAGGTATCATTTGTGGAGG	N/A	N/A
Primer used for RT-PCR: <i>upp-1</i> Forward: GATGGAGTCAACTGCTTCG	N/A	N/A
Primer used for RT-PCR: <i>upp-1</i> Reverse: TTGAACCTGATCTCCATCCA	N/A	N/A
Recombinant DNA		
pCA24N	NBRP	RRID: NCBITaxon_146876
pCP20	CGSC	CGSC: 7629
pCS2+MLS-HyPer7	Addgene	RRID: Addgene_136470

(Continued on next page)

Continued

REAGENT or RESOURCE	SOURCE	IDENTIFIER
Software and algorithms		
Xcalibur (v.4.1)	ThermoFisher Scientific	https://thermo.flexnetoperations.com/
R (v.4.3.0)	R Core Team	https://www.r-project.org/
Gen5	Agilent	https://www.agilent.com/en/product/cell-analysis/cell-imaging-microscopy/cell-imaging-microscopy-software/biotek-gen5-software-for-imaging-microscopy-1623226
Python (v.3.10)	Python Core Team	https://www.python.org
GraphPad Prism 9	GraphPad Software	https://www.graphpad.com/scientific-software/prism/
SRA-Toolkit (v.3.0.10)	NIH	https://github.com/ncbi/sra-tools
cutadapt (v.1.12)	Martin ⁵⁷	https://github.com/marcelm/cutadapt
prinseq lite (v.0.20.4)	Schemieder and Edwards ⁵⁸	http://prinseq.sourceforge.net/
Bowtie2 (v.2.2.5)	Langmed and Salzberg ⁵⁹	https://bowtie-bio.sourceforge.net/bowtie2/index.shtml
gapseq (v.1.0)	Zimmermann et al. ⁶⁰	https://github.com/jotech/gapseq/
Sybil (v2.0.4)	Gelius-Dietrich et al. ⁶¹	https://cran.r-project.org/web/packages/sybil/index.html
cplexAPI (v.1.4.0)	IBM	https://github.com/cran/cplexAPI
DescTools (v.0.99.54)	N/A	https://cran.r-project.org/package=DescTools
Rstatix (v. 0.7.2)	R package rstatix	https://rpkgs.datanovia.com/rstatix/index.html
MESS (v.0.5.7)	R package MESS	https://cran.r-project.org/package=MESS
growthrates (v.0.8.4)	Hall et al. ⁶²	https://cran.r-project.org/package=growthrates
SynergyFinder (v.2.0)	Ianevski et al. ⁶³	https://www.bioconductor.org/packages/release/bioc/html/synergyfinder.html
Rtsne (v.0.16)	van der Maaten and Hinton	https://cran.r-project.org/package=Rtsne
RDKit (v.2020.09.1.0)	RDKit	https://www.rdkit.org/
Factoextra (v.1.0.7)	R package factoextra	https://cran.r-project.org/package=factoextra
HiSeq Control Software (v.2.2.58)	Illumina	https://support.illumina.com/sequencing/sequencing_instruments/hiseq_2500/downloads.html
RTA (v.2.11.3)	Illumina	https://support.illumina.com/sequencing/sequencing_instruments/hiseq_2500/downloads.html
bcl2fastq2 (v.2.20.0)	Illumina	https://support.illumina.com/downloads/bcl2fastq-conversion-software-v2-20.html
trimmmomatic (v.0.39)	Bolger et al. ⁶⁴	http://www.usadellab.org/cms/?page=trimmmatic
salmon (v.1.5.0)	Patro et al. ⁶⁵	https://combine-lab.github.io/salmon/
DESeq2 (v.1.30.1)	Love et al. ⁶⁶	https://bioconductor.org/packages/release/bioc/html/DESeq2.html
tidyverse (v.1.3.1)	Wickham et al. ⁶⁷	https://www.tidyverse.org/
DoRothEA (v.1.5.2)	Garcia-Alonso et al. ⁶⁸	https://saezlab.github.io/dorothea/
ashr (v.2.2-47)	R package ashr	https://cran.r-project.org/package=ashr

(Continued on next page)

Continued

REAGENT or RESOURCE	SOURCE	IDENTIFIER
Compound Discoverer software (v.3.2)	ThermoFisher Scientific	https://www.thermofisher.com/uk/en/home/industrial/mass-spectrometry/liquid-chromatography-mass-spectrometry-lc-ms/lc-ms-software/multi-omics-data-analysis/compound-discoverer-software.html
Metaboanalyst (v.5.0)	Pang et al. ⁶⁹	https://www.metaboanalyst.ca/
ComplexHeatmap (v.2.16.0)	Gu et al. ⁷⁰	https://bioconductor.org/packages/release/bioc/html/ComplexHeatmap.html
MaxQuant	Tyanova et al. ⁷¹	https://www.maxquant.org/
String DB API (v.11.5)	Szklarczyk et al. ⁷²	https://version-11-5.string-db.org/
Gel Analyzer (v.23.1.1)	N/A	http://www.gel analyzer.com/?i=1
XFe Assay (v.2.6.1.56)	Agilent	https://www.agilent.com/en/product/cell-analysis/real-time-cell-metabolic-analysis/xfe-software/seahorse-wave-desktop-software-740897
barrnap (v0.9)	Torsten Seemann	https://github.com/tseemann/barnap
mafft (v 7.526)	Katoh and Standley ⁷³	https://mafft.cbrc.jp/
IQ-tree (2.3.6)	Minh et al. ⁷⁴	http://www.iqtree.org
ggtree (v.3.13.10)	Yu et al. ⁷⁵	https://bioconductor.org/packages/release/bioc/html/ggtree.html
cobrar	N/A	https://github.com/Waschina/cobrar
Sourmash (v.4.8.12)	Irber et al. ⁷⁶	https://github.com/sourmash-bio/sourmash
<hr/>		
Other		
ECOREF genome assemblies	Galardini et al. ⁷⁷	https://evocellnet.github.io/ecoref/

EXPERIMENTAL MODEL AND STUDY PARTICIPANT DETAILS
Culturing of bacterial and *C. elegans* strains

E. coli BW25113 (CGSC#7636) was obtained from coli Genetic Stock Center (CGSC). *E. coli* OP50p (RRID: WB-STRAIN:OP50) and *Comamonas aquatica* (RRID: WB-STRAIN:DA1877) were obtained from the Caenorhabditis Genetics Center (CGC). Bacterial mutants were derived from the Keio library⁷⁸ or the ASKA collection⁷⁹ and were obtained from the National BioResource Project. All bacterial strains were stored in a 20% v/v glycerol/LB solution at -80°C. When required, strains were streak diluted onto LB agar plates using a sterile plastic loop and were incubated at 37°C overnight. To grow bacteria in liquid culture, 8 mL of LB was inoculated with a single colony picked off an LB agar plate using a sterile plastic loop. The culture was incubated at 37°C for 16 h with constant shaking at 220 rpm. Bacterial culture media was supplemented with 30 µg/mL chloramphenicol or 50 µg/mL kanamycin where appropriate. Antibiotics were not added to liquid cultures if the bacteria were being grown for use with *C. elegans* to avoid any detrimental effects that might be associated with antibiotic exposure.

N2 (RRID: WB-STRAIN:WBStrain00000001), GH636 *umps-1(zu456)III* (RRID: WB-STRAIN:WBStrain00007858) and OK286 *pyr-1(cu8)II* (WB-STRAIN:WBStrain00029948) *C. elegans* strains were obtained from the CGC. Strains were grown in nematode growth medium (NGM) composed of 50 mM NaCl, 0.25% (w/v) bacto peptone, 1.7% (w/v) agar in dH₂O with the addition of 25 mM KH₂PO₄ (pH 6.0), 1 mM MgSO₄, 1 mM CaCl₂, 5 µg/mL cholesterol (dissolved in 100% ethanol) on a lawn of *E. coli* BW25113 as food. Plates were maintained at 20°C and 10 adult worms were picked every 3 days onto new plates to avoid starvation. A synchronized population at the L1 larval stage was obtained by bleaching gravid adults with sodium hypochlorite solution (7:8 bleach:NaOH 4 M) and keeping the eggs at 20°C overnight in M9 buffer (22 mM KH₂PO₄, 86 mM NaCl, 26 mM Na₂HPO₄, 1 mM MgSO₄).

Human cell lines and spheroids

HCT116 human male colorectal carcinoma cell line was obtained from ATCC (Cat#CCL-247, RRID:CVCL 0291). HCT116 lacking p53 (HCT116 p53^(-/-)) was gifted by Dr Bert Vogelstein (Johns Hopkins University, Baltimore, MD). Cells were cultured in complete media: RPMI (Gibco A10491-01) supplemented with 10% v/v FBS (Sigma-Aldrich F7524, Lot BCBW1085) and 1% penicillin/streptomycin (Gibco) and kept at 37°C with 5% CO₂ in a humidified incubator. Cells were split before reaching 80% confluence to avoid overpopulation, all experiments were performed on passages 4 to 20. Mycoplasma testing was routinely conducted using MycoAlert testing kit (Lonza). Additional cell lines are described in Table S5.

HCT116 spheroids were generated by seeding 100 μ L complete media with 1000 cells into each well of a 96-well U-bottom-shaped plate (CELLSTAR, Greiner Bio-One, 650970), centrifuging at 300 \times g for 5 min, and left for 4 days in a humidified incubator at 37°C with 5% CO₂ to form spheroids.

Drosophila husbandry and genetics

Experimental flies were raised and maintained on Bloomington semi-defined diet: 1% (w/v) agar, 8% (w/v) yeast, 2% (w/v) yeast extract, 2% (w/v) peptone, 3% (w/v) sucrose, 6% (w/v) glucose, 500 mg/L MgSO₄·6H₂O, 500 mg/L CaCl₂·2H₂O, 6 mL/L propionic acid, 10 mL/L of 10% (w/v) nipagin in 95% EtOH. Media was supplemented with 2-MiCit (10 mM final, from a 1 M stock in H₂O) once the food had cooled down to <60°C before dispensing into vials.

Virgin females of genotype *UAS-dcr2;byn-GAL4,UAS-GFP,tub-gal80^{ts}/TM6B*⁴⁰ were crossed to control *UAS-LacZ* (Bloomington, RRID:BDSC 8529) or oncogenic *UAS-ras^{G12V};UAS-apc^{RNai40}* males in small cages. Embryos were collected and seeded at constant density into bottles and developed at 18°C to prevent transgene expression. Synchronized populations of newly eclosed flies were allowed to mate and mature for ~3 days at 18°C, sorted into separate sexes (~25 adults per vial) and aged until day 7 of adulthood at 18°C. Flies were incubated at 29°C to induce hindgut tumors.

Human cohorts

Phenotypic details for the human cohorts are provided in [Table S4](#).

French and German cohort

The cohort data consists of two datasets from biopsy donors from German and French populations with adenoma, adenocarcinoma or healthy controls. The German cohort has only 5 healthy controls which are all male and no patients with adenoma. While the French cohort is much more balanced in the size and variability of metadata of the study subgroups. We removed one adenoma and one adenocarcinoma patient respectively due to strong deviation in the processed metagenomic data (FR.504, FR.026). The data was originally published in Zeller et al.³⁸ and can be accessed from the European Nucleotide Archive via the project-ID PRJEB6070.

Italian cohort

The Italian cohort comprises two patient cohorts collected in Milan (28 controls and 32 adenocarcinoma) and Vercelli (24 controls, 27 adenoma, 29 adenocarcinoma). The first cohort however did include some UC-patients in the control group. Therefore, we focused on the data obtained in Vercelli only. We removed one adenocarcinoma patient due to strong deviation in the processed metagenomic data (VF208). The data was originally published in Thomas et al.³⁵ and can be accessed from the European Nucleotide Archive via the project-ID PRJNA447983.

Japanese cohort

This cohort originated from 606 participants who underwent colonoscopies at the National Cancer Center Hospital in Tokyo. Colonoscopy preparation does require a bowel cleansing diet which, according to the original study authors, does not impact fecal taxonomic composition. This group was divided into healthy participants (247), patients that had more than three adenomas (66), CRC stage 0 with intramucosal carcinomas (72), CRC stage I-II (108), CRC stage III-IV (74), and finally participants that were considered healthy but had a history of colorectal surgery (39). The data was originally published in Yachida et al.³⁶ and the raw sequencing data for this study is available in the DDBJ Sequence Read Archive (DRA) with accession numbers DRA006684 and DRA008156.

Chinese cohort

1071 fecal samples were collected from study participants in Shanghai and Shandong hospitals, divided into 4 classes, young-onset colorectal cancer (<50 years old), old-onset colorectal cancer (>50 yo), young healthy (<50 yo) and elder healthy participants (>50 yo). From each of these groups, 50 samples were randomly selected to perform WGS, partitioning the groups with 50 participants per condition. Clinical metadata was unfortunately not published with this study. For this article we selected the WGS samples. The data was originally published in Yang et al.³⁷ and can be accessed from SRA with the BioProject ID PRJNA763023.

Netherlands cohort

Metagenomic assembled genomes of tumor associated microbiota were obtained from <https://zenodo.org/records/10777510>, which were originally published in Battaglia et al.³¹ For incomplete clinical metadata please find [Table S4](#) ("1-s2.0-S009286742400312X-mmc4.xlsx") from the original publication. Tumor samples were collected from two cohorts: Human HNSCC tumor material (Vos et al.⁸⁰; <https://clinicaltrials.gov/study/NCT03003637>) and Human NSCLC tumor material, Netherlands Cancer Institute).

METHOD DETAILS

Bacterial IC50 assays

Bacteria grown overnight in LB-Miller broth were washed twice in NGM broth, normalized to an OD₆₀₀ of 2 and added to 96-well microtiter plates at a final dilution of 1000-fold in 200 μ L NGM broth containing 2-fold serially diluted drug. Plates were incubated for 16 h

at 37°C, 180 rpm and the absorbance at OD₆₀₀ was measured using a Tecan Infinite Pro M200 microplate reader and Magellan v7.2 software. GraphPad Prism 6 was used to create drug response curves and calculate the concentration of drug required for 50% growth inhibition (IC50) using a log(inhibitor) vs. response - variable slope (four parameter) model and perform statistical analysis of IC50 values by one-way ANOVA.

LC-MS/MS method for nucleotide and fluoronucleotide quantification

Bacterial sample preparation and collection

Bacterial cultures were prepared as described above with 5-FU (50 µM) or Glucose (10 mM) for 4 biological replicates per condition. Cultures were chilled on ice for 5 min before being centrifuged for 10 min at 6400 x g, 4°C. Supernatant was removed except for 500 µL that was used to resuspend the bacterial pellet. Samples were transferred to 2 mL tubes and were centrifuged. The supernatant was completely removed, and tubes were immediately flash frozen in liquid nitrogen. Samples were stored at -80°C until metabolite extraction.

Worm sample preparation and collection

Fifty NGM plates were prepared as described above, seeding them with approximately 1300 synchronized worms in L1 stage. After 48 h and once larvae reached L4 stage, all worms were washed off the plates with sterile M9 and transferred into plates previously prepared with NGM supplemented with or without 5-FU (50 µM) and with or without Glucose (10 mM), and that had been previously seeded with 150 µL of an overnight culture of BW25113 or ΔpyrE strain and incubated for 3 days at 20°C. Independent biological replicates (n=4) were prepared for each condition, 6 NGM plates were prepared for each sample. After transferring L4s to different condition plates, worms were incubated at 25°C for approximately 12 h, after which they were collected using sterile 1X PBS, into 30 mL tubes. After settling, the worm pellets were collected and transferred into a 2 mL tube and the pellet was washed 3 times using 1 mL PBS 1x. After the third wash, the supernatant was completely removed, and tubes were immediately flash frozen in liquid nitrogen. Samples were stored at -80°C until metabolite extraction.

Metabolite extraction

Samples were extracted with 300 µL of extraction solvent (water/methanol, 20:80 v/v) using an ultrasonic water bath (15 min) followed by centrifugation (13,000 x g, 10 min). The supernatant was filtered using filter plates (PTFE 0.45 µm). Quality controls (QCs) were created by pooling equal aliquots of each sample in the batch, to assess technical replicate reproducibility.

Chromatographic analyses were carried out on a Vanquish Flex Binary UHPLC system (Thermo Scientific Inc., USA) coupled to a benchtop hybrid quadrupole-Orbitrap Q Exactive mass spectrometer (Thermo Scientific Inc., Germany). Separation was achieved using a SeQuant ZIC-cHILIC column (Merck Millipore, 100 × 2.1 mm, 3 µm) equipped with a guard column (Merck Millipore, 30 × 2.1 mm, 3 µm), both held at a temperature of 30°C and a flow rate of 0.2 mL/min. Mobile phases were 100 mM aqueous ammonium acetate pH 4.60/acetonitrile (10:90 v/v) (solvent A) and 100 mM aqueous ammonium acetate pH 4.60/acetonitrile/water (10:10:80 v/v) (solvent B). The gradient elution was performed with a 25-47% solvent B gradient over 10 min, held at this condition for 8 min, and returning to 25% B at 20 min. The column was equilibrated for 10 min, yielding a total run time of 30 min. Ionization was performed in the negative ion mode using a heated electrospray ionization source, with the following parameters: spray voltage ± 3.0 KV, heater temperature 330°C, capillary temperature 320°C, S-lens RF level 50, sheath and auxiliary gas flow rate, 35 and 10 units, respectively. The mass accuracy was calibrated prior to sample analysis. Mass spectrometric data were acquired in profile mode using the full scan setting (*m/z* 70 – 700). Automatic gain control (AGC) was set to 1e5 and maximum MS1 injection time at 50 ms. Xcalibur (v.4.1) was used for data acquisition and processing.

Quantitative RT-PCR

The expression of *ndk-1*, *umps-1*, *pyr-1*, *upp-1*, and *dpyd-1* *C. elegans* ribonucleotide genes was determined by qRT-PCR using approximately 1300 L4 worms. N2 hermaphrodites were grown on NGM plates seeded with BW25113 with or without 10 mM Glucose. Worms were washed off the plates using M9 and lysed with TRI Reagent (Zymo Research) and lysing matrix D (MP Bio-medicals). Samples were flash-frozen in liquid nitrogen and stored at -80°C overnight. After a thaw-freeze-thaw cycle, samples were homogenized using ThermoMixer C (Eppendorf) (2000 rpm, 10 min, 4°C). Total RNA was extracted using Direct-zol MiniPrep (Zymo Research) followed by in-column DNase I treatment. RNA was quantified using Qubit RNA HS Assay Kit (Thermo Fisher Scientific) and cDNA was synthesized using iScript Reverse Transcription Supermix (Bio-Rad). Target DNA amplification was monitored on a LightCycler 480 Real-Time PCR system (Roche) using PrecisionPLUS 2x qPCR MasterMix (PrimerDesign) using primers ([key resources table](#)) that had been optimized over a linear range of cDNA concentrations. Relative transcript quantification of target genes was calculated using the ΔCt method and was normalized to averaged mRNA levels of the housekeeping gene *cde-42*. At least 3 independent biological replicates per condition were measured.

Bacterial growth assays

Biolog phenotype microarray (PM) plates PM1 and PM2A containing carbon sources, PM3B containing nitrogen sources and PM4A containing sulphur and phosphorus sources were used in the screen. Liquid NGM (NGM without agar) was used as the base media instead of the Biolog IF-0a media provided in the kit. Liquid NGM ± 100 µM 5-FU was supplemented with 1X tetrazolium dye and was inoculated with an overnight culture of BW25113 at a final OD₆₀₀ of 0.026. Plates were incubated for 24 h at 37°C at 180 rpm, and bacterial growth was measured at 750 nm (via tetrazolium dye precipitation) every 5 min using a Cytaion 5 Hybrid Multi-Mode Reader (Agilent) linked to Biospa 8 automated incubator operated through Gen5 software. Bacterial growth was estimated as the area under the curve (AUC) integral at OD₇₅₀.

C. elegans developmental assay using different media

5-FU or 5-fluoroorotic acid (5-FO) efficacy were tested under different media compositions and bacterial strains. Standard NGM with bacto-peptone was prepared along with 3 variations where the bacto-peptone was replaced with soy peptone, LB or porcine brain heart infusion (BHI). NGM was supplemented with a range of drug concentrations (0, 0.5, 1, 2, 4, 8, 16, 32 and 64 μ M) and pipetted into 96 well plates. Wells were seeded with 5 μ L of an overnight culture of either: the *E. coli* K-12 BW25113, the *E. coli* B OP50-uracil prototroph (OP50p) or the soil proteobacteria *C. aquatica*. Plates were incubated at 20°C for 72 h to allow aerobic bacterial growth. Lastly, worms were added to the wells at the L1 stage and scored for their development stage after 48 h incubation at 25°C.

The scoring system divides the worm development into 4 stages: 1 – majority of larvae failed to develop and was arrested at the L1 or L2 stage; 2 – majority of larvae developed to L3 and L4 stage; 3 – majority of larvae developed to young-adult or adult stage and laid eggs are visible within the lawn (no visible progeny); 4 – majority of larvae developed to adulthood, laid eggs, and viable progeny is observable within the well. Scores were used as a single value for the single treatments, or as a combination of the scores across all the conditions where more than one condition was used.

C. elegans developmental assay using Biolog plates and 4-way screening

The nutrients in the wells of Biolog plates PM1, PM2A, PM3B and PM4A were resuspended in 220 μ L of molten NGM (Nematode Growth Medium) supplemented with a specific concentration of 5-FU in 96-well flat-bottomed microtiter plates. Next, the solidified NGM agar was dried for 30 min in a laminar flow hood, after which 5 μ L of overnight *E. coli* BW25113 culture or mutant bacteria (i.e., Δ pyrE, Δ udp Δ udk Δ upp) was added to each well and plates were again dried in a laminar flow hood for 2 h. Plates were incubated at 20°C for 72 h (inside a humidified plastic box) to allow bacterial lawns to grow. Approximately ten L1 nematodes were added per well and incubated at 25°C for 48 h, and their developmental stage was visually scored under the microscope.

Phylogenetic tree reconstruction

E. coli genome assemblies were downloaded from the Ecoref GitHub repository resources (<https://evocellnet.github.io/ecoref/>).⁷⁷ Species that did not belong to the Ecoref collection were downloaded from NCBI (accession numbers are in the Table S1). 16S sequence genes were extracted from each genome assembly using barrnap (v.0.9). When multiple copies of the 16S were present, the first complete instance was selected and the rest withdrawn. The sequences were aligned with mafft⁷³ (v 7.526) and the phylogenetic tree was calculated with IQ-tree⁷⁴ (2.3.6) using automatic model selection, which resulted in the TIM3+F+R3 selected as the substitution model. The tree was represented with ggtree⁷⁵ (v.3.13.10).

Worm and bacterial scores

Bacterial scores for the phylogenetic tree in Figure 1 were calculated as the sum of the normalized area under the curve of the bacterial growth for each drug concentration used (50, 100 and 200 μ M 5FU). The bacterial growth score can be represented as:

$$\text{Bacterial growth score} = \frac{AUC_{50}}{AUC_0} + \frac{AUC_{100}}{AUC_0} + \frac{AUC_{200}}{AUC_0}$$

Development in the worm was evaluated as the cumulative scores (CS) when more than 2 drug concentrations were used in an experiment. For example, for the Figure 1G where we tested 7 different 5-FU concentrations (0, 1, 2.5, 5, 10, 25, and 50 μ M), the CS was calculated as the sum of the different development scores for each drug concentration. This same method was also applied to other similar data through the article when mentioned.

4-way screening data analysis

For each nutrient on the Biolog plates, worm scores were summarized as their median value. Bacterial growth assay data were processed by log2-transforming the area under the curve (AUC) values, which were normalized to the bacterial growth values observed on NGM base media without additional nutrient sources (negative control). A linear model was fitted to the data and multiple univariate analyses were performed. Significant effects of nutrient supplementation, fluoropyrimidine treatment and their interaction were estimated using post-hoc analysis and Tukey's multiple comparison test. BH multiple comparison adjustment was applied with an FDR threshold of 0.05 for significance.

To assess the impact of the Biolog nutrients on bacterial growth under the two conditions (with and without 5FU treatment), we performed an adjusted growth analysis. This approach enables us to quantify the true influence of nutrients on bacterial growth while accounting for the presence of 5FU. Specifically, we calculated the absolute difference between the normalized observed growth in the presence of 5FU (the treatment condition) and the expected growth that would have occurred under the control condition, considering the effect of 5FU, as estimated using a linear model.

$$\text{Score} = |AUC_T - (AUC_C - adj)|$$

To illustrate the joint effects of normalized bacterial growth and worm phenotype at the treatment levels (5 μ M of 5-FU for BW25113 control and Δ pyrE, and 250 μ M of 5-FU for Δ udp Δ udk Δ upp), we multiplied each bacterial growth score by the worm phenotype score in the ternary plots in Figure 2F. Enrichment analysis was performed by using metabolite information obtained from EcoCyc in December 2021. Worms with a developmental score equal to or greater than 3 were included in the analysis as developed worms. Enrichment analysis was conducted using the hypergeometric test in the R-environment. Statistical differences were captured using T-test. Benjamini-Hochberg (BH) multiple comparison adjustment was applied with an FDR threshold of 0.05 for significance.

Gene-nutrient screen

To construct our screening library, we initially compiled all gene knockouts of *E. coli* from the Keio library that were associated with the bacterial respiration process and upstream pathways. Additionally, we incorporated genes from significant pathways identified in

the study by Scott et al.¹⁴ to improve the sensitivity of the screen in detecting genes relevant to 5-FU metabolism. The complete list of selected genes can be found in [Table S1](#).

Selected genes were transferred from the Keio library onto 96-well LB plates with kanamycin for their storage and were cultured twice in the presence of antibiotics to avoid cross-contamination. Subsequently, the bacterial strains were cultivated on standard LB plates supplemented with glycerol at a concentration of 20% and stored at -80°C for long-term preservation.

Our screening experiment encompassed four distinct conditions: control NGM with and without 10 mM glucose, and NGM containing 5 mM 5-FU with and without 10 mM glucose. Glucose was sterilized through filtration and subsequently added to the molten NGM medium. The maintenance and introduction of both bacteria and nematodes were executed following the procedures detailed in the 4-way screening section of this study. We scored the phenotype of the nematodes as previously described and normalized these values using *E. coli* BW25113 wild-type data as a reference for each condition. To quantify the specific impact of gene knockouts within the context of 5-FU exposure, we subtracted the normalized values in the treatment condition (5-FU) from those in the control condition (NGM), both in the presence and absence of glucose. This calculation enabled us to evaluate the net effect of glucose supplementation on the efficacy of 5-FU for each gene knockout.

The landscape of gene knockout effects ([Figure S3B](#)) was stratified into different sections depending on their biological implications: genes resistant in presence of glucose (upper-left); genes resistant with and without glucose (upper-right); genes resistant without glucose (right); genes sensitive in presence of glucose but resistant in absence of glucose (bottom-right); genes sensitive under both control and glucose (bottom-left); genes sensitive in absence of glucose (bottom) and all genes resistant in presence of glucose (upper). Only genes that had an absolute effect of >0.5 were considered. Genes from each part were taken as a group and an enrichment analysis was performed using the information from the EcoCyc pathway for the *E. coli* K-12 strain. Hypergeometric tests were used to calculate enrichment significance for each group of genes. The Benjamini-Hochberg method was used to control for multiple comparisons with a significance threshold of 0.05 to control the false discovery rate (FDR). Significant pathways were used for the main results.

***E. coli* mutant generation**

Removal of Kanamycin cassette: *E. coli* BW25113 double or triple knockout strains were generated using the Keio collection. To create BW25113 strains with multiple gene knockouts, the kanamycin resistance gene from BW25113 single gene deletion mutants was removed with electroporation by using the temperature-sensitive pCP20 plasmid that encodes Flp recombinase and the gene for chloramphenicol resistance.⁸¹ An overnight culture of the BW25113 single gene deletion mutant was diluted 16-fold in LB and grown at 37°C to mid-log phase (OD₆₀₀ at 0.6–0.8). Cells were made electro-competent by washing with an ice cold, sterile 10% glycerol solution. Cells were washed three times by centrifuging the culture at 4000 g at 4°C, discarding the supernatant and resuspending the pellet in 10 mL of 10% glycerol solution. On the third wash, cells were resuspended in 300 μL of 10% glycerol solution and were transferred to 2 mL tubes chilled on ice. For each transformation, 20–200 ng of plasmid DNA was mixed with 70 μL of electro-competent cell suspension in a chilled 0.1 cm electroporation cuvette. Electroporation was carried out using a Gene Pulser system (Bio-Rad) set at 1.8 V, 25 μF and 200 Ω. 1 mL of SOC solution was immediately added to the cuvette and the cell suspension was transferred to a 2 mL tube. The cells were incubated at 30°C with shaking for 2 h and were harvested by centrifuging for 2 min at 18,000 x g. The pellet was resuspended in 200 μL of LB and was spread on an LB plate supplemented with 30 μg/mL chloramphenicol. The plate was left to grow at 30°C for approximately 40 h.

Cells that had been successfully transformed expressed Flp recombinase that specifically recognizes flippase recognition target (FRT) sites flanking the kanamycin resistance cassette, resulting in its excision via homologous recombination.⁸¹ To confirm, chloramphenicol resistant colonies were screened for kanamycin sensitivity by replica streaking them on a kanamycin LB plate and an LB plate containing no antibiotics and incubating at 30°C overnight. The pCP20 plasmid was removed by streaking kanamycin sensitive colonies onto an LB plate containing no antibiotics and incubating at 37°C overnight. Kanamycin sensitive colonies were screened for chloramphenicol sensitivity to confirm loss of pCP20 by replica streaking onto a chloramphenicol LB plate and an LB plate containing no antibiotics and incubating at 37°C overnight. The resulting colonies were confirmed as single gene deletion mutants by single colony PCR (primers described in [key resources table](#)) and were ready to be used as the recipient strain in the transduction protocol to introduce additional mutations.

Gene deletion mutants: To transfer deletion mutations from the Keio library, P1 bacteriophage-mediated transduction was performed.⁸² An overnight culture of the BW25113 donor strain containing the desired gene deletion was diluted by 100-fold in LB with 0.2% glucose and 5 mM CaCl₂. It was incubated at 37°C for 45 min with shaking. P1 bacteriophage (100 μL) was added and the culture was incubated for a further 3 h at 37°C until fully lysed, at which point 100 μL of chloroform was added to the lysate and cell debris was removed by centrifuging for 10 min at 2000 g and transferring the supernatant to a fresh tube. An aliquot of 1.5 mL of an overnight culture of the recipient strain was centrifuged at maximum speed for 2 min. The supernatant was discarded, and cells were resuspended in 0.75 mL sterile P1 salts solution (10 μM CaCl₂, 5 μM MgSO₄ in LB) and transferred to 2 mL tubes. Varying amounts of donor P1 lysate (100–500 μL) were added to 100 μL of the cell suspension and the phage was left to adsorb to the cells for 30 min at 37°C. A tube containing 100 μL of cells but no P1 lysate was included as a negative control. One mL of LB and 200 μL of 1M sodium citrate was added to tubes before incubating them for 1 h at 37°C with shaking. Cells were harvested by centrifuging for 2 min at 18,000 x g and discarding the supernatant. Cells were resuspended in 100 μL LB and spread onto LB plates supplemented with 50 μg/mL kanamycin and 5 mM sodium citrate required to chelate phage particles. Plates were incubated overnight at 37°C and two rounds of re-streaking single colonies onto kanamycin/sodium citrate plates were performed to ensure removal of residual phage. Successful gene deletion was confirmed by single colony PCR.

Gene overexpression strains: BW25113 gene overexpression strains were created by transforming the strain with plasmids extracted from the ASKA collection.⁷⁹ The plasmid used is pCA24N, a high copy number plasmid that expresses the open-reading frame under the control of an IPTG-inducible promoter (T5 lac). The plasmid also encodes a chloramphenicol resistance cassette. The plasmid carrying the gene of interest was extracted from the W3110 strain using a GenElute Plasmid MiniPrep Kit (Sigma-Aldrich) according to the protocol supplied by the manufacturer and was stored at -20°C until required. The plasmid was introduced into the BW25113 strain via TSS-enhanced chemical transformation.⁸³ An overnight culture of BW25113 was diluted by 16-fold in LB and was grown at 37°C until reaching mid-log phase (OD₆₀₀ 0.6–0.8). Cells were harvested by centrifuging for 15 min at 4000 x g. The supernatant was discarded, and cells were resuspended in 1 mL of chilled TSS broth (10% polyethylene glycol 3350 in LB containing 5% DMSO and 50 mM MgSO₄). In a 2 mL tube, 20–200 ng of plasmid DNA was mixed with 80 µL of chilled TSS buffer (100 mM KCl, 30 mM CaCl₂, 50 mM MgSO₄), 200 µL of cell suspension was added and tubes were left to incubate for 20 min on ice followed by 20 min at room temperature. Next, 1 mL of LB was added, and cells were incubated at 37°C with shaking for 2 h. The cells were harvested by centrifuging for 2 min at 18,000 g and the pellet was resuspended in 200 µL of LB. The cell suspension was spread on an LB plate supplemented with 30 µg/mL chloramphenicol and grown overnight at 37°C. Successful transformation was confirmed via single colony PCR of resulting colonies.

2-MiCit production in bacteria: *E. coli* BW25113, ΔgltA, ΔprpB and ΔgltAΔprpB were analyzed for 2-MiCit production. Bacterial cultures were initiated by inoculating 50 mL of liquid NGM or liquid NGM supplemented with propionic acid (10 mM, pH 6.0) with 500 µL of an overnight culture of one of the four bacterial mutants. Bacteria were incubated at 20°C for 16 h with constant shaking at 180 rpm and four independent biological replicates were prepared for each condition. Cultures were transferred to 50 mL tubes and centrifuged for 20 min at 6400 x g, 4°C. Most of the supernatant was discarded, leaving 500 µL to resuspend the bacterial pellet. Samples were transferred to 2 mL tubes and were centrifuged again (20,000 x g, 15 min, 4°C). The supernatant was completely removed, and tubes were flash frozen in liquid nitrogen and stored at -80°C until metabolite extraction.

Bacteria predicted to be 2-MiCit producers or non-producers (Table S8) were also tested. Bacterial strains were grown under anaerobic conditions (80% N₂, 10% H₂ and 10% CO₂) using a Whitley A35 Workstation (Don Whitley Scientific, UK) on different agar media (1.2% agar) based on their nutrient requirements, including Fastidious Anaerobe agar (FAA; Neogen, US) and Columbia agar supplemented with 5% defibrinated horse blood (Thermo Scientific Oxoid, UK) as well as De Man–Rogosa–Sharpe agar (MRS; Millipore, UK) and Luria–Bertani agar (LB; Merck, UK). A single bacterial colony from each bacterial strain was inoculated in 5 mL of pre-reduced Fastidious Anaerobe broth (FAB; Neogen, US) and was allowed to grow for 24 hours anaerobically as described above. 1 mL of culture was transferred to a 1.5 mL tube and centrifuged at 12,000 x g, 10 min, 4°C. The supernatant was discarded, and the pellet was flash frozen in liquid nitrogen and stored at -80°C until metabolite extraction.

Metabolites from bacterial pellets were extracted by adding 1 mL of ice cold 80% HPLC grade methanol containing 50 ng/mL heavy labelled citric acid 13C and 50 ng/mL labelled methylcitrate as internal standards. Metabolites from bacterial culture supernatants were extracted by adding 200 µL of supernatant to 800 µL HPLC grade methanol containing 50 ng/mL internal standards. Samples were kept on ice and were sonicated in a water bath Sonica Q700 for 2 cycles of 5 min for complete disruption of the bacterial pellet. An aliquot of each sample was collected and pooled to make a quality control sample. Tubes were centrifuged (20,000 x g, 15 min, 4°C), supernatant was collected into a new tube, dried in a SpeedVac (SPD2030, Thermo Fisher) and kept at -80°C until metabolite detection. Pellets were dried for protein concentration measurement by BCA. Dried metabolites were resuspended in 1.5 mL 1% formic acid in water.

Liquid chromatographic analyses were performed on a Vanquish Flex Binary UHPLC system (Thermo Scientific Inc., MA, USA) coupled to a benchtop hybrid quadrupole-Orbitrap Q Exactive mass spectrometer (Thermo Scientific Inc., Bremen, Germany). Chromatographic separation of extracts was achieved using a ThermoFisher Accucore aQ C18 Polar Endcapped column (150 x 2.1 mm) held at a temperature of 40°C and a constant flow rate of 0.300 mL/min. Mobile phases were water with 0.5% formic acid (solvent A) and acetonitrile with 0.5% v/v formic acid (solvent B). The gradient elution started at 10% of solvent B, increasing to 40–90% B at 3.5–4.0 min, kept constant until 4.5 min and returned to the initial condition at 6.5 min. The column was equilibrated yielding a total run time of 10 min. The sample injection volume was 5 µL. Ionization was performed in negative mode using a heated electrospray ionization source, with the following parameters: spray voltage -3.0 KV, heater temperature 330°C, capillary temperature 320°C, S-lens RF level 50, sheath and auxiliary gas flow rate, 48 and 11 units, respectively. The mass accuracy was calibrated prior to sample analysis. Mass spectrometric data were acquired at high-resolution (70,000 at *m/z* 200) in profile mode using a Full MS scan method (*m/z* 70 to 700). Automatic gain control (AGC) was set to 10⁶ and maximum injection time 250 ms.

Xcalibur version 4.1 was used for data acquisition and processing. Extracted Ion Chromatograms (EIC) were used in the data processing. Relative quantification is reported based on the peak area ratio of the analyte and the IS (Citric acid 13C3). Data from the peak area was normalized against the bacterial growth per sample, measured as the OD₆₀₀ at the moment of metabolite extraction. The OD was divided by the minimum OD value to get the bacteria/metabolite factor by which the peak area was normalized. The normalized area values were converted into log2 values for the downstream analyses.

Differences in the metabolite production between conditions were tested using pairwise T-Student tests. BH multiple comparison adjustment was applied with an FDR threshold of 0.05 for significance.

Metabolic models

Processing of metagenomic read data

Metagenomic DNA sequencing reads were downloaded from the European Nucleotide Archive via their respective project-ids. Fastq files were extracted from the read archives via the SRA-Toolkit with the ‘fastq-dump’ script. Raw reads from those fastq-files were adapter trimmed (Illumina TruSeq forward and reverse adapter, as well as Nextera transposase sequence) with cutadapt⁵⁷ (v. 1.12) and quality trimmed to a mean PhredScore ≥ 30 using prinseq lite⁵⁸ (v. 0.20.4). Reads shorter than 35 base pairs were subsequently discarded. To remove host DNA contamination, only reads that did not map against the human reference genome (GRCh38.10, 2017-01-06) via Bowtie2⁵⁹ (v. 2.2.5) were kept for the following steps. The processed metagenomic reads were mapped against 774 bacterial genomes from the AGORA human gut microbiome collection (Magnusdottir et al.⁸⁴, obtained from <https://webdav-r3lab.uni.lu/public/msp/AGORA/genomes> on 2019-08-21). Mapping results from the same biological sample but different input fastq-files were combined into a single BAM-file. The total amount of mapped reads per species as well as the count of the remaining unmapped reads were extracted for each sample using an in-house script. Species abundances were normalized sample-wise and multiplied by the cohort median in order to obtain scaled relative abundances. Only after this step, the unmapped read counts were discarded. Species with zeros across all samples were removed. The relative abundance information was used in a community modelling approach (see next section).

Matching Netherlands tumor metagenomes to AGORA genomes

In order to obtain taxonomic annotation with AGORA human gut microbiome reference genomes for Metagenomic Assembled Genomes (MAGs) of the Netherlands’ tumor cohort, we employed the sourmash software⁷⁶ (version 4.8.12). MAGs were obtained from the Zenodo archive (<https://zenodo.org/records/10777510>) contained in the file “assembled_bins.tar.gz”. The AGORA reference genomes were downloaded from <https://webdav-r3lab.uni.lu/public/msp/AGORA/genomes>. In short, k-mer signatures were generated for both the MAGs and the AGORA reference genomes with k=31 and scaled=1000 via the “sketch dna” command, followed by an indexing step fro the AGORA reference. MAGs were compared to the AGORA database via the “sourmash prefetch” command. Query and reference genomes were matched by their Average Nucleotide Identity (ANI) values, ranging between 88.2 – 99.7 %. For each query MAG the best matching AGORA genome was selected based on maximum ANI value.

Metadata information for the sample donors was extracted from file “Hartwig-assembly-pseq.rda” (obtained from Zenodo) via the phyloseq package in R.

Prediction of methylisocitrate production capacity of microbial communities

To predict methylisocitrate production capacity for each microbial community, we followed a similar approach like previously for the prediction of agmatine production capacity of the microbiota of type 2 diabetic patients and healthy controls.²⁰ Briefly, updated metabolic models from the AGORA collection^{84,85} were combined into a community-level metabolic model with the individual bacterial models present in the microbiome of a participant (abundance cut-off 10–4) as individual compartments that could interact via a common exchange space. Due to a lack of nutritional information for these cohorts, models were constrained to a diet comprising 10% of the diet encoded in the AGORA models (“Western diet”) and 90% of an averaged diet derived from a Kiel-based cohort.²⁰ Individual bacterial models that did not achieve a minimal growth rate of 0.01 on this diet were discarded from the community models to avoid a strong influence of their restricted growth on community growth. A community-level biomass reaction that drains the individual species’ biomass according to their relative abundance was added to account for the composition of the microbiome of each participant. Additionally, coupling constraints were added to maintain intracellular fluxes within admissible ranges according to each species’ growth rate (with parameters c=400, u=0.01). Subsequently, we set the export of methylisocitrate from the community as objective function and used parsimonious flux balance analysis with a coefficient of p=10⁻⁶ (cf. Pryor et al.²⁰) to obtain maximal methylisocitrate production for the gut microbiome of each participant. Wilcoxon analysis was used to analyze the differences of 2-MiCit production between conditions. Likewise, the predicted metabolic fluxes for methylisocitrate production of a participant’s microbiome from community modelling were compared using a Wilcoxon-rank-sum test between disease and control groups.

Prediction of methylisocitrate production capacity for individual bacterial strains

Species information for each tumor-associated microbiome was extracted from the supplementary data from the study from Nejman et al.³² We selected the bacterial species considered as hits with a full denomination (to the species level) that occurred at least in one cancer tissue. The 16S sequences from these species were used to run a Blast⁸⁶ and select the closest bacterial strain relative found in NCBI. Genomes with a complete status or with fewer contigs were prioritized over the rest.

To predict the maximum production of 2-MiCit for each species, we used genome-scale metabolic models of bacterial species of the gut microbiome. We reconstructed the metabolic models of the species of interest, based on their genomes, using gapseq (December 2020).⁶⁰ To elucidate the effect of the nutritional environment on the production of 2-MiCit within cancer cells, we simulated the bacterial community in a blood medium derived from human serum metabolomics.⁸⁷ Further, the environment was considered anoxic and the pH was set to the acidic region.⁸⁸ Since not all the bacterial models were able to import/export 2-MiCit, we adapted them by adding the respective exchange reaction to them, if 2-MiCit was already available as metabolite in the model. To determine maximal 2-MiCit production capacity for each bacterial strain, we subsequently used flux balance analysis with the 2-MiCit export reaction as objective.^{20,89}

The simulations were conducted using the software sybil,⁶¹ cplexAPI, and IBM ILOG CPLEX Optimization Studio in the R-environment.

Species abundances were added per tissue to calculate the potential production of 2-MiCit. To avoid biases, we used the Table S4 from the original article³² to filter out the bacteria that were marked to be contaminants per sample. After correcting the bacteria that

passed the filter, relative frequencies were calculated per tissue and the resultant composition matrix was used to calculate 2-MiCit production per tissue by calculating the dot product with the matrix of 2-MiCit production per bug in the two different media.

Metabolic supplementation of BW25113 model

The complete genome of *Escherichia coli* BW25113⁹⁰ was acquired from the NIH GenBank: CP009273 and was used to reconstruct the respective genome-scale metabolic model. To this end, the software gapseq⁶⁰ was utilized (version: 1.4.0 a0b13801). The model was designed to be able to produce biomass based on a simulated blood serum.⁸⁷ Since the model was constructed to work with the simulation software cobrar (version 0.1.1 2b0becf7), the subsequent analysis was performed using this software and its dependencies (libSBML (v. 5.18.0),⁹¹ glpk (v. 4.65)) in the environment of R (version 4.4.2). The objective of the simulation was the production of 2-MiCit under the effect of supplementation of all possible nutrients of the model in an anoxic, acidic environment, similarly to the previously explained simulations. The result resembled *E. coli* production capacity of this compound when 10 mg of each compound was supplemented respectively.

Cancer cell lines

Cell culture treatments

To prepare 1 M 2-MiCit, 50 mg of 2-MiCit [(2R,3S)/[(2S,3R)-2-Methylisocitric sodium salt, SigmaAldrich] was dissolved into 242.5 µL of sterile water. Unless stated otherwise reference to 2-methylisocitrate (2-MiCit) refers to the racemic mixture of (2R,3S) and (2S,3R) isomers. Experiments using the single enantiomer, i.e. (2R,3S) isomer, are separately identified. To prepare 5-FU, a stock of 275 mM 5-FU was made in 1 M ammonium hydroxide and stored at -80°C. A 1 M solution of ammonium hydroxide was prepared without the drug to be used as vehicle control. For each experiment, a solution of 1 mM 5-FU was prepared by adding 18 µL of the 275 mM stock to 5 mL of RPMI complete solution. This was used to prepare treatments of 0.039 to 10 µM 5-FU.

To assess 5-FU and 2-MiCit interaction, a checkerboard plate map was designed. First, cells were added to wells at a density of 10,000 cells per well. In this case, media already contained 2-MiCit at a final concentration of 0, 1, 5 or 10 mM arranged in rows. A serial dilution of the drug was prepared ranging from 10 µM to 0.039 µM and added to the wells in columns. Control wells contained only vehicle.

Spheroid treatments

Drug treatment was performed on 4-day-old spheroids by removing 50 µL and adding 100 µL media with drug or control solutions that were prepared as described. Imaging was done with the BioTek BioSpa Live Cell Analysis System (Agilent) set to 37°C and 5% CO₂. Bright-field images were taken per spheroid every 8-12 h. To analyze spheroid size as mm², the pixel area was defined with Ilastik, version 1.4, using pixel and object classification workflows.⁹² Only the image data from spheroids of the inner wells were considered, therefore the subsequent data analysis was done from each 12 vehicle or 5-FU-treated spheroids, and 18 2-MiCit or combined 2-MiCit and 5-FU-treated spheroids. The area under the curve (AUC) was calculated with R library DescTools (v. 0.99.54) and significance was tested using a T-test (rstatix, v. 0.7.2). Maximum growth rate was calculated from the spheroid growth by using the R package growthrates⁶² (v.0.8.4) with a window of 5 time points.

Cell proliferation

Cell proliferation in 96 well plates was determined with the IncuCyte Zoom System (Sartorius). Cells were detached from flasks using 0.25% Trypsin-EDTA (Gibco). The resulting suspension was centrifuged at 1200 g for 5 min and resuspended in fresh medium. The number of viable cells was determined, and suspension was adjusted to 2500 cells/mL. Cells were plated at a density of 250 cells/well in 100 µL complete RPMI and kept in incubator for 24 h. The next day, 2-MiCit to a final concentration of 1, 5 or 10 mM was added and plates immediately placed in IncuCyte. Control wells contained the same amount of water (vehicle) as the 10 mM 2-MiCit wells. Each condition was performed in triplicate. Confluence was monitored every 2 h for a duration of up to 10 days without media change. Growth curves generated from 20 cell lines were utilized to assess sensitivity to 2-MiCit.

Confluence calculations

Raw values from IncuCyte were extracted and analyzed in R. Cellular confluence was corrected by the minimum value of each run to allow every case to start at the same point. Average and standard error of the mean of confluence per cell line and 2-MiCit concentration was calculated for each time point. Area under the curve (AUC) of each cell growth was calculated with the R library MESS (v. 0.5.7), and summary stats were calculated both considering the different biological replicates or merging all biological replicates together. When multiple biological replicates were represented as a single graph, the standard error of the mean was used instead of standard deviation. From the AUCs, proliferation of each cell line was calculated as the ratio between each treatment and the control (0 mM 2-MiCit). Multi-univariate stats were calculated using ANOVA test, and the P-values were adjusted for multiple comparisons with Tukey HSD (honestly significant difference). Maximum growth rate was calculated for the case of HCT1116 WT and p53^(-/-) with and without 2-MiCit treatment, and for the case of HCT116 WT treated with the different 2-MiCit versions, from the confluence growth by using the R package growthrates (v.0.8.4). Confluence previous to 20 h was discarded, and a window of 30 was used for the function easyfit.

Drosophila model of colon cancer

Survival assay: To assess survival post-induction at 29°C, flies were treated ±10 mM 2-MiCit and transferred to fresh media every ~3 days, with deaths and censors recorded at this stage. Statistical analysis was performed by Log-Rank test using GraphPad Prism 9 version.

Dissemination assay: Flies were induced at 29°C for 7 days on media ±10 mM 2-MiCit. To assess dissemination,⁴⁰ adults were dissected via the anterior abdomen, with all internal organs removed carefully to not disturb the dorsal cuticle. The total number

of GFP-positive foci disseminated into the abdominal cavity per adult was scored under a fluorescence microscope (Leica M165 FC). Statistical analysis was performed by one-way ANOVA using GraphPad Prism 9 version.

Drug-drug interaction

Cells (10,000/well) were seeded into 96-well plates. To assess 5-FU and 2-MiCit interaction, the checkerboard plate map described earlier was used. Cells were incubated for 24 h before viability assay. Cell viability was determined colorimetrically using XTT reagent [sodium 3'-[1-(phenylaminocarbonyl)3,4-tetrazolium]-bis (4-methoxy6-nitro) benzene sulfonic acid hydrate]. XTT solution (1 mg/mL in serum and antibiotic free RPMI) was prepared fresh for each assay and warmed to 50°C until complete solubilization of the reagent. Menadione to a final concentration of 0.1 mM was added to the solution immediately before adding to wells at a ratio of 25 µL reagent per 100 µL of cell medium. Plates were incubated for 2 h at 37°C in humidified incubator with 5% CO₂ for the reduction of XTT by metabolically viable cells. This reaction forms an orange formazan dye that is water soluble. Absorbance at 540 nm was measured with a SpectraMax microplate reader (Molecular Devices).

Biolog Plates PM-M11 to M14 (92 cytotoxic drugs) were used for testing 2-MiCit interaction with different classes of anti-cancer agents. As per manufacturer instructions, media contained 1% FBS, as serum could interfere with the action of some of the drugs. Each group of 4 plates was resuspended with media containing a suspension of cells at 100,000 cells/ml and one of the following 2-MiCit treatments: Vehicle (water), 1mM, 5mM or 10 mM 2-MiCit. Incubation with 2-MiCit was 48 h and cell viability was determined with XTT.

To assess cell viability, we normalized the AUC values under each drug condition to the negative control, where both 2-MiCit and the query drug were absent (concentration = 0). Subsequently, the normalized values were multiplied by 100 to express viability as a percentage. Viability scores were used to evaluate drug-drug interactions using SynergyFinder 2.0 via their web server.⁶³ The ZIP synergy score⁹³ was calculated for every pair of drugs in the screening. From the analysis, both the synergy score and the most synergistic score were used for subsequent statistical analyses in the R-environment. The 92 drugs from the Biolog PM-11 to PM-14 plates were manually categorized based on their molecule class, the type of anti-cancer effect, the molecular/cellular target, and the biological process they affected. This categorization was accomplished by referencing information from DrugBank,⁹⁴ PubChem,⁹⁵ and chEBI,⁹⁶ and can be accessed in the [Table S5](#). To assess the statistical significance of the nucleotide antimetabolite drugs, the ZIP synergistic scores were compared to the null hypothesis representing the collective performance of all other drugs within the library, using a T-test. This comparison allowed us to draw meaningful conclusions about the interactions and synergies between these specific drug classes.

Chemical space representation of the drug space

To represent the chemical space where the Biolog plates are embedded, we analyzed their molecular fingerprints in the context of a collection of more than 2000 drugs approved by the FDA (data downloaded from DrugBank in April 2019). The molecular fingerprints from each compound were calculated using the RDKit library from Python, extracting all the fragment descriptors (e.g., number of aliphatic carboxylic acids, number of aliphatic hydroxyl groups, etc). This matrix was used to create a representation of the chemical space by calculating a t-SNE of the data using R library Rtsne (v.0.16) with parameters *max iter* = 2000, *perplexity* = 20, *theta* = 0.5 and *dims* = 3. The chemical space was represented using plotly (v.4.10.2). t-SNE 3D coordinates were used to cluster the Biolog PM11-14 drugs with K-means method using factoextra (v.1.0.7) and selecting the optimal number of clusters from the silhouette analysis. The drugs present in each cluster were used to calculate an enrichment of molecule type using hypergeometric tests. Benjamini-Hochberg multiple comparison adjustment was applied with an FDR threshold of 0.05 for significance.

RNA sequencing and analysis

DLD-1, HCT116, HT29, LoVo, SK-CO-1, SW1417, and SW948 cells were plated in 6 wells plates with complete medium and the following cell densities: 80,000, 60,000, 150,000, 80,000, 150,000, 200,000 and 120,000 cells/well, respectively. 10 mM of 2-MiCit was used as a treatment, or vehicle (water) for control condition. The treatments were added two days after seeding, and cells incubated for 24 h until the RNA extraction. Samples were prepared using GenElute Mammalian Total RNA Miniprep Kit (Sigma-Aldrich), including on-column DNase I digestion.

Samples were sequenced in two batches: HCT116, DLD-1, LoVo and SW948 on an Illumina NextSeq (75 bp length), and HT29, SK-CO-1, and SW1417 on an Illumina NovaSeq 6000 (100 bp length) machine selecting for polyA mRNA, and raw samples were processed with HiSeq Control Software (v. 2.2.58), RTA (v. 2.11.3) and bcl2fastq2 (v. 2.20.0). Raw sequences were quality filtered and trimmed with trimmomatic⁶⁴ (v.0.39) removing Illumina (first batch) or Nextera (second batch) adapters with parameters to filter 15 leading and trailing bases, and a sliding window of quality 20 for 4 subsequent nucleotides. Sequences from the first batch ranged from 15.7 to 22.3 million reads per paired end sample, with an average of 17.7 ± 1.36 million reads. Sequences from the second batch ranged from 62 to 97.5 million reads per paired sample, with an average of 78.5 ± 9.5 million reads. The resulting reads were mapped to the human reference transcriptome from ensembl database (GRCh38.p13, version 103, GenBank: GCA_000001405.28). Quantification of samples was made via salmon⁶⁵ (v 1.5.0) with mapping validation and gcbias options activated. Subsequent analyses were done in the R-environment with the DESeq2 package⁶⁶ (v. 1.30.1) and tidyverse (1.3.1). Transcripts were matched with their read version via AnnotationHub (v. 2.22.1) and passed to DESeq2 pipeline. Genes that had zero counts for 80% of the samples per cell line were removed to avoid artifacts. Differential gene expression was calculated for each cell line via the ashR method (v. 2.2-47). Enrichment per cell line was calculated by extracting the differentially expressed genes and further analyzed by StringDB.⁷²

PCA was computed with the pca function from DESeq2 package and represented with ggplot (v. 3.4.0). The transcriptional profile for all conditions and cell lines was analyzed in DoRothEA (v. 1.5.2),⁶⁸ only levels A, B and C with high confidence were used for the analysis. Comparisons between conditions were made with T-test and the Benjamini-Hochberg method was used to correct for multiple comparisons with and FDR threshold of 0.05.

Metabolomic analysis

Levels of (fluoro)nucleotides, organic acids and sugar phosphates in *C. elegans* and HCT 116 cells were determined by Anion-Exchange Chromatography coupled to Electrospray Ionization High-Resolution Mass Spectrometry (IC-ESI-HRMS) using previously described procedure^{97,98} with some modifications: approximately 3 million cells or 2,000 worms were suspended in ice-cold methanol/acetonitrile/water 5:3:2 (v/v/v) (300 μ L/10⁶ cells, 500 μ L/2,000 worms) using the Precellys 24 homogenizer (Peqlab) at 6,400 rpm twice for 10 s with a 5-sec pause. To 300 μ L of homogenate, 25 μ L of a mixture of isotope-labeled internal standards in Milli-Q water (50 μ M adenosine-¹³C₁₀ 5'-triphosphate, ¹³C₁₀-ATP, Sigma-Aldrich; 50 μ M ¹³C₆-D-glucose-6-phosphate (¹³C₆-G6P) and 50 μ M D₄-succinic acid (D₄-SUC), both Eurisotop) were added. The samples were extracted using a pre-cooled ThermoMixer (Eppendorf) at 4°C and 900 rpm for 20 min. After centrifugation (16,100 RCF, 20 min, 4°C), the supernatants were dried under a stream of nitrogen, and the residues were resolved in 100 μ L of Milli-Q water. For *C. elegans*, the pellets were used for a protein assay with bicinchoninic acid. After mixing and centrifugation (16,100 RCF, 20 min, 4°C), 80 μ L of the resolved supernatants were transferred to autoinjector vials and immediately measured.

IC-HRMS analysis was performed using a Dionex Integron RFIC system (Thermo Scientific) equipped with a Dionex IonPac AS11-HC column (2 mm x 250 mm, 4 μ m particle size, Thermo Scientific) and a Dionex IonPac AG11-HC guard column (2 mm x 50 mm, 4 μ m, Thermo Scientific) and coupled to a Q Exactive HF quadrupole-orbitrap mass spectrometer (Thermo Scientific). 5 μ L of sample were injected using a Dionex AS-AP at 10°C. The IC was operated at a flow rate of 0.38 mL/min with a potassium hydroxide gradient which was produced by an eluent generator with a potassium hydroxide cartridge and Milli-Q water. The gradient started with 10 mM KOH over 3 min, 10-50 mM from 3 to 12 min, 50-100 mM from 12 to 19 min, held at 100 mM from 19 to 25 min, and re-equilibrated at 10 mM for 3 min. The total run time was 28 min. An Dionex ADRS 600, 2 mm suppressor was operated with 95 mA, and methanol was used to produce a make-up flow at a flow rate of 0.15 mL/min.

The mass spectrometer was operated in the negative ion mode. Full MS scans in the range of *m/z* 60-900 were acquired with a resolution of 120,000, an Automatic Gain Control (AGC) target value of 1×10^6 and a maximum injection time (IT) of 240 ms. Spectrum data were collected in the centroid mode.

The ESI source was operated with flow rates for sheath gas, auxiliary gas, and sweep gas of 50, 14 and 3, respectively. The spray voltage setting was 2.75 kV, the capillary temperature 230°C, the S-lens RF level 45, and the auxiliary gas heater temperature 380°C.^{97,98}

The exact *m/z* traces of the internal standards and endogenous metabolites were extracted and integrated using TraceFinder 5.1 (Thermo Scientific). Endogenous (fluoro)nucleotides were quantified by normalizing their peak areas to those of the internal standards: ¹³C₁₀-ATP was used for (fluoro)nucleotides, ¹³C₆-G6P for sugar phosphates and D₄-SUC for organic acids. For *C. elegans*, the peak area ratios were normalized to the protein content of the sample.

Bacterial sample preparation for fully quantitative and comparative metabolomics

E. coli cultures were initiated by inoculating 8 mL of liquid LB supplemented with kanamycin with single colonies. For the comparative analysis between anaerobic and aerobic conditions, three independent colonies were selected for each treatment and grown entirely under their respective oxygen atmospheres. Final cultures were prepared by inoculating 50 mL of liquid LB (with or without 20 mM propionic acid, pH 6.0) with 500 μ L of an overnight culture. Cultures were incubated at 37°C for 16 h with constant shaking at 180 rpm. To determine colony forming units (CFU), serial dilutions were plated onto LB agar plates containing appropriate selection markers.

One mL of each culture was transferred to 2 mL tubes and centrifuged for 20 min at 6400 \times g at 4°C. Seven hundred μ L of the supernatant was then transferred to a new tube and centrifuged again at 20,000 \times g for 20 min at 4°C. The pelleted bacterial cells were flash frozen after any residual supernatant was removed. For secreted metabolites, the supernatant samples were filtered through a 0.22 μ m strainer and flash frozen in liquid nitrogen prior to extraction.

For metabolite extraction, an extraction solution was prepared consisting of a 50:30:20 mixture (v/v) of acetonitrile, methanol, and water containing the internal standard (valine-d8). For the bacterial pellets, 500 μ L of the extraction solution was added. Samples were vortexed for 2 min, then sonicated in a water bath (Sonica Q700) for 10 min using 20 cycles of 30 s on/off at 100% amplitude at 4 °C. After sonication, the extracts were centrifuged at 20,000 \times g for 30 min at 4°C. For the comparative analysis, 200 μ L of the resulting supernatant was transferred to HPLC vials and stored at -80 °C until further measurement.

For full quantification, 300 μ L of the supernatant was divided into six equal aliquots, to which pre-defined concentrations of 2-MiCit (0, 1, 5, 10, 50, and 100 μ M) were added for standard addition quantification. In parallel, secreted metabolite extracts intended for full quantification were first centrifuged for 5 min at 20,000 \times g (4°C). Then, 50 μ L of the supernatant was mixed with 350 μ L of the extraction solution. The mixture was agitated in a Thermomixer at 1600 rpm for 15 min at 4 °C, followed by centrifugation at 20,000 \times g for 20 min at 4 °C. The top 80% of the supernatant was carefully collected, split into equal portions, and spiked with the pre-defined concentrations of 2-MiCit as described. All samples were then transferred to HPLC vials and stored at -80°C until measurement.

Chromatographic separation of 2-MiCit was performed using a Millipore Sequant ZIC-pHILIC analytical column (5 μ m, 2.1 \times 150 mm) equipped with a 2.1 \times 20 mm guard column (5 μ m particle size) in a binary solvent system. Solvent A was

composed of 20 mM ammonium carbonate with 0.05% ammonium hydroxide, and Solvent B was acetonitrile. The column oven was maintained at 40 °C and the autosampler tray at 4 °C. The gradient was run at a flow rate of 0.200 mL/min as follows: 80% B for the first 2 min; a linear decrease to 20% B over the next 15 min; a rapid linear increase back to 80% B over 0.1 min; and a final hold at 80% B until 23 min. Samples were injected in a randomized order with a 5 µL injection volume. A pooled quality control (QC) sample, prepared from an equal mixture of all individual samples, was analyzed at regular intervals to ensure system consistency.

Detection and quantification of 2-MiCit were performed using a Vanquish Horizon UHPLC system coupled to an Orbitrap Exploris 240 mass spectrometer (Thermo Fisher Scientific) via a heated electrospray ionization source. The Orbitrap was operated at a resolution of 60,000. The spray voltage was set to -2.8 kV, with an RF lens value of 70, a heated capillary temperature of 320 °C, and an auxiliary gas heater temperature of 280 °C. Flow rates for sheath gas, auxiliary gas, and sweep gas were maintained at 40, 15, and 0, respectively. Detection was conducted in negative selected ion monitoring (SIM) mode with a target m/z of 205.0354, using a standard AGC target and an automatic maximum injection time configuration. Chromatogram review and peak area integration were performed using Tracefinder software (v5.1, Thermo Fisher Scientific). All solvents used throughout this study were LC-MS grade from LiChrosolv (Merck KGaA, Darmstadt, Germany). All other reagents and chemicals were of analytical grade unless otherwise specified.

Comprehensive targeted metabolomic analysis/LC-MS in cells

Metabolites were extracted from HCT116 cells (wild type or p53^(-/-)) exposed to 10 mM 2-MiCit for 24 h. Cells were detached from 60 mm plates using trypsin, washed with 5% mannitol in water and resuspended in 100% methanol. Metabolites were extracted through centrifugation (9,100 × g, 4°C, 2 h) using filter units.

Chromatographic separation of metabolites was achieved using a Millipore Sequent ZIC-pHILIC analytical column (5 µm, 2.1 × 150-mm) equipped with a 2.1 × 20 mm guard column (both 5 mm particle size) with a binary solvent system. Solvent A was 20 mM ammonium carbonate, 0.05% w/v ammonium hydroxide; Solvent B was acetonitrile. The column oven and autosampler tray were held at 40°C and 4°C, respectively. The chromatographic gradient was run at a flow rate of 0.200 mL/min as follows: 0–2 min: 80% B; 2–17 min: linear gradient from 80% B to 20% B; 17–17.1 min: linear gradient from 20% B to 80% B; 17.1–23 min: hold at 80% B. Samples were randomized and the injection volume was 5 µL. A pooled quality control (QC) sample was generated from an equal mixture of all individual samples and analyzed interspersed at regular intervals.

Metabolites were measured with Vanquish Horizon UHPLC coupled to an Orbitrap Exploris 240 mass spectrometer (both Thermo Fisher Scientific) via a heated electrospray ionization source. The spray voltages were set to +3.5kV/-2.8 kV, RF lens value at 70, the heated capillary held at 320°C, and the auxiliary gas heater held at 280°C. The flow rate for sheath gas, aux gas and sweep gas were set to 40, 15 and 0, respectively. For MS1 scans, mass range was set to *m/z*=70–900, AGC target set to standard and maximum injection time (IT) set to auto. Data acquisition for experimental samples used full scan mode with polarity switching at an Orbitrap resolution of 120000. Data acquisition for untargeted metabolite identification was performed using the AcquireX Deep Scan workflow, an iterative data-dependent acquisition (DDA) strategy using multiple injections of the pooled sample. DDA full scan-ddMS2 method for AcquireX workflow used the following parameters: full scan resolution was set to 60000, fragmentation resolution to 30000, fragmentation intensity threshold to 5.0.³ Dynamic exclusion was enabled after 1 time and exclusion duration was 10s. Mass tolerance was set to 5ppm. Isolation window was set to 1.2 *m/z*. Normalized HCD collision energies were set to stepped mode with values at 30, 50, 150. Fragmentation scan range was set to auto, AGC target at standard and max IT at auto. Mild trapping was enabled.

Metabolite identification was performed in the Compound Discoverer software (v 3.2, Thermo Fisher Scientific). Metabolite identities were confirmed using the following parameters: (1) precursor ion *m/z* was matched within 5 ppm of theoretical mass predicted by the chemical formula; (2) fragment ions were matched within 5 ppm to an in-house spectral library of authentic compound standards analyzed with the same ddMS2 method with a best match score of over 70; (3) the retention time of metabolites was within 5% of the retention time of a purified standard run with the same chromatographic method.

Chromatogram review and peak area integration were performed using the Tracefinder software (v 5.0, Thermo Fisher Scientific) and the peak area for each detected metabolite was normalized against the total ion count (TIC) of that sample to correct any variations introduced from sample handling to instrument analysis. The normalized areas were used as variables for further statistical data analysis.

For ¹³C- and ¹⁵N-isotope tracing analysis, the theoretical masses of isotopes were calculated and added to a library of predicted isotopes. These masses were searched with a 5 ppm tolerance and integrated only if the peak apex showed less than 1% difference in retention time from the [*U*-¹²C] monoisotopic mass in the same chromatogram. After analysis of the raw data, natural isotope abundances were corrected using the AccuCor algorithm found in <https://github.com/lparsons/accucor>.

Normalized ion intensity data was incorporated into R for further statistical analysis. Values were log2-transformed and multiple univariate tests (T-tests) were performed pairwise between conditions. Benjamini-Hochberg (BH) multiple comparison adjustment was applied with an FDR threshold of 0.05 for significance. Metaboanalyst 5.0⁶⁹ was used to calculate pathway enrichment from the significant metabolites in each condition test. Multiple comparison correction was applied by Benjamini-Hochberg correction using an FDR threshold of 0.05 for the enrichment analysis. Z-scores per metabolite and samples was calculated on the log2 transformed values and represented as heatmaps using ComplexHeatmap in R (v. 2.16.0).⁷⁰

Proteomics analysis in HCT116 cells

HCT116 cells were split at a 1:20 ratio into 60 mm plates and allowed to grow for 48 h in complete medium. After 48 h, media was replaced with fresh medium containing treatments: 1.25 μ M 5-FU and/or 1 or 10 mM 2-MiCit. Results of the 1 mM 2-MiCit groups are not shown, but were included in data analysis. Cells were exposed to 2-MiCit and/or 5-FU for 24 h and analyzed for their protein expression. Plates were washed twice with ice cold PBS and cells were collected into 1.5 mL tubes by scrapping the plates with 500 μ L PBS. Remaining cells were collected by tilting and washing the plate with additional 500 μ L PBS.

Cells were centrifuged at 1000 $\times g$ for 5 min at 4°C, supernatant was discarded and pellets were frozen in liquid nitrogen and kept at -80°C overnight until protein extraction. Each pellet was lysed in protein extraction buffer containing 8 M Urea in 20 mM HEPES, pH 8.0. Tubes were placed in a Diagenode Bioruptor Plus for 20 cycles of sonication at 30s on, 30 s off to remove chromatin. Tubes were spun at max speed for 15 min at 4°C and the supernatant was transferred to a new tube. An aliquot was taken for protein analysis by Bradford and volume was adjusted so that each tube contained 50 μ g protein.

Sample processing

Lysates containing 50 μ g of protein in extraction buffer were reduced and alkylated sequentially with 10 mM dithiothreitol and 50 mM 2-chloroacetamide. Incubation times were 30 min in the dark for each step. Samples were diluted with 20 mM HEPES buffer (pH 8.0) to 4 M urea and 200 ng of LysC (Wako, 125-05061) was added for a final protease to protein ratio of 1:250. Samples were incubated for 5 h at 37°C, followed by a further dilution to 2 M urea and addition of 1 μ g of trypsin (Serva, PN:37286.01) for a final 1:50 ratio. Samples were again incubated overnight at 37°C. Samples were acidified with 0.1% v/v trifluoroacetic acid (TFA). Samples were desalting using Glygen C18 spin tips (Glygen Corp, TT2C18.96). Spin tips were sequentially, solvated and equilibrated 3 times with 60% ACN + 0.1% v/v formic acid (FA) and 1% v/v ACN + 0.1% v/v FA, respectively. Digests were loaded onto spin-tips and de-salted 3 times with 1% ACN + 0.1% v/v FA. Peptides were eluted with 3 sequential volumes of 60% ACN + 0.1% v/v FA using 50 μ L buffer. Eluents were dried using a centrifugal vacuum drier.

Liquid chromatography-tandem mass spectrometry (LC-MS/MS) analysis

Dried peptides were re-dissolved with 0.1% v/v TFA by shaking (1200 rpm) for 30 min followed by sonication on an ultrasonic water bath for 10 min (two 5 min steps with sweep function). Solutions were pre-cleared by centrifugation 18,000 g for 10 min. PROCAL peptides in 0.1% v/v TFA (JPT, PN: RTK-1) were spiked into each sample, with final peptide and PROCAL concentrations of 200 ng/ μ L and 14.3 fmol/ μ L respectively. Additionally, a pool of samples was generated by combining a small equal volume of each sample into 1 vial. LC-MS/MS analysis was carried out in single replicate injections, with 1.4 μ g and 100 fm on column for sample and PROCAL peptides respectively. Pool was injected in technical replicates from beginning to end of sample running list at regular intervals. Chromatographic separation was performed using an Ultimate 3000 RSLC nano-liquid chromatography system (Dionex) coupled to an Orbitrap Q-Exactive HF mass spectrometer (Thermo Scientific) via an EASY-Spray source. For LC-MS/MS analysis peptide solutions were injected and loaded onto a trap column (Acclaim PepMap 100 C18, 100 μ m \times 2 cm) for desalting and concentration at 8 μ L/min in 2% acetonitrile, 0.1% TFA. Peptides were eluted on-line to an analytical column (EASY-Spray PepMap RSLC C18, 75 μ m \times 50 cm) at a flow rate of 250 nL/min. Peptides were separated using a 120-min gradient, 1–22% of buffer B for 90 min followed by 22–42% buffer B for another 30 min (buffer A – 95% H₂O, 5% v/v DMSO, 0.1% FA, buffer B – 75% acetonitrile, 5% v/v DMSO, 20% H₂O, 0.1% FA) and subsequent column conditioning and equilibration. Eluted peptides were analyzed by the mass spectrometer operating in positive polarity using a data-dependent acquisition mode. Ions for fragmentation were determined from an initial MS1 survey scan at 120,000 resolution, followed by HCD (Higher-energy Collision Induced Dissociation) of the top 30 most abundant ions at a resolution of 15,000. MS1 and MS2 scan AGC targets were set to 3e6 and 5e4 for maximum injection times of 25 ms and 50 ms respectively. A survey scan *m/z* range of 350 – 1750 was used, normalized collision energy set to 27% and charge exclusion enabled for unassigned and +1 ions. Dynamic exclusion was set to 50 s.

Data processing

Data were processed using the MaxQuant software platform,⁷¹ with database searches carried out by the in-built Andromeda search engine against the Swissprot *Human* database (version 20200914, number of entries: 20,388). A reverse decoy database approach was used at a 1% false discovery rate (FDR) for peptide spectrum matches and protein identification. Search parameters included: maximum missed cleavages set to 3, fixed modification of cysteine carbamidomethylation and variable modifications of methionine oxidation, protein N-terminal acetylation, carbamylation of lysine and arginine, glutamine cyclisation to pyro-glutamate. Label-free quantification was enabled with an LFQ minimum ratio count of 1. ‘Match between runs’ function was used with match and alignment time limits of 0.7 and 20 min respectively. Only samples where at least 1 protein per condition was present were analyzed. Protein abundance estimates were log₂ transformed. Proteins were annotated with GO terms for Molecular Functions, Cellular Component, and Biological Process, and for KEGG pathways. Two-sample T-test was used to evaluate significant differences in protein levels in Perseus,⁷¹ using the S0 parameter with a value of 0.1, 250 randomizations, and applying BH method with an FDR of 0.05 to correct for multiple comparisons. Heatmap representations were done by computing the Z-scores per protein mean. KEGG pathway and GO terms enrichment was performed by using the String DB⁷² API (v. 11.5). Radar plots were created by averaging all the log2FC values between the treatment vs control comparisons per condition for the selected pathways. The gray area marks the threshold for 0 FC. Multiple comparison correction was done by Benjamini-Hochberg method and using an FDR of 0.05 as significance threshold.

Western blot

HCT116 cells were seeded in 12 well plates at 100,000 cells/well in complete media and treated the next day. After 24 h treatment proteins were extracted. Cells were washed once with cold PBS and lysed by adding 50 µL complete RIPA buffer/well, containing 25x cComplete protease inhibitor cocktail (PIC; Sigma-Aldrich, 11836170001) and 10x PhosSTOP (Roche, 4906845001). The cells were scraped off immediately and transferred to pre-cooled 1.5 mL tubes.

HCT116 Spheroids were generated and treated with drugs for 24 h, as described. For protein extraction, 12 or 24 spheroids were pooled per condition, washed twice with ice-cold PBS, and lysed in 25 µL or 35 µL complete RIPA buffer with repeated cycles of vortexing and spinning down. Both 2D and 3D samples were sonicated in a water bath Sonica Q700 for 2 min with 30 s on/off at 80% amplitude.

BW25113 wildtype and crp-mutant *E. coli* were seeded onto NGM agar plates containing 5 µM 5-FU and/or 10 mM D-glucose as a lawn and incubated at 20°C for 72 h. Bacterial cells were scraped from plates and flash frozen. Per sample, 150 µL complete lysis buffer [B-Per (Thermo Scientific, 78243) reagent and 25x PIC was added and the samples were lysed in a pre-cooled ThermoMixer (Eppendorf) for 10 min at 4°C, 600 rpm. The bacterial samples were sonicated in a water bath Sonica Q700 for 20 cycles à 10 min with 30 s on/off at 80% amplitude. After centrifuging for 30 min at 15,000 rfc, 100 µL of the supernatant was transferred to pre-cooled 1.5 mL tubes.

The protein quantity was determined with the Pierce BCA Protein Assay Kit and samples were prepared with 2x Laemmli Sample buffer (BioRad) and DTT to load 20 µg protein lysate for 2D and 3D human cells and 40 µg for bacterial samples per lane. The prepared samples were loaded onto a 4–20% Criterion TGX Precast Midi Protein Gel (Bio-Rad), accompanied by Precision Plus Protein Dual Color Standards (Bio-Rad). Electrophoresis was conducted at 130 V for 1 h 20 min, ensuring efficient separation of proteins, followed by transfer onto PVDF membranes using Trans-Blot Turbo PVDF Transfer Packs (Bio-Rad, 1704157) for spheroids, and nitrocellulose membranes using Trans-Blot Turbo Midi 0.2 µm Nitrocellulose (Bio-Rad, 1707159) for 2D cells and bacteria, and a TurboBlot Transfer machine using a mixed MW protocol (2.5 Ampere constant for 7 mins).

After transfer, membranes were stained with Ponceau S staining solution (Thermo Scientific, A40000279) to ensure transfer quality. The membranes were blocked with 5% milk (Milipore, 1.15363.9010) in 1x TBS-T. Primary antibodies were diluted with 5% BSA (Pro-bumin Bovine Serum Albumin Microbiological Grade, Sigma Aldrich) supplemented with 0.02% sodium azide (Sigma Aldrich), and incubated with the membranes overnight at 4°C. The following primary antibodies were used at 1:500: c-Myc Monoclonal Antibody (9E10) (Thermo Fisher, MA1-980, RRID: AB_558470); at 1:1000: E2F4 (E3G2G) (40291, Cell Signaling Technology, RRID: AB_2799174), Thymidylate Synthase (D5B3) XP Rabbit mAb (9045T, Cell Signaling Technology, RRID: AB_2797693), RRM2 (E7Y9J) XP Rabbit mAb (65939T, Cell Signaling Technology, RRID: AB_2895029), Recombinant Anti-Thymidine Kinase 1/TK1 antibody [EPR3194] (ab91651, abcam, RRID: AB_2050398) and α-Tubulin Antibody (2144S, Cell Signaling Technology, RRID: AB_2210548), at 1:2000: Anti-CRP mouse mAb (BioLegend, 664304, RRID: AB_2565553), at 1:2500: purified anti-*E.coli* RNA Sigma 70 antibody (BioLegend, 663208, RRID: AB_2814499) as well as at 1:10,000 β-actin (A1978, Sigma-Aldrich, RRID: AB_476692).

Following incubation, membranes were washed and probed with Anti-rabbit IgG, HRP-linked Antibody (#7074S, Cell Signaling Technology, RRID: AB_2099233) or Anti-mouse IgG-Peroxidase antibody (A0168, Sigma-Aldrich, RRID: AB_257867) diluted 1:3000 in 5% milk in 1x TBS-T. Protein bands were visualized using Clarity Western ECL Substrate (BioRad, #1705061). Membranes were subsequently stripped using Pierce Restore PLUS Western Blot Stripping Buffer (Thermo Scientific) for re-probing. Finally, western blot images were analyzed using Gel Analyzer 23.1.1 software and Microsoft Excel 16.78.3 for data interpretation.

DNA damage dynamics

HCT116 cells were seeded in 12 well plates at 75,000 cells/well in complete media and treated the next day with 10 mM 2-MiCit or drug vehicle. After 24 h treatment the cell media was changed to normal complete media and proteins were collected 2, 6 and 24 h after treatment cessation. Proteins were processed as described before and probed with DDB2 Polyclonal antibody (30173-1-AP, Proteintech, RRID: AB_2935524) diluted 1:1000 in 5% BSA-1xTBS-T as the primary, and the Anti-rabbit IgG, HRP-linked antibody diluted 1:3000 in 5% milk-1xTBS-T as the secondary, and α-Tubulin Antibody as a loading control as described before.

Annexin V/PI staining

HCT116 cells were seeded into a 24 well plate at 50,000 cells/well in complete medium and treated for 48 h- and 24 h-exposure one and two days later with 10 mM 2-MiCit or control, respectively. The supernatant was collected as well as the attached cells. To measure apoptosis, the eBioscience Annexin V-Apoptosis Detection Kit FITC (Invitrogen, 88-8005-72) was used and the instructions without a Fixable Viability Dye were followed. Sample acquisition was performed with a LSRFortessa cytometer and data were analyzed with the FlowJo software (v10.10.0).

Cell cycle profiling

HCT116 cells were seeded into 6 well plates at 300,000 cells per well and treated with 10 mM 2-MiCit and control one day later. After 24 h treatment the cells were washed with warm DPBS, detached and diluted to 1×10^6 cells per sample. The cells were fixed drop-wise with cold 100% EtOH to a final concentration of 70% EtOH and incubated at 4°C for 2 h before following the instructions of the FxCycle PI/RNase Staining Solution Kit (Invitrogen, F10797). Sample acquisition was performed with a LSRFortessa cytometer and data were analyzed with the FlowJo software (v10.10.0).

HyPer7 measurement

2000 HCT116 cells with a wildtype or mutated p53^(-/-) protein were seeded in 100 µL of complete media on a poly-L-Lysine-coated (Sigma-Aldrich, P4832) 96-well plate (CELLSTAR µClear, Greiner Bio-One, 655090). After 24 h, cells were transfected with the pCS2+MLS-HyPer7 plasmid [gift from V. Belousov (Addgene plasmid #136470; RRID: Addgene_136470)⁹⁹] targeted to the mitochondrial membrane containing the H2O2 sensor using Lipofectamine 3000 (Thermo Fisher Scientific, L3000-001). After 2 days additional 50 µL complete medium was added to each well. The following day, the medium was replaced by 50 µL HBSS minimal medium (140 mM NaCl, 5 mM KCl, 1 mM MgCl₂, 2 mM CaCl₂, 20 mM HEPES and 10 mM glucose in MilliQ water) containing 10% FBS, and the 96-well plate was incubated inside the BioTek Cytation 5 Multimode Reader (Agilent Technologies), set to 37°C and 5% CO₂. The protocol for experiment A described in Jacobs et al.¹⁰⁰ was carefully followed with the following modifications. Instead of bolus H2O2, a bolus of 0 mM, 10 mM and 20 mM 2-MiCit was added to the cells by hand and images were acquired every 2.5 min.

The acquired images were analyzed using the RRA software (Redox Ratio Analysis¹⁰¹). The images were aligned, filtered, background-subtracted, and the intensity for both channels as well as the resulting ratios calculated and saved as an Excel file. Further processing was done using R. A blank subtraction was performed to account for background signal. The mean of the first ten measurements, that correspond to the baseline data before adding the bolus, for each single cell were calculated and then subtracted from the respective values for that single cell. Data was split into 4 tracks depending on the current treatment: baseline (t0 to t30); 2-MiCit treatment (t31 to t90); H2O2 treatment (t91 to t110); and DTT treatment (t111 to t130). AUC values were calculated for each condition and track using R library MESS.

Seahorse

HCT116 cells (both WT and p53^(-/-) genotypes) were used for this experiment in the presence of 2-MiCit (1, 5 or 10 mM) and in control (vehicle) conditions. Basal extracellular acidification rate (ECAR) and oxygen consumption rate (OCR) measurements were determined using a seahorse XFe96 analyzer (Agilent). Briefly, 10,000 cells/well were seeded on an Agilent Seahorse 96-well XF Cell Culture Microplate in complete media and exposed to 2-MiCit for 24 h. Cells were analyzed the next day using Seahorse RPMI media, consistent of Seahorse XF RPMI (Agilent) supplemented with 10 mM glucose, 2 mM glutamine and 1 mM pyruvate at pH 7.4. Mitochondrial respiration, represented as OCR, was measured using a Mitochondrial Stress Test Kit following manufacturer's instructions with 1.5 µM oligomycin, 0.5 µM FCCP and 0.5 µM Rotenone/Antimycin A (Agilent).

Respiration rates from each condition were computed and retrieved from the machine using XFe Assay (v.2.6.1.56), downstream analyses and graphs were done in the R-environment. Raw data was used to divide the dataset into the 4 major stages of the experiment, and pmol/min values were used to calculate the basic respiration parameters following Seahorse manual, i.e., basal respiration, ATP production, proton leak, maximal respiration, spare respiratory capacity and non-mitochondrial respiration. Respiration of the different 2-MiCit concentrations were compared to control condition using T-test. A two-way ANOVA was used to calculate the statistical interactions between the effect of 2-MiCit compared to a control of 1mM 2-MiCit in the two HCT116 cells genotypes (WT and p53^(-/-)).

In vitro IDH activity assay

The effect of different forms of 2-MiCit on NADP⁺ dependent isocitrate dehydrogenase (IDH) activity was measured with the Isocitrate Dehydrogenase Assay kit (Abcam) as per the manufacturer's instructions. Briefly, Isocitric Dehydrogenase (NADP) from porcine heart (Sigma-Aldrich) was diluted 100x in IDH assay buffer and introduced to the wells of a 96 well plate (1 µL/well), resulting in a further 100x dilution. This ensured that the readings were within the linear range of the standard curve. A serial dilution of 2-MiCit or its enantiomers spanning from 10 mM to 0.078 mM was incubated with the enzyme, followed by the addition of the master mix containing the substrate isocitrate. The plate was incubated for 2 h at 37°C in a microplate reader and product formation was monitored spectrophotometrically every 2 min at 450 nm. A standard curve was prepared using NADH.

Replication stress analysis

HCT116 cells were plated at a density of 1000 cells/well in a 384 well CellCarrier plate (PerkinElmer) in 20 µL of full growth medium. The next day, cells were treated with vehicle or 10 mM of 2-MiCit by adding 10 µL of growth medium plus vehicle/drug to plates. After 24 h, 10 µM 5-Ethynyl-2'-deoxyuridine (EdU) was added for the last 30 min of incubation before plates were fixed in 4% formaldehyde in PBS for 15 min at RT. Cells were permeabilized in PBS/0.5% Triton X-100 for 15 min at RT, blocked in blocking solution (2% BS in PBS) for 30 min at RT and EdU positive cells were labelled by the Click-iT reaction with Alexa-647 (ThermoFisher). After EdU labelling, cells were immunostained with either anti-*γ*H2AX (1:2000, Cell Signaling Technology 2577; RRID: AB 2118010), -53BP1 antibodies (1:1000, Cell Signaling Technology 4937; RRID: AB 10694558), -p21 (1:500, BD Biosciences 556430; RRID: AB 396414) or -p53 (1:500, Cell Signaling Technology 2527; RRID: AB 10695803) antibodies diluted in blocking buffer, overnight at 4°C. The next day, plates were washed 3x in PBS and labelled with Alexa-488 labelled secondary antibodies, 1:1000 dilution at RT in the dark (Thermo Fisher Scientific, A-21202; RRID: AB 141607 or A-21206; RRID: AB 2535792). Plates were washed 3x in PBS, labelled with 1 µg/mL Hoechst 33258 for 15 min at RT in the dark before a final wash in PBS. Plates were imaged on an Operetta microscope (Revity) using a 20x N.A. 0.8 objective. Fluorescence intensities and DNA damage foci were quantified using Harmony image analysis software (Revity).

For measuring *yH2AX* intensity in HCT116 cells treated with 5-FU, 2000 cells per well were plated into a poly-L-Lysine-coated (Sigma-Aldrich, P4832) 96-well plate (Falcon, 353219) in 100 µL complete media. After letting cells attach and grow to 60%

confluence for 2 days, the cells were treated for 24 h with 10 μ M 5-FU or control. For immunofluorescence staining, cells were washed with pre-warmed 1x PBS and fixed with pre-warmed freshly prepared 4% PFA (Thermo Scientific, 28906) in PBS for 15 min at 37°C. Following fixation, cells were washed 3x with 1x PBS for 2 min each. To quench autofluorescence, cells were incubated with 50 mM ammonium chloride (NH_4Cl) in PBS for 15 minutes, followed by a single wash with 1x PBS for 2 min. Permeabilization was performed using 0.1% Triton X-100 in PBS for 10 min, after which cells were washed 3x with PBS for 2 min each. Blocking was carried out using 10% heat-inactivated goat serum (HGS; Cell Signaling Technology, 5425S) in PBS for 30 min at RT. Primary antibody staining was performed with anti- γ H2AX (1:2000) diluted in 5% HGS in PBS, incubated overnight at 4°C. Cells were then washed three times with 5% HGS in PBS for 5 minutes each. Secondary antibody staining was performed using Alexa Fluor 568 (Thermo Fisher, A-11011) diluted (1:1000) in 5% HGS in PBS for 1.5 h at RT in the dark. Cells were washed 3x with PBS for 5 min each, with DAPI (Fisher Scientific, 10116287) added during the second washing step at a final concentration of 0.2 μ g/mL. Cells were maintained in PBS for imaging using the ImageXpress Micro 4 system (Molecular Devices) using a 40x Plan Apo Lambda air objective with TRITC and DAPI filters. Image analysis was carried out using FIJI (v 1.54 k) and CellProfiler (v 4.2.6).

Synthetic chemistry

(2*R*,3*S*)-2-Methylisocitrate [(2*S*,3*R*)-3-hydroxybutane-1,2,3-tricarboxylate, **1** (as trisodium salt)] was synthesized ([Scheme 1](#)) from (*R*)-lactic acid **2** by modification of a literature procedure.⁵⁶ Following the procedure of Ley and co-workers,¹⁰² acid-catalyzed reaction of (*R*)-lactic acid with 5,5',6,6'-tetrahydro-4*H*,4'H-2,2'-bipyran **3** gave the dispiroketal (6*S*,7*S*,15*R*)-15-methyl-1,8,13,16-tetraoxadispiro[5.0.5.4]-hexadecan-14-one **4**. Dispiroketal **4** was deprotonated at C-15 with lithium diisopropylamide and the resulting carbanion was reacted with racemic diethyl 2-bromosuccinate **5** to afford diethyl (2*S*)-2-[(6*S*,7*S*,14*R*)-14-methyl-15-oxo-1,8,13,16-tetraoxadispiro[5.0.5.4]hexadec-14-yl]butanedioate **6**. Acidic hydrolysis of compound **6** gave the crystalline lactone (2*R*,3*S*)-2-methyl-5-oxotetrahydrofuran-2,3-dicarboxylic acid **7**, which afforded (2*R*,3*S*)-2-methylisocitrate trisodium salt **1** on treatment with sodium hydroxide. Alternatively, compound **6** was subjected to acid-catalyzed methanolysis, which gave crystalline dimethyl (2*R*,3*S*)-2-methyl-5-oxotetrahydrofuran-2,3-dicarboxylate (lactone **8**, major product) and trimethyl [(2*S*,3*R*)-3-hydroxybutane-1,2,3-tricarboxylate [(trimethyl (2*R*,3*S*)-2-methylisocitrate **9**, minor]. The absolute configuration of lactone **8** was determined as (2*R*,3*S*) [2-methylisocitrate numbering] by crystallographic analysis (Begum et al., unpublished results), confirming the original assignment for compound **7**.⁵⁶ Reaction of lactone **8** with sodium hydroxide gave **1**, which on treatment with an excess of iodomethane gave trimethyl ester **9** (major product) with lactone **8** (minor).

QUANTIFICATION AND STATISTICAL ANALYSIS

General

Data was considered statistically significant when $p < 0.05$, one-way ANOVA, two-way ANOVA or Benjamini-Hochberg FDR < 0.05 as indicated in the figure, figure legend or experimental methods. Asterisks denote corresponding statistical significance * $p < 0.05$; ** $p < 0.01$; *** $p < 0.001$. Data is presented as the mean \pm SD or mean \pm SE where appropriate from at least 3 independent biological replicates, unless stated otherwise in figures, figure labels or experimental methods. Statistical analysis was performed using GraphPad Prism software (v9), the R-environment (version 4.30) or Python (version 2.7.15 and 3.10) as specified in each section. The statistical tests used to compare groups were T-test, linear models, one-way ANOVA, two-way ANOVA, Wilcoxon rank-sum test. Correction for multiple tests were applied (via Benjamini-Hochberg) unless stated otherwise. The log(inhibitor) vs. response - variable slope (four parameter) model in GraphPad Prism was used to calculate IC₅₀. Hypergeometric tests were used to calculate enrichment unless stated otherwise.

The main software used for statistics has been the R-environment, where data has been mainly handled and plotted with the functions contained in the “tidyverse” package (v.2.0.0)⁶⁷ and statistics have been calculated either by using the base “lm” function for linear models, “multcomp” (v.1.4-25) to define multiple interaction effects in the high throughput screens, and rstatix (v.0.7.2) as a wrapper of a diverse set of statistical comparisons (one and two-way ANOVA, multiunivariate T-test and Wilcoxon test). No distribution showed signs of deviation from homoscedasticity or normality unless stated otherwise. Packages used in R to calculate the different statistics and other computational methods have been described throughout the different methods section indicating the version used.